Graphitic Carbon Nitride/Oxygen Deficient Tungsten Oxide S-Scheme Heterojunctions for the Photocatalytic Methyl Orange Degradation and Hydrogen Peroxide Generation under Visible Light Irradiation

by

Aleyna BAŞAK

A Dissertation Submitted to the
Graduate School of Sciences and Engineering
in Partial Fulfillment of the Requirements for
the Degree of

Master of Science

in

Materials Science and Engineering

KOÇ
ÜNİVERSİTESİ

December 19, 2023

Graphitic Carbon Nitride/Oxygen Deficient Tungsten Oxide S-Scheme Heterojunctions for the Photocatalytic Methyl Orange Degradation and Hydrogen Peroxide Generation under Visible Light Irradiation

Koç University

Graduate School of Sciences and Engineering

This is to certify that I have examined this copy of a master's thesis by

Aleyna BAŞAK

and have found that it is complete and satisfactory in all respects,
and that any and all revisions required by the final
examining committee have been made.

Committee Members:

Assoc. Prof. Önder Metin (Advisor)

Assoc. Prof. Sedat Nizamoğlu

Prof. Dr. Sermet Koyuncu

Date: _____

[To my lovely family]

ABSTRACT

Graphitic Carbon Nitride/Oxygen Deficient Tungsten Oxide S-Scheme Heterojunctions for the Photocatalytic Methyl Orange Degradation and Hydrogen Peroxide Generation under Visible Light Irradiation

Aleyna Başak

Master of Science in Materials Science and Engineering

December 19, 2023

Synthetic dyes used in various sectors, especially textile and paper, are one of the most important causes of water pollution. These synthetic dyes, which are released into water stream without being reduced to less toxic byproducts, seriously affect the aquatic ecosystem. For example, synthetic dye effluents in a lake absorb most of the sunlight, making it difficult for algae to photosynthesize. In addition, since dyes mix with groundwater, freshwater reserves are decreasing day by day. In this context, the release of synthetic dye effluents into water streams without being converted into harmless or less harmful by-products such as CO_2 and H_2O threatens the aquatic ecosystem in the short term and all living life in the long term. Another problem facing humanity is that fossil fuels are about to run out. As of the 21st century, alternative energy sources to fossil fuels are being considered in order to ensure the continuity of civilization. However, the alternative resources that are focused on should not strengthen the threat of global warming, which is accelerating today due to the uncontrolled use of fossil fuels and makes itself felt more as a climate crisis. Among the alternatives, hydrogen peroxide (H_2O_2), which posseses high energy density, as an energy carrier has attracted great attention from the scientific community since no harmful byproduct or emission are produced when H_2O_2 is used. Photocatalysis, which is based on the excitation of semiconducting material called photocatalyst through sunlight and its production of electrons and holes to be used in reduction/oxidation reactions, is one of the most sustainable and promising methods for degradation of dyes to harmless compounds and the generation of H_2O_2 from water. The most critical point in photocatalytic applications is an effective photocatalyst design that can meet the demands and provide high efficiency.

Graphitic carbon nitride (g-CN) is a polymeric semiconductor with a generally two-dimensional and layered structure. Furthermore, it can be easily synthesized using nitrogen-rich materials such as melamine and urea. It can be separated into thinner layers by exfoliation. The fact that g-CN can be activated by visible light due to its approximately 2.7 eV band gap and suitable band positions make it a frequently preferred material in photocatalytic applications. However, the fast and high rate of recombination of photo-generated electrons and holes along with extremely limited light absorption capacity in the visible region pose a major obstacle for the wide-scale use of g-CN. To overcome these disadvantages of g-CN, constructing heterojunctions with other semiconductor materials is a frequently used and successful strategy. In this regard, oxygen-deficient tungsten oxide (WO_{3-x}) is one of the most attractive semiconductors to form a heterojunction with g-CN. First of all, the high valence band potential enables many photocatalytic reactions to occur. However, the most interesting point about this material is the optical properties caused by deficiency of oxygen in the structure. In this way, WO_{3-x} gains a localized surface plasmon resonance property, which makes possible

to produce electrons and holes in the visible and infrared regions despite its wider band gap close to 3 eV. As a consequence, the light absorption ability of the material increases and additional electrons and holes are provided to the system to use in reduction and oxidation reactions. In the light of the information presented, in this thesis, graphitic carbon nitride/oxygen deficient tungsten oxide (g-CN/WO_{3-x}) heterojunction photocaytalyst was synthesized for use in photocatalytic dye degradation and H_2O_2 production without any metal addition.

In this thesis, g-CN/WO_{3-x} heterojunction was synthesized via the solvothermal method, but synthesis parameters such as temperature, time, solvent and concentration (mg/mL), which affect the localized surface plasmon resonance intensity of WO_{3-x}, were also evaluated to synthesize optimum g-CN/WO_{3-x} photocatalyst. Then, advanced characterization methods (Raman, XRD, SEM, TEM, XPS, ssNMR, UV-Vis DRS, PL, TRPL, TPC and EIS) were used to reveal the structural, chemical, photophysical and electrochemical properties of the photocatalyst. Analysis revealed that heterojunction synthesis occurred successfully and electron-hole recombination was greatly suppressed while the optical properties of the heterojunction improved. In the application section, under white light (λ> 400 nm), the photocatalyst achieved 98% degradation of 5 ppm methyl orange in 25 minutes (k = 0.1787 min^{-1}) and generated 45.9 mg/L H_2O_2 from 10 wt % methanol solution in 90 minutes. Additionally, in H_2O_2 production, the effect of adding various alcohols as hole scavenger to the reaction medium on photocatalytic activity was investigated and it was observed that adding 10 wt% isopropanol to the reaction environment resulted in the production of 87.44 mg/L H_2O_2. By using various characterization methods, band structures of semiconductors were found and plausible electron flow routes were determined. Then, it was revealed that the formed g-CN/WO_{3-x} heterostructure demonstrated S-scheme heterojunction properties. In the following step, H_2O_2 experiments were carried out at green light, and it was proved that hot electrons could be produced thanks to localized surface plasmon resonance of g-CN/WO_{3-x} photocatalyst. Also pathway followed by hot electrons was determined through the same experiment. At the next step, under white light illumination, scavenger experiments were carried out to determine the reactive oxygen species present in the reaction environment, and it was seen that the photocatalyst had sufficient potential to produce superoxide and hydroxyl radicals as well as electrons and holes. Following all these results, a possible reaction mechanism was suggested for photocatalytic methyl orange degradation and hydrogen peroxide generation. High activity of the photocatalyst was associated to reasons as follows i) decreased electron-hole recombination due to the formation of S-scheme heterojunction ii) enhanced light absorption ability of photocatalyst towards visible and near-infrared region thanks to the localized surface plasmon resonance, iii) generated hot electrons to participate in redox reactions. At the end, recyclability measurements were performed and it was observed that the photocatalyst maintained its high activity during the first 4 cycles, but there was a sharp decrease in activity at 5^{th} cycle. Based on the XRD analysis applied after the 5^{th} cycle, the loss of activity was explained by the conversion of WO_{3-x} in the photocatalyst to stoichiometric WO_3.

ÖZETÇE

Görünür Bölge Işıması Altında Fotokatalitik Metil Oranj Bozunması ve Hidrojen Peroksit Üretimi için Grafitik Karbon Nitrür/Oksijen Noksanlı Tungsten Oksit S-şemalı heteroeklemleri

Aleyna Başak

Malzeme Bilimi ve Mühendisliği, Yüksek Lisans

19 Aralık 2023

Tekstil ve kağıt başta olmak üzere çeşitli sektörlerde kullanılan sentetik boyalar su kirliliğinin en büyük etkenlerinden biridir. Toksisitesi daha az olan yan ürünlere indirgenmeksizin suya salınan bu boyalar su ekosistemini ciddi şekilde etkilemektedir. Örneğin, su içerisindeki sentetik boyalar güneş ışığının büyük kısmını soğurduğundan alglerin fotosentez yapması imkansız hale gelmektedir. Ayrıca, boyalar yer altı sularına da karıştığından içilebilir su rezervleri her geçen gün azalmaktadır. Bu bağlamda, sentetik boyaların CO_2, H_2O gibi zararsız ya da daha az zararlı yan ürünlere dönüştürülmeden suya salınması kısa vadede su ekosistemini uzun vadede ise tüm canlı yaşamını tehdit etmektedir. İnsanlığın karşı karşıya kaldığı bir diğer sorunsa fosil yakıtların tükenmek üzere olmasıdır. 21. yüzyıl itibari ile medeniyetin devamlılığının sağlanabilmesi için fosil yakıtlara alternatif enerji kaynakları üzerine düşünülmektedir. Ancak üzerine yoğunlaşılan alternatif kaynaklar, günümüzde fosil yakıt kullanımı nedeniyle ivmelenen ve iklim krizi olarak kendini daha çok hissettiren küresel ısınma tehdidini güçlendirmemelidir. Alternatifler arasında olan yüksek enerji yoğunluğuna sahip hidrojen peroksitin (H_2O_2) enerji taşıyıcı olarak kullanılabilme ihtimali bilim camiasının büyük ilgisini çekmiştir. Çünkü taşıdığı enerjiyi açığa çıkarmak için H_2O_2 kullanıldığında herhangi bir zararlı madde üretilmez. Fotokatalizör olarak adlandırılan yarı iletken malzemelerin güneş ışığı aracılığıyla uyarılmasına ve indirgenme/yükseltgenme reaksiyonlarında kullanılmak üzere elektron ve hol üretmesine dayanan fotokataliz, boyaların zararsız bileşiklere indirgenmesinde ve sudan H_2O_2 üretiminde en sürdürülebilir ve umut vadeden yöntemlerden biridir. Fotokataliz uygulamalarında ise en kritik nokta talepleri karşılayabilen ve yüksek verim sağlayan etkili bir fotokatalizör tasarımıdır.

Grafitik karbon nitrür (g-CN), azot bakımından zengin melamin, üre gibi malzemeler kullanarak kolayca sentezlenebilen genellikle iki boyutlu ve tabakalı yapıya sahip polimerik bir yarı iletkendir. Eksfoliasyon ile daha ince tabakalara ayrılabilmektedir. g-CN'nin hem yaklaşık 2.7 eV bant aralığı sebebiyle görünür ışık ile aktive edilebilir olması hem de uygun bant pozisyonları, onu fotokatalitik uygulamalarda sıklıkla tercih edilen bir malzeme yapmaktadır. Ancak foto-üretilen elektron ve hollerin hızlı ve yüksek oranda rekombinasyonu ve görünür bölge içerisindeki ışık absorpsiyon kapasitesinin oldukça kısıtlı olması, g-CN'nin geniş çapta kullanımı önünde büyük engel teşkil etmektedir. g-CN'nin bu dezavantajlarını gidermek için başka yarı iletken malzemelerle heteroeklemler inşa etmek sıklıkla kullanılan ve başarılı olan bir stratejidir. Oksijen noksanlığı olan tungsten oksit (WO_{3-x}), g-CN ile bir heteroeklem oluşturmak için en cazip yarı iletkenlerden biridir. Öncelikle, oldukça yüksek değerlik bant potensiyeli bir çok reaksiyonun gerçekleşmesini sağlamaktadır. Ancak bu malzemeye dair en ilgi çekici nokta yapıdaki oksijen noksanlığının ortaya çıkardığı optik özelliklerdir. Bu sayede,

WO_{3-x} lokalize yüzey plasmon rezonans özelliği kazanmakta bu da onun 3 eV'ye yakın bant aralığına rağmen görünür ve kızılötesi bölgede de elektron ve hol üretmesini mümkün kılmaktadır. Bu şekilde hem malzemenin ışık absorpsiyon yeteneği artmakta hem de sisteme indirgeme ve oksidasyon reaksiyonlarında kullanmak üzere fazladan elektron ve hol sağlanmaktadır. Sunulan bilgiler ışığında bu çalışmada, grafitik karbon nitrür/oksijen noksanlığı olan tungsten oksit (g-CN/WO_{3-x}) heteroyapısı herhangi bir metal eklemesi olmadan fotokatalitik boya bozunması ve H_2O_2 üretiminde kullanılmak üzere sentezlenmiştir.

Bu tezde, g-CN/WO_{3-x} heteroeklemi solvotermal yöntem aracığılıyla sentezlenmiştir ancak WO_{3-x}'in lokalize yüzey plasmon rezonans şiddeti üzerine etki eden sıcaklık, süre, çözücü ve konsantrasyon (mg/mL) gibi sentez parametreleri de değerlendirilerek optimum g-CN/WO_{3-x} fotokatalizörü elde edilmiştir. Ardından, fotokatalizörün yapısal, kimyasal, fotofiziksel ve elektrokimyasal özelliklerini gözler önüne sermek için ileri karakterizasyon yöntemleri (Raman, XRD, SEM, TEM, XPS, ssNMR, UV-Vis DRS, PL, TRPL, TPC ve EIS) kullanılmıştır. Analizler, heteroeklem sentezinin başarılı bir şekilde gerçekleştiğini ve heteroeklemin optik özellikleri gelişirken elektron-hol rekombinasyonunun büyük ölçüde baskılandığını açığa çıkarmıştır. Uygulama kısmında, beyaz ışık altında (λ> 400 nm) fotokatalizör 5 ppm metil oranjın 25 dakikada %98 oranında (k=0.1787) bozunmasını sağlarken 90 dakika içerisinde de kütlece %10'luk metanol çözeltisinden 45.9 mg/L H_2O_2 üretmeyi başarmıştır. Ayrıca, fotokatalitik H_2O_2 üretiminde, çeşitli alkollerin reaksiyon ortamına eklenmesinin fotokatalitik aktviteye etkisi araştırılmış ve kütlece %10 kadar isopropanolün reaksiyon ortamına eklenmesinin 87.44 mg/L H_2O_2 üretimi ile sonuçlandığı görülmüştür. Çeşitli karakterizasyon yöntemleri ile yarı iletkenlerin bant potensiyelleri bulunmuş ve elektronların muhtemel akış yolları belirlenerek oluşan heteroyapının S-şemalı heteroeklem özelliklerini gösterdiği ortaya çıkarılmıştır. Sonraki aşamalarda, yeşil ışık kullanarak yürütülen H_2O_2 deneylerinde g-CN/WO_{3-x} fotokatalizörünün lokalize yüzey plasmonu etkisiyle sıcak elektronlar üretilebildiği ve bu elektronların reaksiyon esnasında takip ettikleri yol belirlenmiştir. Takip eden süreçte, beyaz ışık altında yürütülen reaksiyonlarda, ortamda mevcut olan reaktif oksijen türlerine karar vermek için kurban ajan deneyleri yapılmış ve fotokatalizörün elektron ve holün yanısıra süperoksit ve hidroksil radikallerini üretmek için yeteri kadar potansiyele sahip olduğu görülmüştür. Tüm bu sonuçların ardından muhtemel bir reaksiyon mekanizması öne sürüldü ve fotokatalizörün yüksek aktivitesi S-şemalı heteroeklem oluşumu nedeniyle elektron-hol rekombinasyonunun azalması, lokalize yüzey plasmonu sayesinde fotokatalizörün oldukça geniş bir spektrumda ışık absorpsiyonu gerçekleştirebilmesi, ve yine lokalize yüzey plasmonu sayesinde fotokatalizörün daha düşük enerjili ışıklar aracılığıyla reaksiyonlarda kullanılmak üzere sıcak elektronlar üretmesi ile ilişkilendirilmiştir. Son aşamada ise tekrarlanabilirlik deneyleri yapılmış ve fotokatalizörün ilk 4 çevrim boyunca yüksek aktivitesini koruduğu ancak 5. çevrimde aktivite de sert bir azalış olduğu görülmüştür. 5. çevrimden sonra yapılan XRD analizinine dayanarak aktivite kaybı fotokatalizördeki WO_{3-x}'in WO_3'e dönmesi ile açıklanmıştır.

AKNOWLEDGEMENTS

I would like to thank all the people in my life who supported and helped me for my academic journey.

Firstly, I would like to express my deepest gratitude to my supervisor Assoc. Prof. Önder Metin since he gave me a chance to be a member of Metin Research Group, contributed to my scientific perspective and shared his knowledge and experience. Besides all these, I gained self-confidence, thanks to his encouraging and trusting attitude, and now I know what I can do.

I would like to thank my thesis committee members Assoc. Prof. Sedat Nizamoğlu and Prof. Sermet Koyuncu for their time and consideration in improving my master's thesis.

I would like to extend my thanks to Koç University Surface Science and Technology Center (KUYTAM) especially Dr. Hadi Jahangiri and Dr. Barış Yağcı for my TRPL and XPS measurements.

I would like to put into words my grateful feelings for former and present members of Metin Research Group. During my master period, I felt the sense of belonging, and at one point, SNA 224 became my second home. I made enjoyable and unforgettable memories. Thank you all for scientific discussions, daily conversations and more.

I would like to my heartfelt thanks to Dr. rer. nat. Melek Sermin Özer, Dr. Zafer Eroğlu, Dr. Orhan Altan and Asst. Prof. Sibel Eken Korkut for their amazing mentorship.

I would like to express my deepest thanks to my lovely friend Aybüke İzci. We are friends from ITU. We share our all sadness and happiness together. Throughout my education life, she believed in and supported me more than I did. Thanks for everything.

Lastly, I would like to thank my mum Neşe, dad Hüseyin and sister Beyza for supporting and encouraging me in every situation. I know they are there wwhenever I have a problem. Thank you.

TABLE OF CONTENTS

LIST OF TABLES

LIST OF FIGURES

ABBREVIATIONS

ROS	Reactive Oxygen Species
•OH	Hydroxyl radical
$•O_2^-$	Superoxide radical
HOO•	Hydroperoxyl radical
H_2O_2	Hydrogen Peroxide
g-CN	Graphitic Carbon Nitride
WO_{3-x}	Oxygen Deficient Tungsten Oxide
LSPR	Localized Surface Plasmon Resonance
UV-vis-NIR DRS	Ultraviolet-Visible-Near-infrared diffuse reflectance spectroscopy
TEM	Transmission Electron Mıcroscopy
XRD	X-ray Diffraction
EDX	Elemental Dispersive X-ray Spectroscopy
SEM	Scanning Electron Microscopy
XPS	X-ray Photoelectron Spectroscopy
PL	Photoluminisence
TRPL	Time-Resolved Photoluminisence
XPS-VB	X-ray Photoelectron Spectroscopy Valance Band
EIS	Electrochemical Impedance Spectroscopy
ssNMR	Solid State Nuclear Magnetic Resonance
Eg	Bandgap
NHE	Normal Hydrogen Electrode
MeOH	Methanol
EtOH	Ethanol
MO	Methyl Orange
C_0	Initial Concentration
C_t	Instantaneous Concentration
k	Reaction Rate
BQ	1,4-Benzoquinone
TEOA	Triethanolamine

IPA	Isopropanol
TA	Terephthalic Acid
λ	Wavelength
h	Planck Constant
ν	Frequency
ϕ_{Spec}	Work Function of XPS Instrument
K	Absorption Coefficient
S	Scattering Coefficient
α	Energy-dependent Absorption Coefficient
WE	Working Electrode
CE	Counter Electrode
RE	Reference Electrode
V_{fb}	Flat-Band Potential
C	Capacitance
V	Voltage
ε	Dielectric constant
NFE	Near Field Enhancement
CP	Cross Polarization
SRH	Shockley-Read-Hall
IEF	Internal Electric Field

Chapter 1:

INTRODUCTION

Wastewater remediation is an essential topic for the continuity of the ecosystem considering the limited natural sources. Releasing of dyes, antibiotics and heavy metal ions from industrial effluents to natural stream is the primary reason of water pollution. In this regard, some treatment procedures such as membrane filtration, ion exchange, electrocoagulation, and biological treatment are often used. However, major concerns in these treatments are their high cost and low efficiency. When these treatments are applied to wastewater, the toxicity of effluents is still unsolvable, and a huge amount of sludge formation creates another disposal problem [1]. In this regard, photocatalysis by utilizing solar energy is a promising way for the removal of these waste because in a photochemical process, well-designed photocatalyst can mineralize contaminants in the water stream partially or completely by producing reactive oxygen species (ROS) such as hydroxyl radicals (•OH), superoxide radicals ($\bullet O_2^-$) and hydroperoxyl radicals (HOO•) [2,3].

In a photocatalytic process, a semiconductor material called as photocatalyst is excited by photon with appropriate energy, which results in the generation of free charges called as excited electrons and holes at the conduction band (CB) and valence band (VB) of the semiconductor. These free charges are used directly or indirectly in redox reactions, mainly excited electrons (e^-) used for reduction and holes (h^+) for oxidation. As a conclusion, redox reactions will continue if the photocatalyst ensures e^-s and h^+s. Additionally, e^-s and h^+s tend to recombine and thus they should be separated for the efficient photocatalysis. Therefore, scientific community have made a great effort to design efficient photocatalysts where e^-s and h^+s are generated and their recombination is prevented [4].

Hydrogen peroxide (H_2O_2) production have been studied for a long time because H_2O_2 is one of the most important chemicals in the world. Although it has been used in different areas, recently H_2O_2 have been considered as an energy carrier. Photocatalytic hydrogen evolution from different sources have great attraction in academia because H_2 has exceptional energy density (3.5 MJ/kg), and its production is very clean. However, major concern in usage of H_2 as an energy carrier is transportation because it is in gas phase under standard conditions, and it needs huge volumes for storage. On the other

hand, energy density of 60% H_2O_2 aqueous solution is 2.1 MJ/kg, and it is also environmentally friendly. Another property of H_2O_2 is its full solubility in water, which is transportation in liquid form is applicable. These qualifications make it alternative to H_2 [5,6]. In this study, g-CN/WO_{3-x} heterojunction photocatalyst was designed to examine its performance at photocatalytic dye degradation for water remediation and H_2O_2 formation as an alternative energy carrier.

Graphitic carbon nitride (g-CN) is a low cost layered semiconducting polymeric material that can be synthesized via a facile thermal polycondensation procedure. Its activation under visible light illumination and excellent chemical and thermal stability make g-CN as an ideal candidate for solar-light-driven photocatalytic reactions. Nevertheless, high e^- - h^+ recombination rates, low electrical conductivity, limited optical absorption ability in visible-light region and insufficient surface area are shortcomings that hinder its extensive usage. To eliminate these inadequacies, the construction of its heterojunction with other semiconducting materials or metals are highly advantageous [7].

Oxygen deficient tungsten oxide (WO_{3-x}) is a type of non-stoichiometric metal oxide. Presence of oxygen deficiencies on WO_{3-x} surface introduces free electrons into crystal structure. In this way, WO_{3-x} behaves as a highly doped n-type semiconductor. As a result of enhanced dopant concentration, localized surface plasmon resonance (LSPR) property in WO_{3-x} semiconductor is revealed. Depending on free electron concentration, WO_{3-x} can show an LSPR peak in the visible and infrared range of light that results in greater activity [8]. Moreover, considering the larger bandgap, band positions, low-costs and non-toxic character of WO_{3-x}, it is thought that combining of g-CN with WO_{3-x} in the form of heterojunctions will enable more efficient structure to photocatalytic reactions [8, 9].

In this thesis, binary g-CN/WO_{3-x} heterojunctions was constructed for the photocatalytic dye degradation and hydrogen peroxide formation as an energy carrier. In addition to heterojunction formation between g-CN and WO_{3-x} for aforementioned applications, the other objectives of the thesis is as follows: *i*) to prove the creation of oxygen-deficiency within WO_{3-x} structure, *ii*) to achieve optimum photocatalyst by considering influences on synthesis procedure including temperature/time, solvent type, and concentration of tungsten precursor in solution (mg/mL) onto LSPR property of heterojunction *iii*) to elucidate the relation between plasmonic behavior-morphology and

activity and iv) unveiling the type of heterojunction formed between g-CN and WO_{3-x} as well proposing a plausible mechanism for the charge carriers migration in the heterojunction structure and their utilization in the photocatalytic reaction. In this context, ultraviolet-visible-near-infrared diffuse reflectance spectroscopy (UV-vis-NIR DRS) and transmission electron microscopy (TEM) were used to investigate effect of synthesis parameters on LSPR behavior and morphology. After deciding the best parameters, the formation of optimum heterojunction was enquired with various advanced characterization methods mainly X–ray diffraction (XRD), transmission electron microscopy with elemental dispersive X-ray spectroscopy (TEM-EDX), scanning electron microscopy (SEM) and X-ray photoelectron spectroscopy (XPS). Furthermore, photophysical properties of optimum heterojunction was evaluated by utilizing UV-vis-NIR DRS, photoluminescence spectroscopy (PL), and time-resolved photoluminescence spectroscopy (TRPL). Moreover, band structures and charge flow mechanism of heterojunction photocatalyst was elucidated by XPS-VB, Mott-Schottky and EIS analysis. Also, solid state nuclear magnetic resonance (ss-NMR) and RAMAN spectroscopies were used for further insight into oxygen deficient structure and hot-electron effect. In addition, several trapping experiments were carried out for further clarification of mechanism, and to understand hot-electron effect.

In the Chapter 1, a detailed introduction about photocatalysis, synthetic dyes, hydrogen peroxide, g-CN and WO_{3-x} were discussed along with the concept of semiconductor materials and heterojunctions were presented briefly. Chapter 2 summarizes the available literature on the photocatalytic studies on g-CN based heterojunctions, WO_{3-x} based heterojunctions, and g-CN/WO_{3-x} based heterojunctions. Chapter 3 outlines the methodology including chemicals&materials, experimental procedures, characterization techniques and electrochemical measurements used in the study. In Chapter 4, results and discussions about the data acquired on the materials characterization and photocatalytic studies were given, and the thesis ended with the conclusion part.

1.1 Synthetic Dyes

Dye is basically a material that imparts color to the applied substrate, and they are especially indispensable for textile dyeing and finishing, printing, photography, cosmetic

and pharmaceutical industries [10]. A dye molecule is composed of the chromophore, the auxochrome and the matrix which is generally aromatic amine groups. Chromophore is the light-absorbing part of dye, and this part contains unsaturated bonds. Thanks to these unsaturated bonds and conjugated π bonds of the matrix, dye absorbs light selectively in the visible region, and provides the complementary color of absorbed light to material with the help of auxochrome. The auxochrome part of the dye could have acidic or basic functional groups. The structures outside these parts are called the matrix [11].

Dyes have been used for over 4600 years. Before accidental invention of mauve, which is the first synthetic dye, from coal-tar by William Henry Perkin, dyes were obtained from natural sources such as plants, minerals and insects. On account of their natural characteristics, these dyes were easily biodegradable. However, synthetic dyes become more dominant as compared to natural ones in the industrialized world. Today, more than 3000 different synthetic dyes have been used in various industries, and consequently, more than 8 x 10^5 ton/year synthetic dyes are consumed in the world. In addition, these industries mostly discharge their dye effluents into water stream. In spite of alternative classifications, synthetic dyes are chemically categorized into nitro, nitroso, diarylmethane, triarylmethane, xanthene, anthraquinoid, acridine, cyanine, quinone-imine, pthalocyanine, thiazole and azo dyes [1, 10, 12] (**Figure 1.1**).

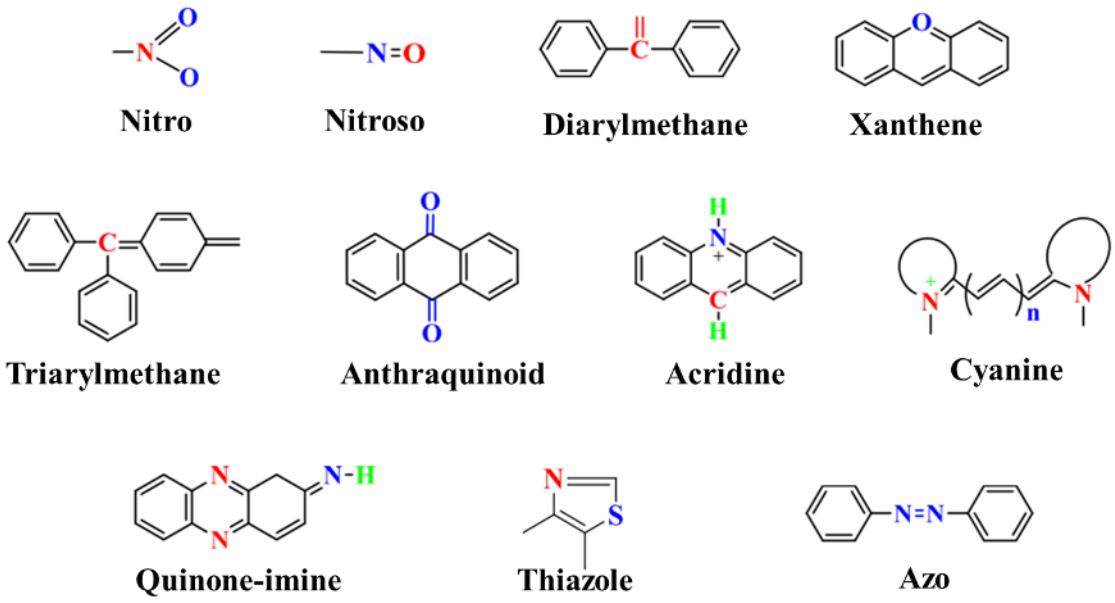

Figure 1.1: Classification of synthetic dyes based on chromophore [11]

Azo dye is the dye that its chromophore group is azo (-N=N-). Azo dyes account for 70% annual dye production. Therefore, these dyes are the most important group within synthetic dyes. Their various chemical structures, exceptional light fastness, strengths and high molar extinction coefficient, which is a measure of light absorption ability make them very substantial for dyeing industries. Nevertheless, most of them are carcinogenic and toxic. Their biodegradability is problematic because final product that results from biodegradation contains aromatic amine groups. Toxicity of these groups are higher than original dye molecule [10, 11]. Besides, azo dyes inhibit penetration of light inside water. Therefore, algae could not produce oxygen efficiently. Consequently, aquatic life and the photosynthesis cycle are affected adversely [13]. Considering all these, water should be remediated to ensure sustainability.

1.2 Hydrogen Peroxide

In 1818, Thenard achieved synthesis of hydrogen peroxide (H_2O_2) by reaction of barium peroxide (BaO_2) and nitric acid (HNO_3) for the first time [14]. From that day forward, H_2O_2 has become one of the essential chemicals in different industries such as organic chemistry, paper and pulp, mining, water protection and disinfection. Its high active oxygen content (47.1% w/w), and clean side products (H_2O and O_2), it makes a fabulous and environmentally benign oxidant [15]. Besides, since fossil fuels are on the verge of running out, and global warming is a growing danger, scientific community focus on fuel cell technology for production of electricity in a more sustainable way [6]. To date, hydrogen (H_2) has been seen the most suitable candidate as an energy carrier in fuel cells due to its satisfying energy density (3.5 MJ/kg) and high theoretical output voltage (1.23 V), non-toxic by-product and facile photocatalytic production [5, 14]. However, the most critical point about hydrogen fuel cells is storage and transportation of molecular H_2. First, low volumetric energy density of H_2 necessitates larger volumes for storage. Moreover, hydrogen can be stored in a form of gas or liquid but in gaseous phase, H_2 is compressed and stored in high-pressurized tanks while liquid form entails cryogenic conditions to prevent boiling of liquid H_2. In both cases, capitals for storage are not cost-effective and sustainable despite environmentally friendly character of H_2 [6, 16]. At this point, H_2O_2 has gained great attention as a clean energy carrier alternative to H_2. As a material, energy density (2.1 MJ/kg) and theoretical output voltage (1.09 V) of 60%

aqueous H_2O_2 are close to H_2. Furthermore, it has fully soluble in water, facilitating its transportation and storage. In addition, in the presence of H_2O_2-based fuel cell, there is no need any membrane to separate anode and cathode compartments [5, 14]. Approximately 95% of global H_2O_2 production was supplied through oxidation of anthraquinone (AQ). A standard AQ oxidation process initiates with hydrogenation of AQ (HAQ) in the presence of organic solvent and Ni or Pd catalyst [14]. The following step consists of oxidation of HAQ in air or O_2-enriched conditions by using the same catalyst. After oxidation of HAQ, the generated H_2O_2 is extracted from reaction environment, and HAQ backs to AQ for another usage. Process ends up with purification and concentration of H_2O_2. As can be understood, high amount of energy and organic solvent are spent by virtue of successive hydrogenation and oxidation reactions during AQ oxidation process. Apart from this, a considerable amount of wastewater, solid waste and exhaust gas are generated in the process, In **Figure 1.2**, a typical AQ process was illustrated [14, 17, 18].

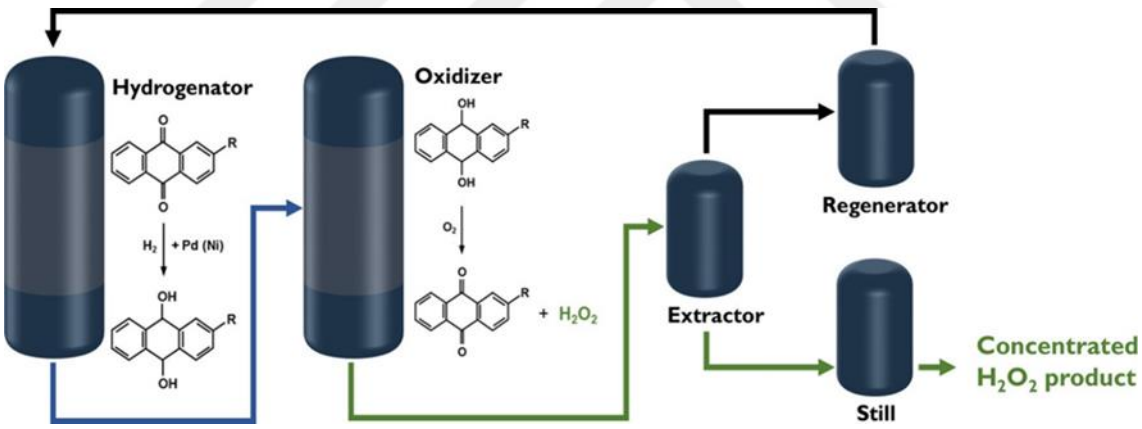

Figure 1.2: Diagram of anthraquinone process [18]

Direct synthesis of H_2O_2 from H_2 and O_2 over noble-metal catalyst was suggested by researchers to ensure cleaner production route. Reaction $H_2 + O_2 \Rightarrow H_2O_2$ is conducted by using Au or bimetallic Au-Pd metal catalyst, H_2 and O_2 mixture and acidic methanol at atmospheric pressure and around 0 °C. This procedure does not generate any waste and require high energy input. Nonetheless, its industrial usage is hindered by some drawbacks. The most important issue is coexistence of H_2 and O_2 in reaction medium since they might be explosive in most H_2/O_2 concentrations. The other one is low

selectivity towards H_2O_2. The last is expensiveness due to utilization of noble-metal catalyst [5, 15]. Considering the problems associated with the H_2O_2 synthesis via the oxidation of AQ and direct synthesis methods, development of a safer, more economical and sustainable H_2O_2 production strategy to industry is highly desirable. In accordance with this situation, recently, attention and curiosity of industry together with academia has focused on photocatalytic H_2O_2 generation which was detailed in **chapter 1.6.**

1.3 Photocatalysis and Semiconducting Materials

A product in the chemical reaction is formed when reactants collide each other on a correct direction and certain energy level. The mentioned required energy level is called as activation energy (E_a). Reactions generally requires high activation energy which behaves as a barrier to be overcome. Therefore, the activation energy causes relatively low reaction rate. Catalyst is a substance that increases reaction rate of a chemical reaction by proceeding it on an alternative pathway with lower activation energy. **Figure 1.3** illustrates how the catalyst changes the reaction pathway and lower the activation energy. Moreover, structure of catalyst is the same before and after reaction while its structure might be changed during reaction. Another interesting point about catalysts is that they are not consumed in the chemical process. These features allow catalyst to be used more than once in the chemical reaction [19]. Finally, catalysis is a phenomenon that is related to kinetics. Presence of catalyst in the medium does not change thermodynamics [19].

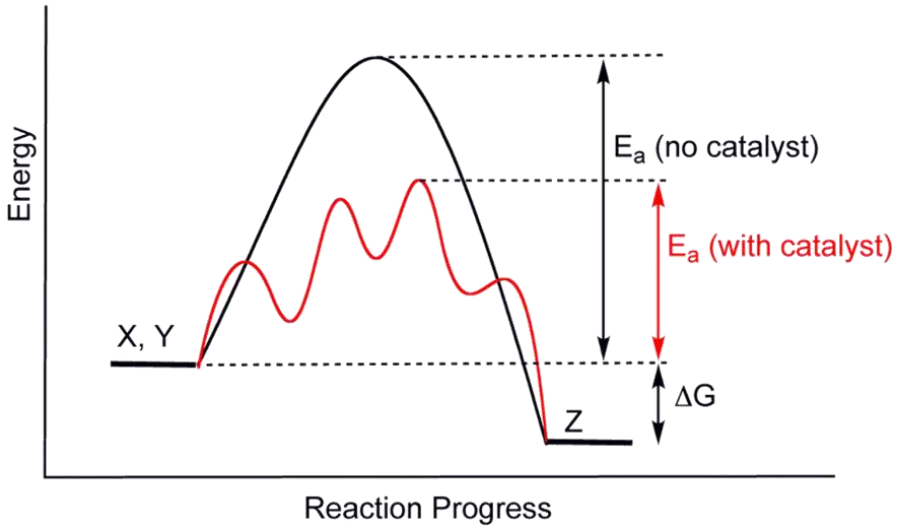

Figure 1.3: The effect of catalyst on reaction pathway and activation energy. Reprinted from ref. [20]

Catalysis is classified as biocatalysis, homogenous catalysis and heterogeneous catalysis. Biocatalysts are enzymes that are protein-based complex structures, and they catalyze reactions in the organisms. The most outstanding properties of biocatalysts are their extreme efficiency, activity and selectivity. Although they show excellent activity in mild conditions, their stability and activity are very problematic at high temperatures, extreme pH values and in organic solvents. In addition, their cost is very high. Due to these drawbacks, biocatalysts are not generally preferred in the industry [21]. Another class of catalysts is homogenous catalysis. In homogeneous catalysis, catalysts and reagents are in same phase in the solution and all active sites of catalyst have identical electronic structures. Therefore, homogenous catalysts exhibit excellent selectivity and activity. Besides the advantageous properties of homogeneous catalysts, their disadvantages are listed as follows: *i)* reducing the life of equipment due to the used severely corrosive liquids such as HF and H_2SO_4 [22] *ii)* being catalyst thermally unstable *iii)* separating product and catalyst from reaction environment since they are in the same phase with reagents. The last class of the catalysis is heterogeneous catalysis. In this case, the catalyst is generally in the solid form while reactants are liquid or gas phase. The fact that the catalyst and reactants are in different phases facilitating the separation procedure, and makes it possible to use the catalyst repeatedly. Also, it is thermally stable, and it does not need corrosive solvents for reactions. These are the main reasons why heterogeneous catalysts are more appealing to industry. However, heterogeneous catalysis suffers from low selectivity due to non-uniform surface sites [23].

Photochemistry is a branch of chemistry that studies the effect of light absorption on chemical reactions, and photocatalysis is one of the photochemistry subgroups. In a photocatalytic reaction, apart from reagents, another material known as photocatalyst is present in reaction medium. The mission of photocatalyst excited by light irradiation is to initiate the reaction or to rise the reaction rate [24-26].

Based on ability of materials to conduct electric current, they are categorized as conductors, semiconductors and insulators. All of them have partially or filled valance band (VB) and conduction band (CB) that is empty band located above VB. The magnitude of the band gap (E_g) between VB and CB bands determines their electrical properties (**Figure 1.4**). In conducting materials, there is no distinct band gap between VB and CB because these bands are overlapped. In the case of insulating materials, band gap is higher than 4 eV. Therefore, they need large amount of energy to accelerate

electrons from VB to CB. Semiconducting materials have bandgap that is smaller than 4 eV, and electrical conductivity of them increases when the band gaps get smaller [27, 28].

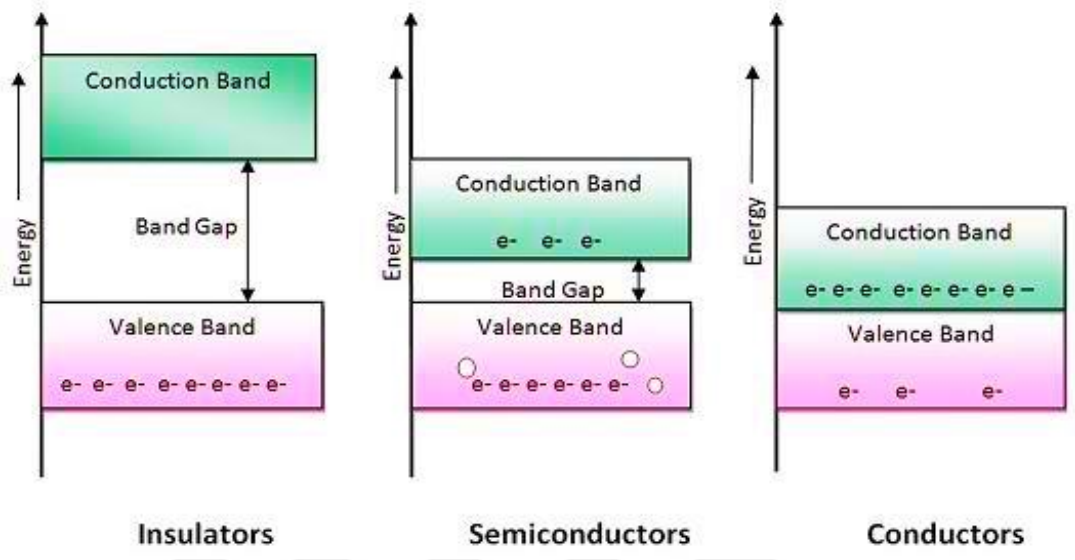

Figure 1.4: Position of energy band diagrams, and magnitude of bandgaps for insulators, semiconductors and conductors. Reprinted from ref. [29]

Semiconductor materials are divided into two as intrinsic and extrinsic semiconductors. Intrinsic semiconductors indicate perfect pure materials that do not contain any impurity or defect (**Figure 1.5a**).In these structures, completely filled valance band is seperated from empty conduction band through small bandgap that is mostly smaller than 1.5 eV. Due to their small band gaps, excitation of electrons from VB to CB can be initiated via mechanicallyor thermally. The extrinsic semiconductors have impurities and defects in their structure. Since even low concentration of impurities or defects change electrical properties of semiconductors exceedingly, modification of extrinsic semiconductors are more effortless. Moreover, impurities are unavoidable for a material. That is why all commercial semiconductors are an example of extrinsic semiconductors [30]. When an extrinsic semiconductor is excited, if the number of electrons in CB is greater than the number of holes in VB, it is called as n-type semiconductor (**Figure 1.5b**). Introduction of phosphorous (P) with 5 valance electrons into pure silicon (Si) matrix, which each Si atoms have 4 valance electrons, forms n-type semiconductor. In this case, P is electron donor. After excitation, if hole concentration is excess, semiconductor is p-type, and impurity element is named as electron acceptor

(**Figure 1.5c).** Addition of boron (B) with 3 valance electrons into intrinsic Si semiconductor creates p-type semiconductor [30, 31].

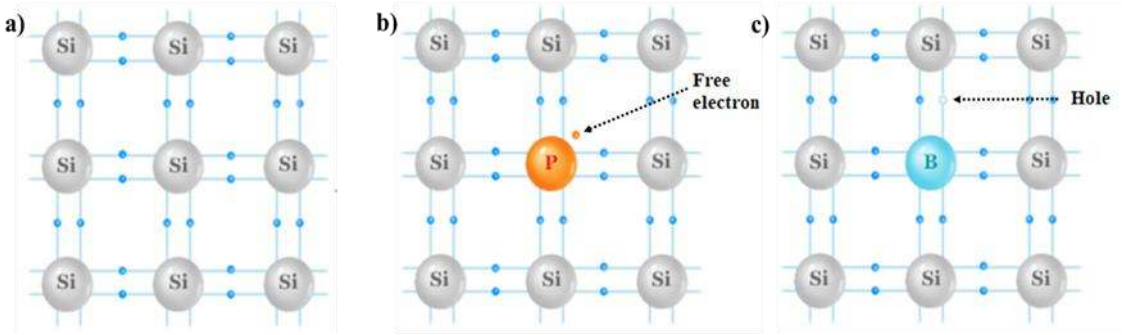

Figure 1.5: a) intrinsic semiconductor, **b)** n-type extrinsic semiconductor, **c)** p-type extrinsic semiconductor. Reprinted from ref. [32]

1.4 Heterojunction Photocatalysts

Photocatalysis is a promising solution to achieve sustainability because it uses solar energy directly. Nevertheless, in practical applications, it has some limitations that reduce activity. The major difficulty in a semiconducting material, serving as photocatalyst is fast electron-hole recombination. To increase photocatalytic reaction efficiency, the separation of electron-hole pair and their fast migration onto photocatalyst surface should be provided. Due to thermodynamic laws, it is impossible to completely prevent electron-hole recombination, but it can be suppressed to some extent by proposing diverse strategies [33]. Also, redox ability of a semiconductor cannot be enough for the desired photochemical reaction. To proceed with reduction and oxidation reactions spontaneously, a semiconductor needs a relatively positive VB maximum, and a relatively negative CB minimum. However, this creates a conflict. These band positions bring about larger bandgap which requires the excitation of photocatalyst with highly energetic photons. That configuration limits the solar spectrum utilization considerably because only small portion of solar spectrum which is around 5% belongs to ultraviolet radiation. Another concern which restrains their implementations is inadequate light harvesting ability of an individual semiconductor [34, 35]. Forming a heterojunction between two semiconductors is the most efficacious and applicable way to solve these problems. The term “heterojunction” is related to interface of two different semiconductor. More clearly,

when two semiconducting material with different Fermi levels contact with each other, electrons flow from higher Fermi level to lower Fermi level up to they are aligned, and an electric field is created at the interface due to charge difference, and bands of semiconductor bends according to electron flow direction. The electric field, specifically named as internal or built-in electric field, facilitates electron-hole separation and fast migration of them onto surface. Additionally, heterojunctions abate the aforementioned disadvantages of single semiconductor by creating synergism [34].

In the literature, heterojunctions have been classified as semiconductor-metal, semiconductor-carbon and semiconductor-semiconductor heterojunctions. Semiconductor-semiconductor heterojunctions are the most preferred combination in the construction of heterojunctions [34]. Before S-scheme heterojunction emerged, it was reported that 4 different types of heterojunction could be formed between two semiconducting materials. These are type I, type II, type III and Z-scheme which is special version of type-II. However, the introduction of the S-scheme heterostructure to the literature revealed that the presumptive charge transfer mechanisms in type-II and Z-scheme are not thermodynamically and dynamically feasible. Incorrect assumptions for type-II and Z-scheme are related to the pathway followed by charges. To further clarify these issues, charge transfer mechanism in Z-scheme heterojunctions will be explained below. [36, 37]. Moreover, type-I, type-III and S-scheme heterojunctions will be explained in this section.

In type-I heterojunction photocatalyst, one of the semiconductors has higher CB and lower VB potentials (semiconductor A) as compared to the other one (semiconductor B) as shown in **Figure 1.6a**. Therefore, flow of free electrons in CB and holes in VB of semiconductor A toward the semiconductor B is thermodynamically more favorable when the semiconductors are irradiated by a proper light source. Since both electrons and holes flows to semiconductor B with narrower bandgap, electron-hole recombination cannot be solved effectively. Additionally, reduction and oxidation potentials of photocatalyst is restricted due to lower redox ability of semiconductor B [37]. Accordingly, type-I heterojunctions could not provide highly effective photocatalyst design for the most of photon-driven reactions.

In type-III heterojunction called as broken bandgap, there is no flow of electron or hole between semiconductors due to non-overlapping bandgaps (**Figure 1.6b**). In this

design, two semiconductors forming the heterojunctions acting individually. As a result, influential separation of charge carriers cannot be achieved. Therefore, this heterojunction type is not appropriate for the development of efficient photocatalysts for any photocatalytic reactions [34].

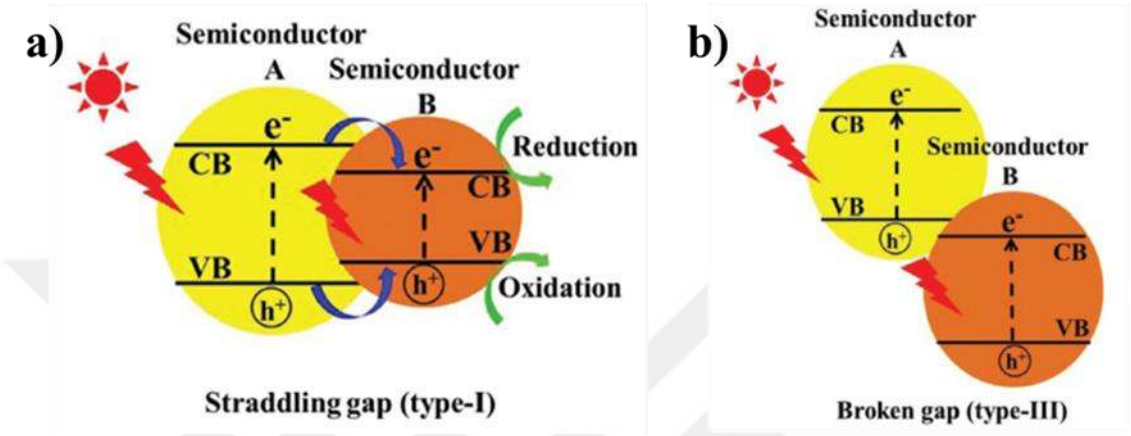

Figure 1.6: Band positions of semiconductors in **a)** type-I heterojunction, **b)** type-II heterojunction. Reprinted from ref. [37]

Z-scheme heterojunctions were the most attractive type of heterojunction since it conserves charges, having high redox ability based on assumed charge transfer route. However, Zhang and coworkers unveiled that these suggested pathway is wrong. In this regard, schematic illustration of all-solid-state Z-scheme was used to show supposed and real charge transfer pathway (**Figure 1.7**). Under light illumination, both Semiconductor 1 (S1) and Semiconductor 2 (S2) generate photo-induced charges, and then electrons in CB of S1 moves through conducting mediator to recombine with hole of S2 at supposed electron transfer pathway of all-solid-state Z-scheme heterojunctions (**Figure 1.7a**). In point of thermodynamics, this assumption is not correct. As can be seen in **Figure 1.7b,** S2 has more negative conduction band potential, and this situation makes more favorable recombination with e^{-}'s in CB of S2 and h^{+}'s in VB of S1. Another type of Z-scheme heterojunction is direct Z-scheme, but its charge transfer mechanism is still mystery [36].

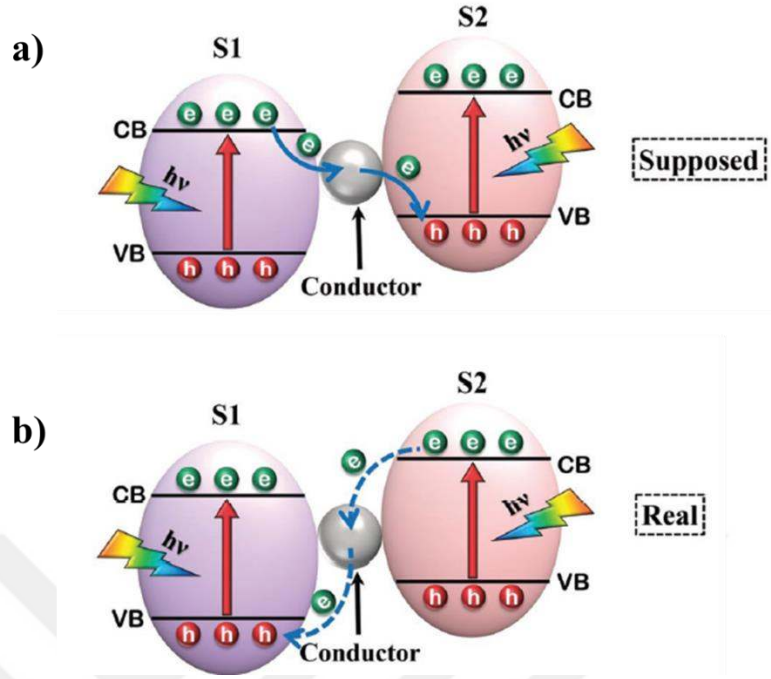

Figure 1.7: Schematic illustration of **a)** supposed **b)** real electron transfer pathways in all-solid-state Z-scheme heterojunctions [36]

S-scheme heterojunction where S describes step, is a modified version of Z-scheme heterojunction. This concept eliminates missing points of type-II and Z-scheme heterojunctions. In S scheme heterojunction, two semiconductors named as reduction photocatalyst (RP) and oxidation photocatalyst (OP) are present, and they get these names based on their work functions (**Figure 1.8a**). RP has higher Fermi level than OP. Hence, when RP and OP come into contact with each other, free electrons in CB of RP flows to OP at the interface of heterojunction, and this drift continues until Fermi level of these two semiconductors will be aligned. As a result of this charge transfer, RP loses electron and it becomes positively charged while OP gains electron and it is negatively charged. Simultaneously, upward bands bending for RP and downward bands bending for OP occurs at the interface. Concomitantly, an internal electric field from RP to OP is created at the interface (**Figure 1.8b**). Under light irradiation, photogenerated electrons in CB of OP make a move to VB of RP. Occurrence of internal electric field, proper band bending and strong Coulombic interaction between electron and hole assist presumed charge transfer mechanism, and they also hinder both recombination of e^-'s in CB of RB and h^+'s in VB of OP and movement of e^-'s from CB of RP to CB of OP or hole transfer from VB

of OP to VB of RP (**Figure 1.8c**). As conclusion, redox ability of photocatalyst increases, and recombination of e^-/h^+ in higher energy bands is prevented in S-scheme heterojunctions. Besides, the principles of this recommended charge transfer mechanism can be explained thermodynamically and dynamically [36].

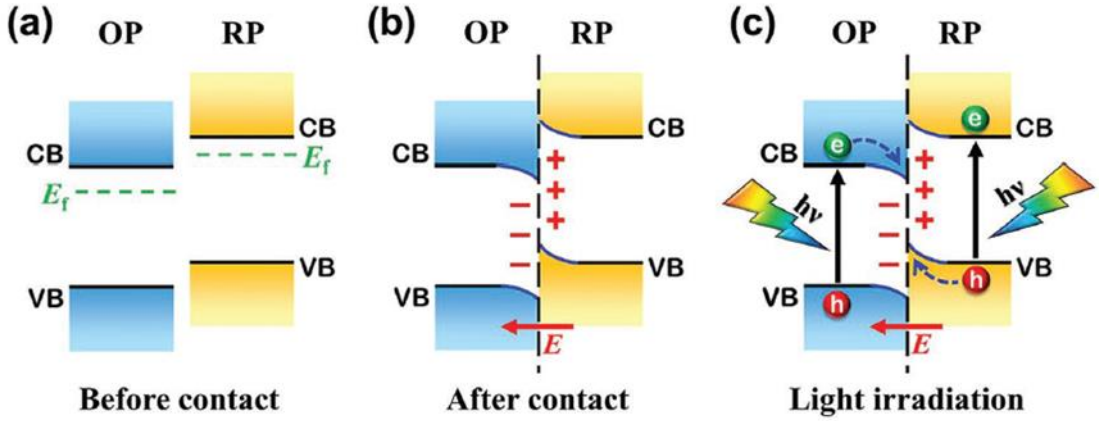

Figure 1.8: Charge carrier mechanism in S-scheme heterojunction **a)** before contact **b)** band bending after contact **c)** e^-/h^+ separation under light irradiation. Reprinted from ref. [36]

1.5 General Mechanism of Photocatalytic Degradation Reactions in Aqueous Medium

Photocatalysis is considered to be an advanced oxidation process. Although this phenomenon can be used for different applications, photocatalytic reactions follow a similar pathway [38]. However, mechanism was explained from perspective of photodegradation at this section. In a typical photodegradation reaction, reagents are transferred to the photocatalyst, and adsorption of them on photocatalyst's surface occurs. In this step, photocatalytic reaction initiates with photoexcitation of semiconductor. Here, photocatalyst is exposed to photon that its energy is equal or higher than semiconductor bandgap. As a result of this process, photogenerated electrons (e^-s) accelerates from VB to empty CB of semiconductor, and holes (h^+s) are formed in the VB (**Eq. 1.1**). To create reactive oxygen species (ROS) that participate in the redox reactions, free charge carries move to photocatalyst surface quickly [33]. Next, adsorbed water is ionized by reacting with holes in VB to generate hydroxyl (•OH) radicals (**Eq. 1.2**). •OH are exceedingly strong oxidizing agents, and very significant for photocatalytic reactions. At the same

time, dissolved O_2 in the environment use free e^-s in CB to produce superoxide ($\bullet O_2^-$) radicals (**Eq. 1.3**). In addition to oxidation process, $\bullet O_2^-$ serves other purposes. One of them is to suppress electron-hole recombination since e^-s are used for generation of $\bullet O_2^-$. Second one is protonation of superoxide radicals in order to obtain H_2O_2 (**Eq. 1.4**). The produced H_2O_2 compounds dissociate into •OH radicals by photogenerated electrons (**Eq. 1.5**). In the last step, reactants are oxidized or reduced according to semiconductor's band positions and reaction potentials, and finally, products are removed from surface of semiconductor (**Eq. 1.6-1.9**) [39, 40]. In **Figure 1.9**, illustration of a photocatalytic process can be seen.

$$\text{Photocatalyst} + h\nu \rightarrow h^+ (\text{VB}) + e^- (\text{CB}) \quad \textbf{(1.1)}$$

$$H_2O(\text{ads}) + h^+ \rightarrow \bullet OH(\text{ads}) + H^+ \quad \textbf{(1.2)}$$

$$O_2 + e^- \rightarrow \bullet O_2^- \quad \textbf{(1.3)}$$

$$\bullet O_2^- + 2H^+ + e^- \rightarrow H_2O_2 \quad \textbf{(1.4)}$$

$$H_2O_2 + e^- \rightarrow 2\bullet OH \quad \textbf{(1.5)}$$

$$\text{Pollutants} + \bullet OH / \bullet O_2^- \rightarrow \text{Intermediate} \quad \textbf{(1.6)}$$

$$\text{Intermediate} \rightarrow CO_2 + H_2O \quad \textbf{(1.7)}$$

$$\text{Pollutans} + h^+ \rightarrow \text{Oxidation products} \quad \textbf{(1.8)}$$

$$\text{Pollutants} + e^- \rightarrow \text{Reduction products} \quad \textbf{(1.9)}$$

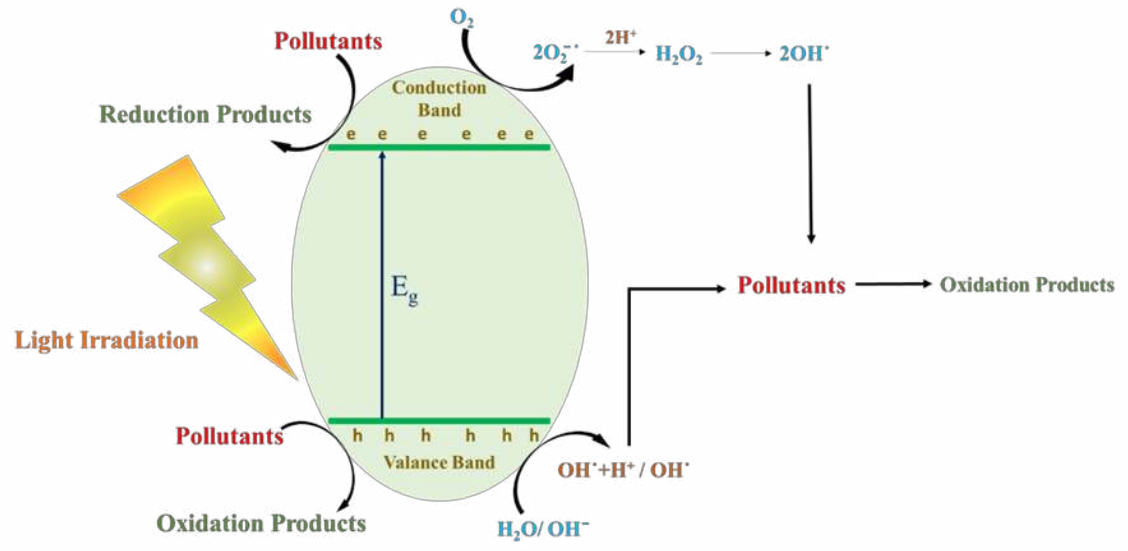

Figure 1.9: Schematic illustration of a simple photocatalytic process

1.6 General Mechanism of Photocatalytic H2O2 Generation

Photocatalytic H_2O_2 generation gains great prominence by means of sustainable nature of all process. In a typical process, solar light serves as an energy source and water/O_2 are resources to produce H_2O_2 in the presence of a semiconductor [14]. Similar to the pollutant degradation mechanism, sequential photocatalytic reactions initiate with excitation of photocatalyst by proper light, continued with photogeneration of electrons and holes. At the next step, these charges migrate to photocatalyst surface to create radicals as a result of a reaction with species adsorbed on catalyst surface. H_2O_2 can be produced photo catalytically in two ways. First of them is the oxygen reduction reaction (ORR) which can follow either an indirect two-step single-electron or a direct one-step two-electron reduction pathways [15]. Both ORR pathways start with the ionization of adsorbed water molecules by photogenerated holes to produce O_2 and protons (H^+) (**Eq. 1.10**). In the case of indirect route, e^-s in CB of photocatalysts undergo reaction with adsorbed O_2 molecules on catalyst surface and produce superoxide ($\bullet O_2^-$) radicals (**Eq. 1.11**). These $\bullet O_2^-$ radicals expose to another reaction with H^+ to form $\bullet HO_2^-$ (**Eq. 1.12**), followed by another single electron reduction, resulting in HO_2^- (**Eq. 1.13**). In the final step of this route, H_2O_2 is produced after reaction of HO_2^- and H^+ (**Eq. 1.14**). Direct one-step two-electron reduction pathway is displayed in **Eq. 1.15**. In this route, after the ionization of water, produced and adsorbed O_2 reacts with both two proton and $2e^-$ directly, forming H_2O_2 [14, 41]. In thermodynamics point of view, direct ORR route more convenient as required potential for direct ORR (+0.68 V) is more positive than that of indirect ORR (-0.33 V). On the other hand, the indirect reaction pathway utilizes one electron at each step, and it makes more feasible in the perspective of reaction charge kinetics. In addition, CB band potential is a significant criterion to proceed these reactions. CB potential of the semiconductor photocatalyst must be more negative than -0.33 V for coexisting of indirect and direct routes. If CB potential is between 0.68V and -0.33V, only direct ORR can occur thermodynamically. In the last scenario, if CB edge is more positive than 0.68 V, neither direct nor indirect ORR pathways cannot proceed [41].

Oxygen Reduction Reaction (ORR)

Indirect Two-Step Single-Electron Reduction

$2H_2O + 4h^+ \rightarrow O_2 + 4H^+$ $E^0 = +1.23$ V vs. NHE **(1.10)**

$O_2 + e^- \rightarrow \bullet O_2^-$ $E^0 = -0.33$ V vs. NHE **(1.11)**

$\bullet O_2^- + H^+ \rightarrow \bullet HO_2^-$ **(1.12)**

$\bullet HO_2^- + e^- \rightarrow HO_2^-$ $E^0 = +1.44$ V vs. NHE **(1.13)**

$HO_2^- + H^+ \rightarrow H_2O_2$ **(1.14)**

Direct One-Step Two-Electron Reduction

$2H_2O + 4h^+ \rightarrow O_2 + 4H^+$ $E^0 = +1.23$ V vs. NHE **(1.10)**

$O_2 + 2H^+ + 2e^- \rightarrow H_2O_2$ $E^0 = +0.68$ V vs. NHE **(1.15)**

Water oxidation reaction (WOR) on VB is another way to photo-catalytically generate H_2O_2, and it is also classified as indirect two-step single-electron and direct one-step two-electron WOR. When reactions follow indirect pathway, first, hydroxyl (•OH) radical is formed because of water oxidation with photo-induced holes (**Eq. 1.16**). After that, H_2O_2 is produced indirectly by two •OH radicals (**Eq. 1.17**). Oxidation of two water molecules by holes generates H_2O_2 and H^+ in the direct one-step two electron WOR [5]. When potentials of these reactions are considered, direct WOR is thermodynamically easier since it requires less energy (1.76 V) to proceed reaction as compared to indirect WOR (2.73 V). However, direct route uses two electrons at one step, and it affects reaction kinetics severely. Therefore, indirect WOR is kinetically more favorable despite requirement of high potential [41]. For WOR reactions, VB potential of semiconductor is important parameter. To drive direct WOR reaction, VB potential must be higher than 1.76 V. If VB is placed at a potential where is higher than 2.73 V, both indirect and direct reaction can be conducted at the same time [15]. In **Figure 1.10**, ORR and WOR pathways over a photocatalyst for H_2O_2 generation was illustrated.

Water Oxidation Reaction (WOR)

Indirect Two-Step Single-Electron WOR

$H_2O + h^+ \rightarrow \bullet OH + H^+$ $E^0 = +2.73$ V vs. NHE **(1.16)**

$2 \cdot OH \rightarrow H_2O_2$ **(1.17)**

Direct One-Step Two-Electron WOR

$2H_2O + 2h^+ \rightarrow H_2O_2 + 2H^+$ $E^0 = +1.76$ V vs. NHE **(1.18)**

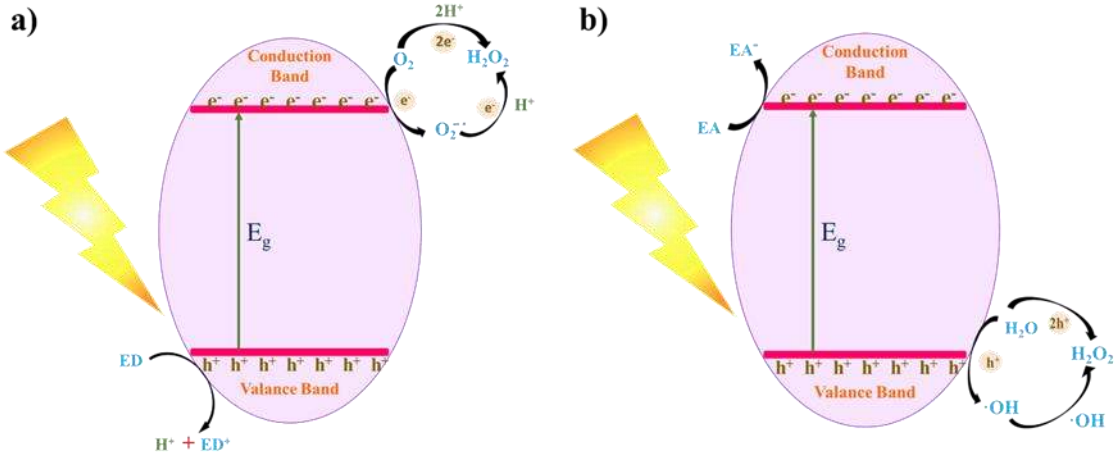

Figure 1.10: Schematic representation of light-driven H_2O_2 generation by **a)** ORR **b)** WOR *ED is electron donor and EA is electron acceptor.

1.7 Graphitic Carbon Nitride

Carbon nitride (C_3N_4) is one of the oldest synthetic polymers. In 1834, Berzelius synthesized C_3N_4 derivatives, and Liebig named this derivative as melon (**Figure 1.11a**). For the first time, Franklin mentioned the concept of C_3N_4. Then, Pauling and Sturdivant proposed that the tri-s-triazine unit is the motif that forms C_3N_4 structure in 1937. In the following years, it was revealed by Redemann and Lucas that melon and graphite resemble each other in planarity. Despite these studies, researchers could not elucidate structure of C_3N_4 in those years, and they stopped working on C_3N_4 until 1990s. In these years, scientists tried to synthesize β-C_3N_4 which has outstanding hardness and bulk modulus. However, they did not achieve β-C_3N_4 synthesis due to unsatisfactory thermodynamic stability. After this attempt, it was found that although C_3N_4 has different 7 allotropes, g-C_3N_4 is the most stable phase among these allotropes under ambient conditions [42, 43]. In the following years, the structure of g-C_3N_4 started to elucidate by improving advanced characterization techniques. With clarification of its structure, it was stated that g-C_3N_4 is formed by triazine (C_3N_3) and tri-s-triazine/heptazine (C_6N_7) rings which is thermodynamically favorable. (**Figure 1.11b-c**). One of the main targets of scientists is to obtain perfect, fully condensed crystalline g-C_3N_4. However, more stable tri-s-triazine units are very defect-rich blocks so it makes the synthesis of perfect g-C_3N_4

impossible. Also, the occurrence of defects in the structure results in an amorphous character, thereby low crystallinity, and it distorts stoichiometry [43, 44]. Therefore, g-CN notation is more realistic than g-C_3N_4. However, defect-rich structure brings some advantageous, mainly more active sites for reactions.

First application of g-CN as a photocatalyst is a water splitting reaction under visible-light irradiation in 2006 [45]. After that, graphitic carbon nitride has attracted all the attention in the scientific world thanks to its superior properties to be mentioned. g-CN is a polymeric semiconductor that has an indirect bandgap around 2.7 eV. Therefore, it can be activated with visible light. Based on normal hydrogen electrode (NHE), its VB and CB are located around 1.6 eV and -1.1 eV. These band positions, especially CB positions are excellent for a lot of photocatalytic reactions. The polymeric nature of g-CN ensures significant flexibility to structure. Therefore, g-CN is a great matrix for 1D and 0D materials. Although g-CN is a polymer, it possesses remarkable thermal stability up to 600 °C in the air. Moreover, g-CN has facile synthesis procedure. Its pristine form can be synthesized by thermal condensation of earth abundant, nitrogen-rich precursors for example dicyandiamide, melamine, thiourea and urea. However, as-synthesized g-CN is in 3D structure, and to utilize more exceptional properties, it should be exfoliated. Exfoliation is a method to obtain thinner structures by breaking Van-der Waals bonds between monolayers. Mechanical exfoliation, sonication-assisted liquid exfoliation, thermal exfoliation and combination of thermal and sonication-assisted liquid exfoliation are commonly used in the literature. As a result of exfoliation, thinner layer is obtained, and thinner structure reduces photogenerated electron-hole recombination rate and charge transfer resistance of g-CN. Also, exfoliation increases surface area. Despite of exfoliation, it is very challenging to obtain single layer g-CN. Lastly, it should be noted that depending on precursor and polymerization temperature, thermal, chemical, optical and photophysical properties of g-CN could differ widely [42-44, 46].

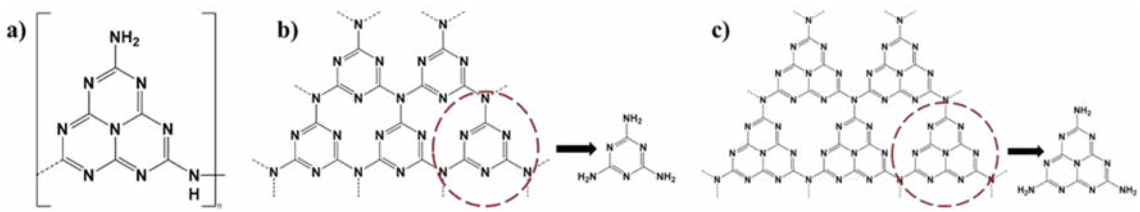

Figure 1.11: a) melon as derivative of C_3N_4, **b)** s-triazine **c)** tri-s-triazine (heptazine) as building blocks of g-CN

1.8 Oxygen-Deficient Tungsten Oxide

Oxygen-deficient tungsten oxide (WO_{3-x}) is a member of nonstoichiometric tungsten oxides. First usage of nonstoichiometric tungsten oxides dates back to the 17th century for the synthesis of tungsten bronzes, formulated as $M_x(W^{+6})_{1-x}(W^{+5})_xO_3$ (M= Na^+, K^+, Rb^+ ,Cs^+ and $0<x<1$). After the discovery of their electrochromic properties, diverse nonstoichiometric tungsten oxides have been gained to the literature for various applications. Furthermore, it was understood that WO_{3-x} with $0.3>x$ exhibits semiconducting material characteristic, and $W_{18}O_{49}$, W_5O_{14}, $W_{24}O_{68}$, $W_{20}O_{58}$, $W_{19}O_{55}$ belongs to this material group [47].

Structure of WO_{3-x} slightly differs from stoichiometric WO_3 with the introduction of oxygen vacancy, and reason of that is the presence of mixed-valance state of W, particularly W^{+5} and W^{+6}. While crystal structure of WO_3 is formed by generally corner-sharing of WO_6 octohedra building blocks, in the case of $WO_{3-x,}$ both corner and edge-sharing WO_6 octohedra are created. Because of increasing oxygen vacancy, WO_{3-x} starts to demonstrate crystallographic shear (CS) [48] (**Figure 1.12**). Moreover, in WO_{3-x}, apart from WO_6, structure can contain pentagonal bipyramid (MO_7) owing to edge shearing of five metal-oxygen octohedra, forming pentagonal column (PC) network. Another structural form called as hexagonal tunnel (HC) is built when two PC combine with corner-sharing of WO_6. These crystallographic knowledge shows that complex structure of WO_{3-x} as a product of stacked CS-PC-HC units [49].

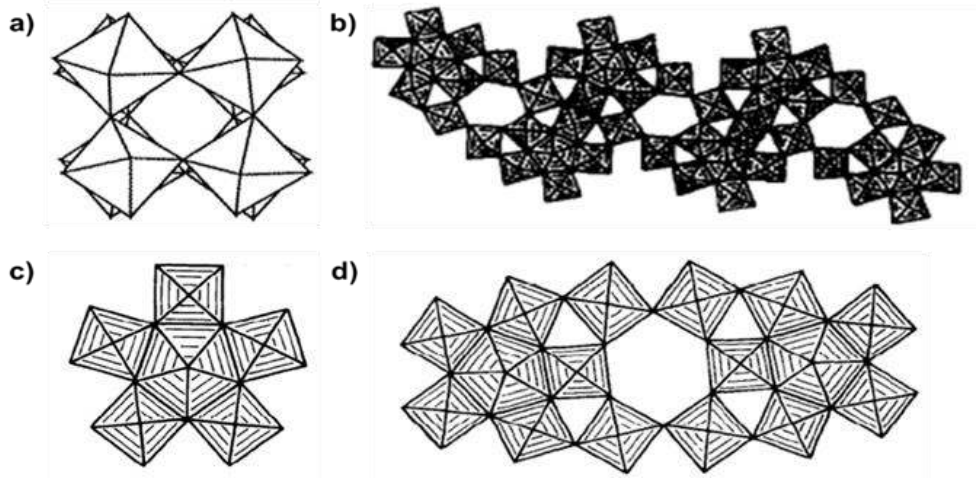

Figure 1.12: a) corner sharing of WO_6 octahedra in perfect WO_3 **b)** Crystal shear due to coexistencte of corner and edge sharing WO_6 octahedra **c)** Pentagonal column and **d)** CS-PC-HC in WO_{3-x} structure [49]

Change of oxidation state of W from (6+) to (5+) introduces oxygen vacancy in the structure due to deformed WO_6 octahedra [8]. The presence of oxygen vacancy increases the number of free electrons which cause the higher charge carrier density. In a stoichiometric WO_3, total charge carrier density is generally lower than 10^{20}, whereas this value for WO_{3-x} can reach to 10^{21}-10^{22}. Moreover, WO_{3-x} behaves as highly doped n-type semiconductor owing to excess number of electrons as charge carrier, resulting in accumulation of charges WO_{3-x} surface, and thus emergence of localized surface plasmon resonance (LSPR) property [8, 50]. However, LSPR is a phenomenon that can be only observed in nanomaterials, and if wavelength of incident light is larger than material dimensions, electron density decreases on the material surface interacting with light, and becomes stronger on non-interacting surface of the same material. Creation of asymmetrically distributed electron cloud activates restoring force exerted on positive nuclei and negatively charged electron, giving rise to collective oscillation of free electrons on semiconductor surface. Next, redistribution of electron clouds generates an electric field opposite to external electric field. Apart from coherent oscillations of free electrons and produces electric field are known as localized surface plasmons (LSP) [51]. In more detailed, optical extinction of a particle has maximum at plasmon resonance frequency that electrons oscillate with minimum energy dissipation, leading to LSPR. When frequency of incident light is consistent with resonant frequency, LSPR appears, and produces extremely strong localized electric field on plasmonic material surface [51, 52] (**Figure 1.13**).

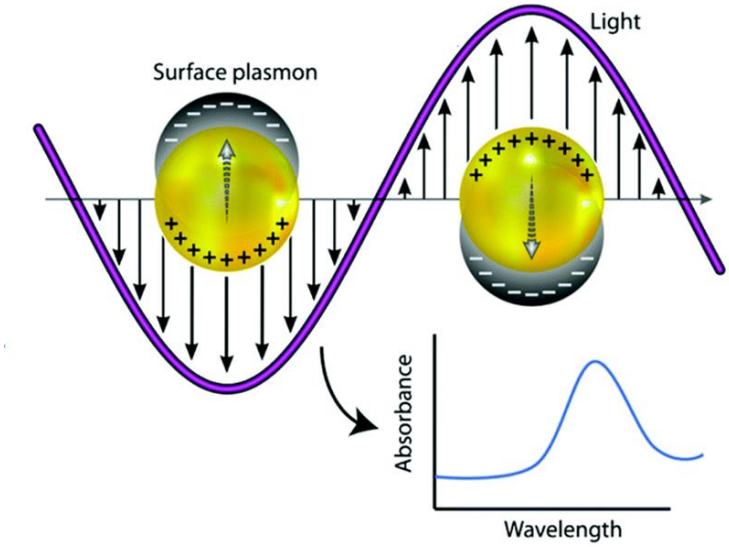

Figure 1.13: Localized surface plasmon resonanance creation over a plasmonic material [53]

LSPR property provides some advantages to WO_{3-x}. One of them is strong light absorption in the range of visible and NIR lights despite wider band gap of WO_{3-x}. In addition, LSPR peak position is tunable by controlling oxygen vacancy concentration. The second benefit associated with LSPR in WO_{3-x} is the production of hot electrons. Hot electrons are produced when LSPR is activated by appropriate light, and these energetic electrons supply the photothermal effect and extra electrons to the photocatalytic reaction [50], which will be evaluated in more detail in **Chapter 4**.

Herein, combination of g-CN with WO_{3-x} was designed to harvest ultrabroad range of solar spectrum, utilize hot electrons and their additional influences, and suppress radiative electron-hole recombination. Furthermore, performance of heterojunction photocatalysts was assessed in the photocatalytic MO degradation and H_2O_2 generation under visible light illumination.

Chapter 2:

LITERATURE REVIEW

2.1 Graphitic Carbon Nitride Based Heterojunctions

g-CN is a very propitious semiconductor photocatalyst owing to its facile synthesis procedure by using inexpensive precursors, moderate bandgap, proper band positions, nontoxic behavior, and delicate thermal and chemical stability. However, high e^-/h^+ recombination rate, its relatively low surface area and very limited light absorption ability in visible and near-infrared regions restrict its practical usage in industrial applications. To overcome aforementioned problems, construction of g-CN heterojunctions with other semiconductors is a viable design [54].

In the literature, g-CN was reported for different photocatalytic applications mainly pollutant degradation, hydrogen evolution, hydrogen peroxide production, carbon dioxide reduction and etc. [36, 54]. Previously type-II and Z-scheme, recently S-scheme heterojunctions of g-CN have received considerable attention thanks to their excellent designs.

Zhang and coworkers constructed 2D/2D BiOBr/g-C_3N_4 S-scheme photocatalyst by following in-situ self-assembly route. Besides its notable stability, the optimum photocatalyst 1.5BiOBr/g-C_3N_4 efficiently degraded 99% of 10 ppm Rhodamine B (RhB) within 30 minutes, and in H_2 generation reaction, heterojunction produced 106.63 $\mu mol \cdot g^{-1} \cdot h^{-1}$ while monocomponent BiOBr could not show any activity due to inappropriate CB potential, and activity of single g-C_3N_4 was measured as 31.66 $\mu mol \cdot g^{-1} \cdot h^{-1}$. Additionally, XPS results revealed that free electrons of g-C_3N_4 are transferred to BiOBr, and Brunauer-Emmett-Teller (BET) analysis showed that binary photocatalyst possesses higher surface area (60.72 m^2/g) than of pristine BiOBr (11.82 m^2/g) and pristine g-C_3N_4 (24.99 m^2/g), suggesting more active sites for a photocatalytic reaction [55]. Ahmad et al. fabricated a S-scheme ternary ZnO-g-C_3N_4-CuO heterosystem by using facile and rapid solution combustion process. Performance of photocatalyst was examined in methylene blue (MB) and RhB degradation. Under visible-light illumination, the synthesized ternary photocatalyst demonstrated 100% and 90% degradation performance within 35 minutes for MB and RhB respectively, and these ratios were higher compared to mono- and binary photocatalysts. With the creation of ternary system, the surface area of ZnO-g-C_3N_4-CuO

was the highest among all possible forms. Therefore, number of active sites and adsorption ability of ternary system increased that were vital for photocatalyst performance. Also, introduction to CuO into ZnO-g-C_3N_4 binary photocatalyst enhanced light harvesting ability toward visible-light regions, and assisted to effectual e^-/h^+ separation by creating intimate heterojunction. These results revealed why the ternary system works better in visible-light induced reactions [56]. $CuNb_2O_6$/g-C_3N_4 heterojunction was created with consecutive synthesis procedures known as co-precipitation and calcination by another group for wastewater treatment. In this regard, photocatalyst was performed in Cr(VI) reduction and RhB, MB and methyl orange (MO) degradations by preparing a mixture of pollutants under visible light irradiation. At the end of 2.5 hours, photocatalytic Cr (VI) reduction activity of binary heterojunction was measured to be 92.80% while its photodegradation efficiency for RhB, MB and MO was calculated as 99.6%, 98.5% and 99%, respectively. Rising photoactivity was attributed to transfer formation of Z-scheme heterojunction between individual semiconductors, providing fast charge transfer mechanism [57]. Very recently, our group also reported a novel ternary photocatalyst of BPQDs/CN-rGO for different applications such as MO and tetracycline (TC) degradation. Photodegradation efficiency of ternary heterojunction in MO and TC was calculated as 97% within 30 min and 96% for 120 min with the rate constants k= 0.1289 min^{-1} and 0.0291 min^{-1}, respectively. Furthermore, it is noted that the presented ternary heterojunction has a non-classical type II heterojunction, as the holes maintain their positions in the VB of CN-rGO even though the photogenerated electrons move from the BPQDs to the CB of the binary heterojunction CN-rGO. The proposed charge transfer pathway made possible production of $\bullet O_2^-$, $^1O_2$ and h^+, leading to superior activity in ternary heterojunction [58].

Zhao and coworkers designed Z-scheme noble-metal free $Bi_4O_5Br_2$/g-C_3N_4 photocatalyst for H_2O_2 generation. They synthesized the heterojunction by facile water-induced self-assembled method. In the first step, g-C_3N_4 was obtained through two steps thermal polymerization of melamine which initial heating procedure was 550°C for 4 hours and second was 500°C for 2 hours. $Bi_4O_5Br_2$ nanorods were produced via colloidal synthesis containing stirring for 10 days. After 10 days, the certain amount of g-C_3N_4 joined into colloidal mixture, followed by dropwise addition of water, and stirring along 8 hours to obtain $Bi_4O_5Br_2$/g-C_3N_4 heterostructure. By applying visible light, the H_2O_2 generation performance of optimum photocatalyst $Bi_4O_5Br_2$/g-C_3N_4 was measured as 124

μM for 60 min in O_2-equilibrated and no-scavenger conditions, and this production rate was around 25 times and 62 times higher than single g-C_3N_4 and $Bi_4O_5Br_2$, respectively. The improved H_2O_2 evolution rate under visible light irradiation was attributed to the construction of binary heterojunction which results in an increment in e^-/h^+ separation and redox ability [59]. Wang et al. proposed C_3N_4/ $NiIn_2S_4$ heterostructure for photocatalytic H_2O_2 production, and the calculated yield was 1080 μmol·L^{-1}·h^{-1} in the presence of 10 wt% ethanol as electron donor and O_2-saturated environment. Heterojunction was synthesized by in-situ solvothermal growth of $NiIn_2S_4$ with lamellar structure on 2D g-C_3N_4 layers. Thanks to intimate contact of g-C_3N_4 and $NiIn_2S_4$, enhanced light absorption and therefore an effective photohermal conversion, offering higher photoactivity was stated [60]. Liu and colleagues synthesized hierarchically porous ZnO/g-C_3N_4 S-scheme photocatalyst through two-step calcination method. Photocatalytic H_2O_2 evolution reaction was performed for ZnO/g-C_3N_4 binary photocatalyst and its individual components. For heterojunction, photocatalytic H_2O_2 production was recorded as 1544 μmol·L^{-1}·h^{-1} which activity was enhanced 3.4 times and 5 times in comparison to respective g-C_3N_4 and ZnO. Reasons of improved photoactivity in binary heterojunction was associated with S-scheme charge transfer mechanism, supplying effective charge separation, strong redox capability and improved light absorption ability. Additionally, pores in the structure created alternative charge migration pathways and plentiful active sites for H_2O_2 generation [61]. Another group designed cobalt single-atom supported on sulfur doped graphitic carbon nitride/reduced graphene oxide (Co-CN@G) photocatalyst for H_2O_2 formation from natural seawater. They demonstrated that synergism between Co single atoms and CN@G heterostructure and photothermal effect accelerated H_2O_2 formation by separating photo-induced charges effectively and reducing energy barrier of ORR and WOR. The formed H_2O_2 from natural seawater with no-scavenger was determined as 8.29 mM at the end of 10 hours in simulated solar light [62]. Chen et al. constructed a 2D/2D g-C_3N_4/In_2S_3 by hydrothermal synthesis to illuminate charge flow mechanism during photocatalytic H_2O_2 formation. Under simulated solar light along 120 min, the synthesized binary heterojunction exhibited 294 μmol/L H_2O_2 yield which is higher than 36.4 μmol/L of pristine g-C_3N_4. Moreover, they showed that the formed heterojunction exhibited type-I structure since electrons and holes of g-C_3N_4 had tendency to flow on In_2S_3. However, scavenger experiments proved that while electrons in CB of g-C_3N_4 flow to CB of In_2S_3, the holes of g-C_3N_4 remain in its VB, causing

effective charge separation and accelerating two-step single-electron reduction pathway which was the reason of high activity in g-C_3N_4/In_2S_3 [63]. Das and coworkers designed 0D/2D Fe_2O_3/B-g-C_3N_4 by in-situ nucleation of Fe_2O_3 on B-doped g-C_3N_4. Photocatalyst was used for H_2O_2 generation in 5% isopropanol and O_2-saturated conditions. It exhibited the highest H_2O_2 yield as 729 $\mu mol \cdot g^{-1} \cdot h^{-1}$ whilst activity of B-g-C_3N_4 and Fe_2O_3 was limited with 371 $\mu mol \cdot g^{-1} \cdot h^{-1}$ and 86 $\mu mol \cdot g^{-1} \cdot h^{-1}$. Determination of O_2^- and ·OH radicals with the help of scavenger experiments and terephthalic acid (TA) test, and XPS analysis which confirms electron flow from Fe_2O_3 to B-g-C_3N_4 revealed that S-scheme heterojunction type was formed between B-g-C_3N_4 and Fe_2O_3, explaining high activity [64].

2.2 Oxygen Deficient Tungsten Oxide Based Heterojunctions

WO_{3-x} has gained great attention due to its LSPR property. With appropriate light, LSPR phenomena enables production of hot electrons in the semiconductor that accelerating the reaction kinetics and providing more electron to photochemical reaction [8]. Besides, its relatively low cost and abundancy in the nature as compared to noble metals with LSPR like Au, Ag and Cu along with nontoxic character and stability in extreme conditions makes WO_{3-x} intriguing candidate for solar energy utilization [65]. On the other hand, similar to other metal oxide semiconductors, WO_{3-x} has wider bandgap and relatively positive conduction band that is inadequate for some chemical reactions [66]. To eliminate drawbacks of WO_{3-x} and achieve superior photoactivity, construction of WO_{3-x}'s heterojunctions with other materials is acceptable strategy. In this regard, especially Z-scheme and S-scheme heterojunctions of WO_{3-x} are available for use in different photocatalytic applications such as dye and antibiotic degradation, organic transformations, H_2O_2 and H_2 generation in current literature.

Yan and coworkers designed a core-shell photocatalyst that TiO_2 spheres were covered by WO_{3-x}, denoted by TiO_2@WO_{3-x} for photodegradation of MB. Thanks to presence of WO_{3-x}, core-shell structure utilized full solar spectrum, and EPR results proved that under NIR irradiation, TiO_2@WO_{3-x} had ability to produce free electrons and reactive oxygen species. MB degradation experiments were conducted in only UV, visible and NIR irradiation for 250 min to compare photocatalysts' performance. TiO_2 exhibited satisfactory photoactivity for MB degradation under UV (k_{UV}= 0.064 min^{-1}) and

visible light (k_{Vis}= 0.012 min^{-1}) but its performance is extremely poor (k_{NIR}= 6.4×10^{-4} min^{-1}) in NIR light source. On the other hand, WO_{3-x} show photocatalytic activity in the presence of UV (k_{UV}= 0.016 min^{-1}), visible (k_{Vis}= 0.0048 min^{-1}) and NIR light (k_{NIR}= 2.3×10^{-3} min^{-1}), however degradation efficiency at these lights are not good enough. In addition, photodegradation performance of TiO_2@WO_{3-x} was higher than that of pure forms TiO_2 and WO_{3-x} under UV (k_{UV}= 0.90 min^{-1}), visible (k_{Vis}= 0.017 min^{-1}) and NIR illumination (k_{NIR}= 7.0×10^{-2} min^{-1}) [67]. Another group proposed a ternary photocatalyst $Bi_7O_9I_3$/$Cd_{0.5}Zn_{0.5}S$ QDs/WO_{3-x} to use in photodegradation of phenol. The photocatalyst performance in phenol degradation was 4.02, 3.75 and 5.71 times higher than pure $Bi_7O_9I_3$ under full spectrum, visible and NIR irradiation, respectively. Moreover, under full spectrum, phenol degradation performance of ternary heterojunction was 100% within 60 min while at the same conditions, parent semiconductors $Bi_7O_9I_3$, $Cd_{0.5}Zn_{0.5}$ and WO_{3-x} exhibited photoactivity of 38.1%, 10.1% and 24.3%, respectively. The exceptional degradation efficiency of ternary photocatalyst was expressed by construction of double S-scheme which created alternative channels for charge migration, and utilization of full solar spectrum that was demonstrated with UV-DRS. Besides, EPR results and trapping experiments uncovered •OH and $\bullet O_2^-$ radicals were fundamental roles in degrading phenol [68]. Yang et al. constructed 0D/2D $W_{18}O_{49}$/ZnI_2S_4 by using hydrothermal route for ZnI_2S_4 synthesis and a simple water-bath heating procedure to form binary heterojunction. Selective oxidation of benzyl alcohol (BA) to benzaldehyde (BAD) was applied to $W_{18}O_{49}$/ZnI_2S_4 nanocatalyst. Although individual semiconductors and binary heterojunction disclosed highly selective (>99%) for oxidation of benzyl alcohol to benzaldehyde, conversion of BA to BAD was limited with 22.4% and 3.7% for $ZnIn_2S_4$ and $W_{18}O_{49}$, respectively. In case of binary heterojunction, conversion to BAD was 68.6% within 3 hours. The extraordinary increment in photocatalytic performance with creation of $W_{18}O_{49}$/ZnI_2S_4 was expressed by three reasons. First reason was fruitful spatial separation and transfer kinetics of photogenerated charges on the grounds of the formation of Z-scheme heterojunction type between ZnI_2S_4 and $W_{18}O_{49}$. Second was increase in light harvesting ability of heterojunction thanks to LSPR of $W_{18}O_{49}$. Based on experimental and DFT results, the last one was to generate abundant $\bullet O_2^-$ radicals by easier and faster activation of molecular oxygen by virtue of synergism between photothermal effect and continuous formation of hot electrons [69]. Z-scheme tandem heterojunction of WS_2 QDs/MoS_2@WO_{3-x} core-shell was synthesized by another group

for degradation of 2,4-Dichlorophenol (DCP). The photodegradation performance of core-shell structure was measured as 97% for 120 min along with the rate constant k=0.03569 min^{-1} which was higher than MoS_2 (k= 0.00201 min^{-1}), WO_{3-x} (k=0.00158 min^{-1}) and WS_2 (k=0.00089 min^{-1}). The enhanced photodegradation efficiency in WS_2 QDs/MoS_2@WO_{3-x} was ascribed to several reasons. First of all, improved charge separation thanks to Z-scheme tandem heterojunction formation, and increased light absorption ability and photothermal effect providing by plasmonic WO_{3-x}. Additionally, as TEM images revealed, MoS_2 has nanosphere morphology but these nanospheres comprised of stacking of MoS_2's lamellar form. It was understood that the random stacking of lamellar structures enabled more active sites in edges and higher surface area to core-shell structure. The last one was that inadvertently doping of oxygen into MoS_2 crystal structure during synthesis procedure. In this way, recombination of charges was suppressed, and their lifetime were prolonged, leading to higher photocatalytic performance [70]. Huang et al. created 3D flower-like WO_{3-x}/Bi/BiOCl hierarchical Z-scheme heterojunction via solvothermal method. Its performance was evaluated to rhodamine B (RhB) degradation under different light. Results were 100% within 8 min, 100% within 3 min and 96% within 120 min at UV, visible and NIR light by turn while under same durations, photoactivity of Bi/BiOCl against RhB degradation was measured as 84% for UV, 88% for visible and 41% for NIR light. As compared to UV light, further enhancement of photodegradation in visible light was attributed to photosensitization of RhB at approximately 556 nm, causing increase in electrical conductivity at heterojunction. Outstanding performance of ternary photocatalyst was mainly associated to presence of WO_{3-x} since light harvesting ability of WO_{3-x}/Bi/BiOCl extended from 250 nm to 2500 nm. In addition, authors stated that flower-like structure with high surface area paved the way adsorption of RhB molecules [71]. Jiang and colleagues constructed S-scheme heterojunctions NH_2-MIL-125-Ti/WO_{3-x} with low, moderate and high oxygen vacancy concentration for photogeneration of CO and H_2O_2 from CO_2 and H_2O with addition of no-scavenger. Since introduction of oxygen vacancy into structure changes the Fermi level position, authors proposed that proper oxygen vacancy concentration in WO_{3-x} provides larger difference between Fermi levels of oxidation and reduction semiconductors, sparking stronger built-in electric field at interface that improves charge separation and migration by conserving high redox potential of S-scheme heterojunction. In this regard, heterojunction that was formed by WO_{3-x} with moderate oxygen vacancy

concentration possessed the most powerful built-in electric field, and concurrent photocatalytic formation of CO as 12.57 μmol·g^{-1}·h^{-1} and of H_2O_2 as 8.41 μmol·g^{-1}·h^{-1} was detected, which was 8.01 and 6.62 times higher than NH_2-MIL-125-Ti [72].

2.3 Graphitic Carbon Nitride/Oxygen Deficient Tungsten Oxide (WO_{3-x}) Based Heterojunction Photocatalysts

Combination of g-CN with another semiconducting materials is frequently used strategy to suppress electron-hole recombination and to increase light gathered ability of g-CN. At this point, nonmetallic but plasmonic WO_{3-x} semiconductor with its cheapness, nontoxicity, higher oxidation potential, facile synthesis and appealing optical properties serves as outstanding candidate to form heterojunction with g-CN. A photocatalyst of g-CN/WO_{3-x} is a promising heterojunction for different applications thanks to fascinating properties of heterojunction.

Recently, the number of studies focusing on g-CN/WO_{3-x} photocatalyst and its ternary versions has been increasing to use in different applications such as water remediation, H_2 formation, sterilization and H_2O_2 generation. In this regard, some studies in the current literature was summarized in the following section.

In the first study, WO_{3-x}/g-C_3N_4 binary heterostructure was constructed by using one-step annealing method to investigate the specific merits such as influence of vacancy concentration and heterojunction formation on photocatalytic activity. Binary photocatalyst was tested in RhB and TC degradation and bacteria killing. Photodegradation efficiency of g-C_3N_4, WO_{3-x} and WO_{3-x}/g-C_3N_4 was measured as 48%, 6% and >99% with the rate constants k= 0.042 min^{-1}, k= 0.003 min^{-1} and k= 0.291 min^{-1} in order against 10 ppm RhB within 15 minutes. At TC degradation experiments, under LED illumination for 100 min, performance of binary heterojunction was detected as 68% with rate constant k= 0.021 min^{-1}, which was higher than that of pure g-C_3N_4 (58%, k= 0.013 min^{-1}) and WO_{3-x} (25%, k=0.004 min^{-1}). As a last application, disinfection experiments revealed that while WO_{3-x}/g-C_3N_4 photocatalyst killed bacteria by 15% under dark conditions, it could kill bacteria completely with light illumination, which 64% and 34% of bacteria was eliminated for g-C_3N_4 and WO_{3-x}. Improved photoactivity at these applications was explained by layered structure of g-C_3N_4 with more active site, enhanced light absorption of binary photocatalyst on account of vacancies in WO_{3-x}, and

formation of heterojunction, quenching the photo-induced charge recombination [73]. Shang and colleagues designed 1D/1D $W_{18}O_{49}$/g-C_3N_4 to serve in different photocatalytic applications. They synthesized double-layer hallow g-C_3N_4 (CNNT) via hydrothermal synthesis, followed by calcination. TEM images demonstrated that $W_{18}O_{49}$ was wrapped on g-C_3N_4 after additional solvothermal reaction for formation of hybrid H_2 generation, RhB degradation and antibacterial test was chosen to illuminate multifunctional nature of binary photocatalyst. H_2 generation reactions was conducted by adding 3wt% Pt on the present photocatalyst, and the first result was H_2 generation rate of CNNT was 5.97 times higher than bulk-CN, and pristine $W_{18}O_{49}$ had no ability to produce H_2 at these reaction conditions. Besides, 1D/1D $W_{18}O_{49}$/ g-C_3N_4 heterojunction produced 4.67 $mmol \cdot g^{-1} \cdot h^{-1}$ H_2, and when experiments were conducted at light having 700 nm wavelength, binary heterojunction maintained production of H_2 thanks to hot electron produced from $W_{18}O_{49}$ while CNNT did not work at the same wavelength. Degradation efficiency of 1D/1D $W_{18}O_{49}$/ g-C_3N_4 was measured as 100% in 12 min while its sterilization performance was 99.41% within 20 min. The calculated work functions and EPR uncovered that S-scheme heterojunction was established between CNNT and $W_{18}O_{49}$. As indicated in the simulations and DFT calculations, apart from S-scheme heterojunction formation (**Figure 2.1a**), another factor that enhances the performance was that wrapping of $W_{18}O_{49}$ onto CNNT enabled strengthening of localized electric field and light absorption [74]. Zhang et.al developed a plasmonic photocatalyst $W_{18}O_{49}$/g-C_3N_4 with the aid of facile solvothermal method for photocatalytic proton reduction. Photocatalytic water reduction reaction was tried to observe performance of binary heterojunction by adding 1.0 w % Pt as cocatalyst. Results show that it produces 15.2 $\mu mol \cdot h^{-1}$ H_2 which has 3.2 times more than g-C_3N_4 under solar simulator. Furthermore, at 700 nm wavelength, $W_{18}O_{49}$/g-C_3N_4 had activity for production of H_2 thanks to hot-electron flow to heterojunction while parent semiconductors g-C_3N_4 and $W_{18}O_{49}$ did not how any activity at this wavelength owing to extremely limited light absorption of the former, and inadequate CB potential of the latter one. After these outcomes, they proposed a synergism between Z-scheme heterojunction and noble-metal like LSPR-induced hot electrons since these provided effective charge separation and extra charge generation, conducing improved photoactivity within ultrabroad spectrum [50]. Another group created binary heterojunction by growing $W_{18}O_{49}$-onto two dimensional CN via solvothermal synthesis. Artificial photosynthesis of H_2O_2 by using binary heterojunction was achieved under 10

wt% isopropanol solution and O_2-saturated conditions, and production was measured as 732.4 $\mu mol \cdot g^{-1} \cdot h^{-1}$, followed by λ >700 nm experiments which elegant performance of heterojunction was 140.5 $\mu mol \cdot g^{-1} \cdot h^{-1}$. XPS analysis demonstrated W-N bond forms at the interface of two semiconductors, making easier charge flow and separation. Also, it was proven that enhancement in electric field within LSPR wavelength range lowered the adsorption energy of O_2. In addition, band alignments of CN and $W_{18}O_{49}$ indicated formation of Z-scheme heterojunction, rendering charge recombination (**Figure 2.1b**). These mentioned results were used to explain why the photocatalytic H_2O_2 production in the heterostructure increases [75]. Li and coworkers synthesized S-doped porous g-C_3N_4 (S-pCN) /$WO_{2.72}$ heterojunction via solvent evaporation induced self-assembly method by using ethanol. They proposed that the formed heterojunction has S-scheme charge transfer mechanism due to synthesis procedure and oxygen vacancies of WO_{3-x} alongside proper band position of pristine semiconductors. Since ethanol is a small molecule, it passed pores of S-pCN, and this caused concentration difference between inside and outside of pore. In this way, $WO_{2.72}$ easily attached pores of S-pCN with the help of diffusion process provided by osmatic pressure. Moreover, XPS results unveiled that solvation step in solvent evaporation method led to formation of ·OH groups on S-pCN and lone pairs of electron on the S atom in S-pCN. Hydrogen bond formation between ·OH group and lone pair electrons of S-pCN and oxygen vacancies of $WO_{2.72}$ increased strength of interfacial contact, resulting in compact S-scheme heterojunction formation.

To analyze activity of photocatalyst, TC and RhB degradation along with H_2 and H_2O_2 generation were selected as model reactions. While binary photocatalyst degrade RhB 100% within 20 min, and TC 85% within 120 min, its hydrogen evolution reaction activity was detected as 786 $\mu mol \cdot g^{-1} \cdot h^{-1}$. In the case of H_2O_2, without using any sacrificial agent, 87 μM H_2O_2 was produced from DI water within 180 min. For this case, heterojunction exhibited higher activity than their pristine forms, which attributed to S-scheme heterojunction with strong interface contact [76]. C_3N_4/N-doped carbon quantum dots (N-CQDs)/ $W_{18}O_{49}$ ternary heterojunction was constructed for photocatalytic degradation of MB, MO, TC and ciprofloxacin (CIP) mixture .Under full spectrum (λ>365 nm), degradation efficiencies of photocatalyst for MB, MO, TC and CIP were almost 100% within 90 minute, 100% within 120 minute, 99.6% and 99.5% within 180 min by turn, while their photoactivity in NIR were calculated as 83.7%, 82.8%, 83.4% and 84.5% in the same order at the end of 180 minutes. Ternary heterojunction

photocatalyst exhibited higher activity than their individual forms in all case which is associated with several reasons. First of them, LSPR of $W_{18}O_{49}$ improved charge separation efficiency, and produced hot electrons to heterojunction, resulting in full-spectrum-response of photocatalyst. The second was integration of N-CQDs to $C_3N_4/W_{18}O_{49}$ as N-CQDs forms the additional channels to shorten charge transfer distance and enhance charge separation between C_3N_4 and $W_{18}O_{49}$. The final one was formation of Z-scheme heterojunction type, providing effective charge separation and preserving of charges having high redox ability [77]. Zhang et al. developed WO_{3-x}/S doped g-C_3N_4 (SC_3N_4) for photoremoval of pharmaceuticals and personal care products, naproxen and diclofenac. Photodegradation percentage of naproxen and diclofenac were 99.2% within 25 min and 99.5% at 60 min, respectively which is higher than those of SC_3N_4 and $W_{18}O_{49}$. Moreover, photocatalyst had ability to degrade naproxen and diclofenac under NIR irradiation since introduction to $W_{18}O_{49}$ improved to light absorption ability of SC_3N_4 in the range of Vis and NIR. Moreover, transient photocurrent responses showed that S-doping into g-C_3N_4 has positive influence on charge separation. Additionally, Mott-Schottky analysis and work function calculations revealed that S-scheme heterojunction was formed between individual semiconductors, suppressing charge recombination while retaining charges with high redox potential [78]. In another study, Hong and coworkers created a ternary heterojunction $W_{18}O_{49}$/Au/g-C_3N_4 photocatalyst for H_2 generation. While $W_{18}O_{49}$/g-C_3N_4 heterostructure was fabricated through solvothermal method, integration of Au (2 wt%) onto binary heterostructure was achieved with photodeposition, followed by solvothermal procedure. Photocatalytic H_2 production activity of $W_{18}O_{49}$/g-C_3N_4 and $W_{18}O_{49}$/Au/g-C_3N_4 was found as 1785 $\mu mol \cdot g \cdot h^{-1}$ and 3465 $\mu mol \cdot g \cdot h^{-1}$ in turn under 1h solar light. These results ascribed to Z-scheme heterojunction formation proved by UPS. Even though Z-scheme heterojunction of $W_{18}O_{49}$/g-C_3N_4 enabled to high redox capability and efficient spatial charge separation, as a mediator Au deposition over binary heterostructure accelerated charge-transport dynamic more, explaining higher photoactivity in $W_{18}O_{49}$/Au/g-C_3N_4. Additional rationales in improved activity were extension of light gathering ability from visible to NIR thanks to LSPR effects of both $W_{18}O_{49}$ and Au [79]. In the last research, to utilize in photocatalytic H_2O_2 generation and disinfection, Z-scheme of rGO decorated $W_{18}O_{49}$@g-C_3N_4 ternary heterojunction was developed via solvothermal method. Its performance under solar simulation, visible and NIR light in photocatalytic H_2O_2

formation was determined as 71, 58.5 and 6.5 $\mu mol \cdot g^{-1} \cdot h^{-1}$ while g-C_3N_4's generation rate was limited as 54, 29 $\mu mol \cdot g^{-1} \cdot h^{-1}$ and no detection, in order. For sterilization experiments, E.coli inactivation was selected as model reaction, and under light irradiation at 60min, ternary heterojunction, g-C_3N_4 and $W_{18}O_{49}$ killed E. coli bacteria 6.3 log CFU mL^{-1}, 4.2 log CFU mL^{-1} and 2.4 log CFU mL^{-1}. Enhancement photoactivity of rGO decorated $W_{18}O_{49}$@g-C_3N_4 was endowed by synergism of integration with $W_{18}O_{49}$ and decoration with rGO as a co-catalyst over g-C_3N_4 to obtain a productive Z-scheme heterojunction (**Figure 2.1c**). To be clearer, introducing $W_{18}O_{49}$ enhanced light absorption ability apart from providing higher oxidation potential to Z-scheme while addition of rGO extra sped up photo-induced electron migration to oxygen reduction sites [80].

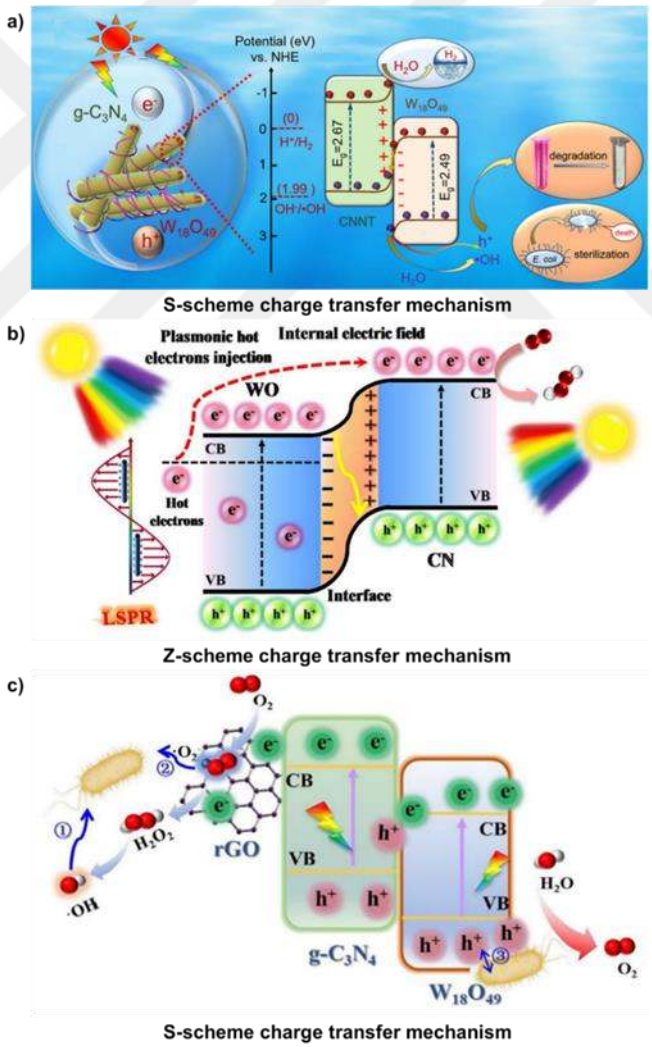

Figure 2.1: Proposed charge transfer and separation pathways for reported g-CN/WO_{3-x} heterostructures. Reprinted from **a)** Ref. [74] **b)** Ref [75] and **c)** Ref. [80]

Chapter 3:

MATERIALS AND METHODS

3.1 Chemicals

Urea (≥99.5 GR for ACS reagent, IsoLab), Tungsten hexachloride (WCl_6 ≥99.9% trace metal basis, Sigma-Aldrich), Sodium tungstate dihydrate ($Na_2WO_4.2H_2O$≥99%, ACS reagent, Sigma-Aldrich), 1,4-benzoquinone(BQ ≥ 98%,Sigma-Aldrich), Triethanolamine (TEOA ≥ 99.0%, Sigma-Aldrich), Potassium iodide (KI ≥ 99.5 % for analysis EMSURE, Supelco), Potassium hydrogen phthalate (KHP ≥ 99.5 % for analysis EMSURE, Supelco), Methyl orange (MO, 85%, ACS reagent, Sigma-Aldrich), Sodium hydroxide (NaOH ≥ 98%, pellets, Sigma-Aldrich), Terephthalic acid (TA>98%),hydrogen peroxide (H_2O_2, 30% in water, Sigma-Aldrich), Ethanol absolute (≥99.9, IsoLab), Methanol (≥99.7, Honeywell Riedel-de Haën), 2-propanol (≥99.5, IsoLab), 1-butanol (≥99.5, Sigma-Aldrich), Ethylene glycol (≥99, Sigma-Aldrich, Nitric acid (HNO_3 >65% ,IsoLab), Hydrochloric acid (HCl, 37%, IsoLab) and Deionized water (DI, 0.055 $\mu S.cm^{-1}$)

3.2 Synthesis Procedures of Photocatalysts

3.2.1 g-CN Synthesis

g-CN was synthesized by the thermal polycondensation of urea without using a template [81]. In a typical g-CN synthesis, 25 g urea was grinded in a porcelain mortar along 15 min, and it was transferred into a quartz crucible. After the lid of crucible was closed, it was placed into muffle furnace with the heating program. According to the initial step of the heating program, the furnace was heated to 80 °C with 15 °C/min and kept at this temperature for 1 hour, followed by increasing temperature to 550°C with the same heating rate. After keeping crucible at 550°C for 4 hours, the heating program was ended with cooling to oven to room temperature. The obtained pale-yellow product was grinded again, and stored in dark environment to protect it from sunlight irradiation.

3.2.2 Stoichiometric WO_3 Synthesis

A literature method was used to synthesize stoichiometric WO_3 [82]. In a typical synthesis of WO_3, 5 mL of nitric acid (65%) was added dropwise into 25 mL DI water,

and solution was stirred for 10 min. In another flask, 1.5 mmol of $Na_2WO_4.2H_2O$ was dissolved in 10 mL DI water until obtaining homogeneous solution and the resultant solution was transferred into nitric acid/water solution. Upon the addition, a precipitate was observed, and the color of the mixture changed from white to bright yellow. The final suspension was stirred for another 30 min, and it was taken to Teflon-lined autoclave. The heating program for 180 °C for 3 hours was applied. After cooling the reactor room temperature, the yielded material in the autoclave was transferred to two centrifuge tubes (50 mL) and centrifugations were performed by two times, first in DI water and finally in EtOH at 9000 rpm for 10 minutes each. To dry the final product, it was kept at 70 °C overnight, and stored in dark.

3.2.3 WO_{3-x} Synthesis

WO_{3-x} was synthesized by solvothermal method. WCl_6 was used as W precursor. 130 mg of WCl_6 was weighted, and 26 mL methanol (MeOH) was poured on it in a glass bottle, and color of system became mustard. Mixture was sonicated for 4 hour, and solution's color turned to pale navy blue. After sonication, solution was put in Teflon-lined autoclave, and it was located into muffle furnace. The furnace was heated to 180°C within 30 minutes, and autoclave was kept at this temperature for 18 hours. When reactor cooled to room temperature, material was taken into two centrifuge tubes with 50 mL, and MeOH was added on them, followed by centrifuge at 8000 rpm for 10min. In addition to this, material was centrifuged two times by using ethanol (EtOH) as a solvent at 8500 and 9000 rpm for 10 minutes in turn. To dry the material, vacuum rotary evaporator was used. Finally, the obtained WO_{3-x} with pale navy-blue color was stored in dark.

3.2.4 g-CN/WO_{3-x} Heterojunction Photocatalyst Synthesis

250 mg of g-CN was dispersed in 50 mL EtOH, and dispersion was sonicated for 3 hours. After sonication process, solution was divided into 2 centrifuge tubes with 50 mL volume, followed by centrifuge with EtOH at 9000 and 8500 rpm for 15 minutes each, respectively. g-CN was dried at 70°C overnight. Later, 100 mg of g-CN was weighted from the prepared batch, and 80 mg WCl_6 with 26 ml MeOH was added on exfoliated g-CN. Similar to WO_{3-x} synthesis, sonication in ultrasound bath was applied to mixture for 4 hours. Color of the mixture seemed as iridescent by the reason of presence of yellowish

g-CN. After sonication, mixture was poured into Teflon-lined autoclave, and the same heating procedure of WO_{3-x} which is 180°C for 18 hours was applied to autoclave at the muffle furnace. The material cooled to room temperature was taken into 2 centrifuge tubes with 50 mL volume. For first centrifuge at 8000 rpm for 10 min, MeOH was added to centrifuge tubes. EtOH was used for the other 2 centrifuges, which were conducted at 8500 and 9000 rpm for 10 min each, respectively. Vacuum rotary evaporator was used to dry the synthesized g-CN/WO_{3-x} heterojunction. The color of final product is similar to light mint green. The synthesized binary heterojunction was preserved in dark.

3.2.5 g-CN/WO_3 Heterojunction Photocatalyst Synthesis

g-CN/WO_3 heterojunction photocatalyst was synthesized via a physical mixing of g-CN a d WO_3 dispersions. 250 mg of exfoliated g-CN and 100 mg of the prepared stoichiometric WO_3 was added on 25 mL DI water. By turn, stirring for 30 min and sonication for 1 hour was applied to the suspension. After these steps, the suspension was divided into 4 centrifuge tubes with 50 mL volume. Centrifugation with DI water at 1200 rpm for 10 min was used to collect precipitates. The final product was ground and stored in dark after drying at 80 °C for 10 hours.

3.3 Photocatalytic Methyl Orange Degradation Experiments

Methyl Orange (MO) degradation experiments was performed in double-jacketed glass reactor under constant stirring by applying water circulation to control the reaction temperature around 25°C. Firstly, 30 mg photocatalyst was dispersed in 5 ml DI water for 15 minutes, and 100 mL, 5 ppm MO solution in DI water was prepared. By taking 3 mL solution from reactor, intensity of MO characteristic peak around 464 nm was detected via UV-Vis Absorbance Spectroscopy. After that, the dispersed photocatalyst was added into glass reactor under constant stirring. To reach adsorption-desorption equilibrium, mixture was stirred for 1 hour in dark conditions, and 3 mL samples were taken from reactor at 15 minute intervals. 3 mL suspension was syringed with 0.20 μm syringe filter, and change in intensity of peak was observed. At the end of 1 hour, halogen lamb (white light, 150 W) turned on, and 3 mL samples were taken with 5 minute time intervals , followed by filtering (0.20 μm syringe filter), and change in absorbance was analyzed numerically through absorbance spectrophotometer. Relation between

reduction in absorbance intensity and degradation efficiency was calculated by using **Eq. 3.1** where C_0 is initial concentration and C_t is instantaneous concentration at a given time. For this purpose, a calibration curve of MO was prepared (**Figure 3.1**). After determination of degradation efficiency, first-order reaction equation (**Eq. 3.2**) was applied to find rate constant (k) of MO degradation reaction at given time.

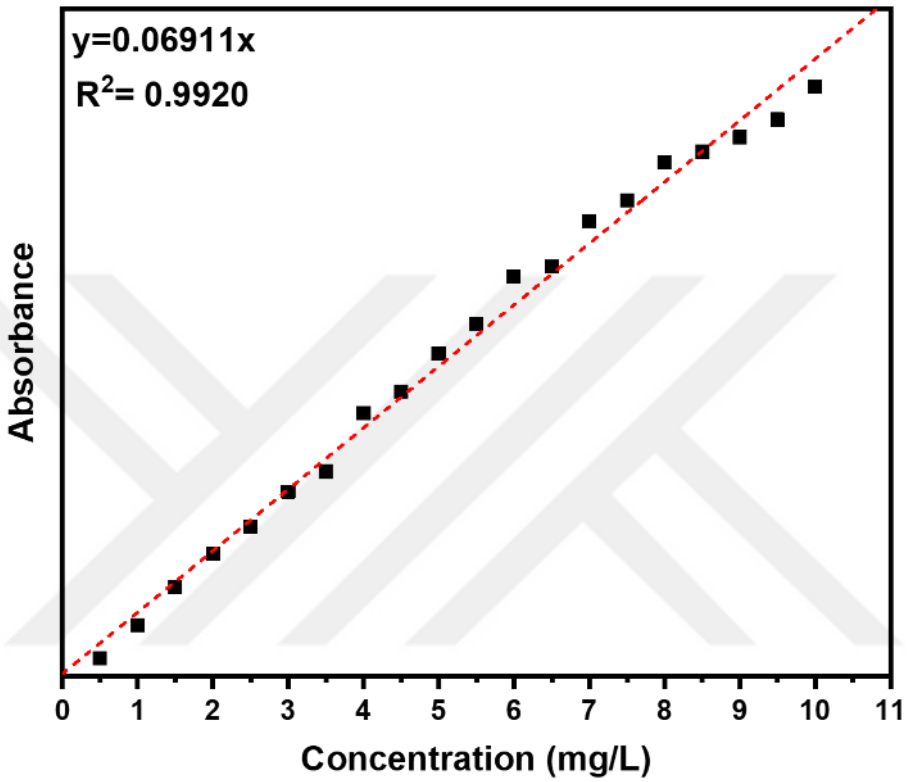

Figure 3.1: Calibration curve of MO

$$\text{Degradation Efficiency (\%)} = \frac{C_0 - C_t}{C_0} \times 100 \quad \textbf{(3.1)}$$

$$\ln(C_0/C_t) = kt \quad \textbf{(3.2)}$$

3.4 Photocatalytic Hydrogen Peroxide Generation Experiments

Photocatalytic hydrogen peroxide (H_2O_2) formation experiments was conducted at the same photoreactor system. 50 mg photocatalyst was dispersed in 5 ml DI water for 15 min while 50 mL DI water solution containing 10 wt% methanol as a hole scavenger was stirred in double-jacketed glass reactor. Starting with initial concentration of H_2O_2 in the

absence of photocatalyst, 3 mL of solution was taken from glass reactor at 15 minute intervals until 90 minute. After measurement of initial concentration, dispersed catalyst was added into solution. In this case, 0.22 µm syringe filter was used for removal of catalyst from 3 mL sample. Iodometric spectrophotometry was used for detection of H_2O_2. In this method, photocatalytically produced H_2O_2 reacts with KI to form yellow-colored triiodide (I_3^-) [83]. Therefore, 0.1 mL of 0.4 M KI and 0.1 mL of 0.1 M KHP was added to taken sample, and 4 minutes was waited to complete following reaction (**Eq. 3.3**). Thanks to strong absorbance of I_3^- at 350 nm, amount of generated triiodide was decided by UV-vis absorbance spectroscopy (JASCO V730) at the end of 4 minutes. For determination of produced H_2O_2 numerically, a calibration curve was constructed (**Figure 3.2**).

$$H_2O_{2(aq)} + 3I^-_{(aq)} + 2H^+ \rightarrow I^-_{3(aq)} + 2H_2O \qquad \textbf{(3.3)}$$

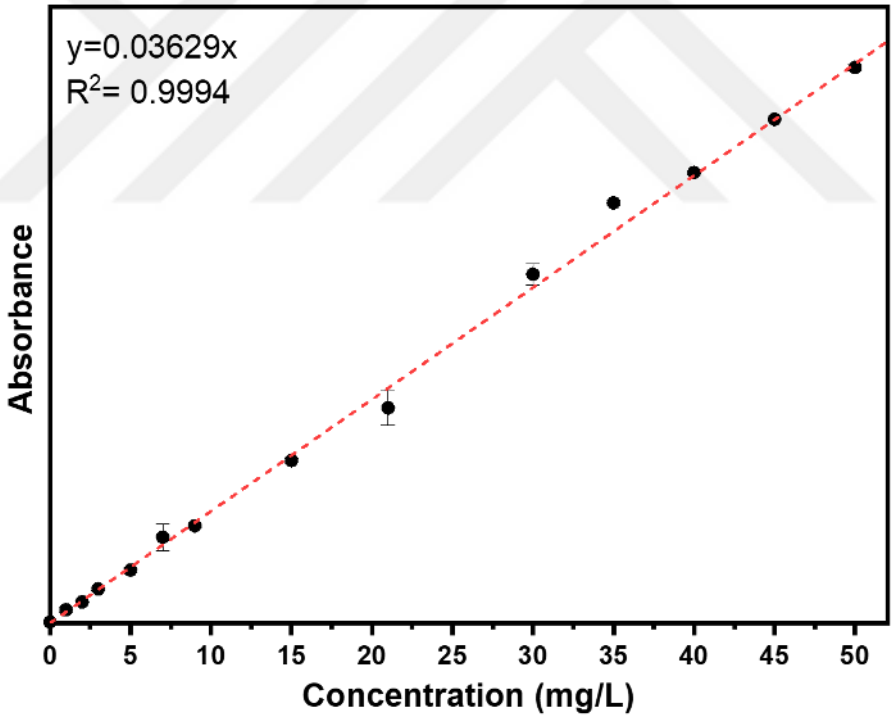

Figure 3.2: Calibration curve of H_2O_2

3.5 Scavenger Experiments

Same reactor and experimental system was used to conduct scavenger experiments. 1,4 benzoquinone (BQ), triethanolamine (TEOA) and isopropanol (IPA) as 3 equivalent

for each was used to scavenge electron/ superoxide ($\bullet O_2^-$) radical, hole (h^+) and hydroxyl (•OH) radicals, respectively. Just before turning on the light, the related scavenger was added to the reaction medium. After the light source turned on, measurements were made at 5-minute intervals in accordance with the described MO degradation experimental procedure.

3.6 Terephthalic Acid (TA) Experiments

A solution of TA (1×10^{-3} M) and NaOH (4×10^{-3} M) was prepared at the beginning. 10 mg of photocatalyst was added onto this solution followed by stirring. First sample was taken in dark conditions from reaction environment, and then, it was syringed. At the next step, light was illuminated [84]. At 15, 30, 45, 60, 75 and 90 minutes under light irradiation, samples were taken from reaction environment, and analyzed with PL spectroscopy (Agilent Cary Eclipse) for hydroxylated terephthalic acid formation (HTA). Because it is a PL-active molecule around 430 nm, and HTA is formed if ·OH radicals are present in reaction medium.

3.7 Hot Electron Experiments

H_2O_2 generation was selected for determination of hot electrons, and experiments were performed at glass vial with 30 mL volume by applying green light (530 nm, LED, 24W). In the first step, 20 mg photocatalyst was dispersed in 5 mL DI water for 15 min, and 20 mL solution with 10 wt % MeOH was prepared. 3 mL sample was taken from stirred solution, and iodometric spectrophotometry was used as mentioned in **chapter 3.4**. After addition of catalyst, samples were taken with 15 minute intervals until 90 minutes, and the same route of H_2O_2 generation was applied.

3.8 Recyclability Measurements

Experimental procedure of MO degradation was applied for recyclability tests. By considering the photocatalyst loss at successive measurements, recyclability experiments were started with 50 mg photocatalyst in 100 mL MO solution (5 ppm), and number of measurement was reduced. At the end of each cycle, a certain amount of MO was added to reaction environment to keep the amount of pollution constant at 5 ppm. Recyclability tests continued until a drastic activity loss was observed at the conducted cycle.

3.9 Instrumentation

Raman analysis was performed by using Renishaw Invia Raman Microscope equipped with 532 nm excitation laser. XRD pattern was obtained through Bruker D2 Phaser-X-ray Diffractometer using Cu Kα radiation (λ= 1.54 Å). SEM analysis was conducted by Zeiss Sigma 300. TEM and EDX analysis at low magnification was employed by Hitachi HT7800 120 kV (S)TEM equipped with Oxford EDX detector. HRTEM, high-angle annular dark field (HAADF), scanning transmission microscope (STEM) and elemental mapping images was recorded by Hitachi HF5000 200 kV (S)TEM with Oxford instrument for EDX analysis. XPS measurements were conducted at Thermoscientific k-alpha X-ray phototoelectron spectrometer with Al Kα (hv= 1468.3 eV). Avantage software was used for fitting of raw XPS data. Bruker 500 MHz Ascend Neo NMR spectroscopy with MASSB-DR-BBLR CPMAS H/X VTN 4 mm double resonance probe for SB solid state was used for ssNMR of C^{12} and H^{1} NMR. Optical properties of material was analyzed with ultraviolet-visible-near-infrared spectroscopy (UV-vis-NIR DRS) through Shimadzu UV-3600 UV-Vis-NIR Spectrophotometer. Reflectance data were converted to absorbance by using Kubelka-Munk equation. Also, $BaSO_4$ was utilized as reference material. Photoluminisence measurements were performed at Agilent Cary Eclipse PL (350 nm) spectrometer. By using Edinburgh Instruments FLS1000 spectrometer with 377 nm wavelength excitation source, TRPL analysis was applied. For electrochemical analysis which are Mott-Schottky, transient photocurrent (TPC) and electrochemical impedance spectroscopy (EIS), Gamry interface 1010 potentiostat was used. Transient photocurrent measurements were conducted under AM 1.5 G illumination of the Solar Light-16 S solar model (1 sun, 100 mW/cm^2). Under light conditions, EIS measurements were employed in the presence of light at 10 mV AC voltage and 0.1-100 kHz frequency range.

3.10 Characterization Methods

In this section, the working principles of characterization methods that were employed in this thesis study were explained briefly.

3.10.1 Structural and Chemical Characterization

Raman

Raman spectroscopy is a non-destructive technique to analyze chemical structure, phase, crystallinity and molecular interaction of a material. Moreover, it is used to identification of material through characteristic Raman fingerprint. The Raman effect stems from inelastic scattering of light known as Raman scattering due to interaction with molecules [85]. In a typical Raman scattering, interaction of incident light with molecule gives rise to distortion of electron cloud around the nuclei and nuclear motion to create vibrational states which is not stable, permitting re-emission of light as scattering. During Raman scattering, either energy of incident light is transferred to molecule (Stokes scattering), or molecule's energy is transmitted to incident photon (anti-Stokes scattering), resulting in energy difference between incident and scattered photons by one vibrational unit. A Raman spectrum is drawn according to shifting of incident photons' energies, denoted by cm^{-1} [86].

X-ray Diffraction (XRD)

XRD is a nondestructive technique to determine the crystal structure and phase of the material. Also, it can be used for chemical composition detection and crystallite size calculation [87]. A XRD data is a result of constructive interference of monochromatic X-ray beam and crystalline material. In a clear way, when incident X-ray hits the material, light scatters at all directions. Due to periodic arrangement of crystalline materials, a special case "constructive interference" occurs, which they are detected and counted (**Figure 3.3**). After that, the characteristic diffraction pattern of a phase was obtained based on intensity of diffracted rays which scatter at different angles. Therefore, a XRD pattern is drawn as intensity on y-axis against angle of detector, 2θ on x-axis [88, 89]. Furthermore, lattice spacing between two planes can be found through Bragg's law (**Eq. 3.4**) where n is order of diffraction, λ is wavelength of X-ray, and θ is angle between incoming/diffracted light and material [90].

$$n\lambda = 2d_{hkl} \sin\theta \qquad \textbf{(3.4)}$$

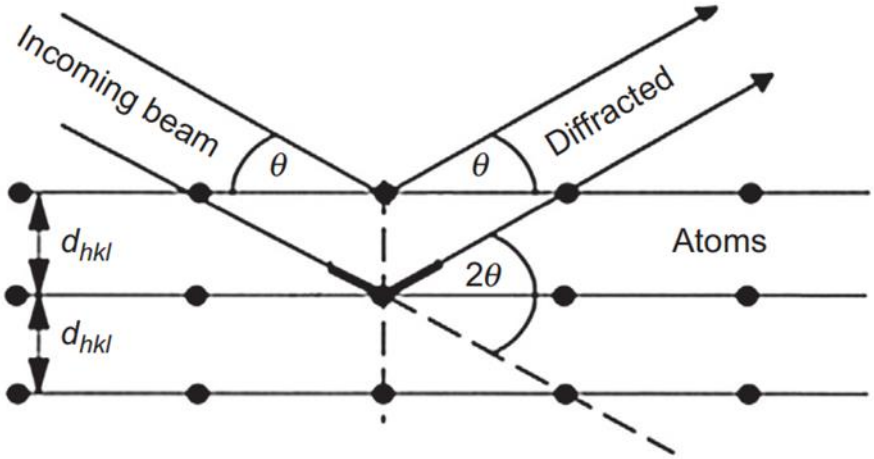

Figure 3.3: Illustration of diffraction phenomena on a crystalline material [88]

Scanning Electron Microscopy (SEM)

SEM is a frequently preferred nondestructive imaging technique to analyze morphology, topography and chemical composition of a material by scanning the surface. In a typical SEM, highly-energetic electron beam is produced by an electron gun, and they are focused on a spot over material surface through a series of magnetic lenses. After sending of electron beam onto specimen, electron-matter interaction produces Auger, secondary, backscattered electrons as well as X-ray mainly gathered and processed by different detectors (**Figure 3.4**). Secondary and backscattered electrons are the most important data providers in SEM analysis. Secondary electrons are inelastically ejected from near-surface, and they are less energetic than backscattered electrons. When these electrons are detected, they gives information about surface texture and roughness of specimen with high resolution. Elastic collision of primary electron and specimen generates energetic back-scattered electrons, providing images about topography and chemical composition with remarkable contrast [91, 92]

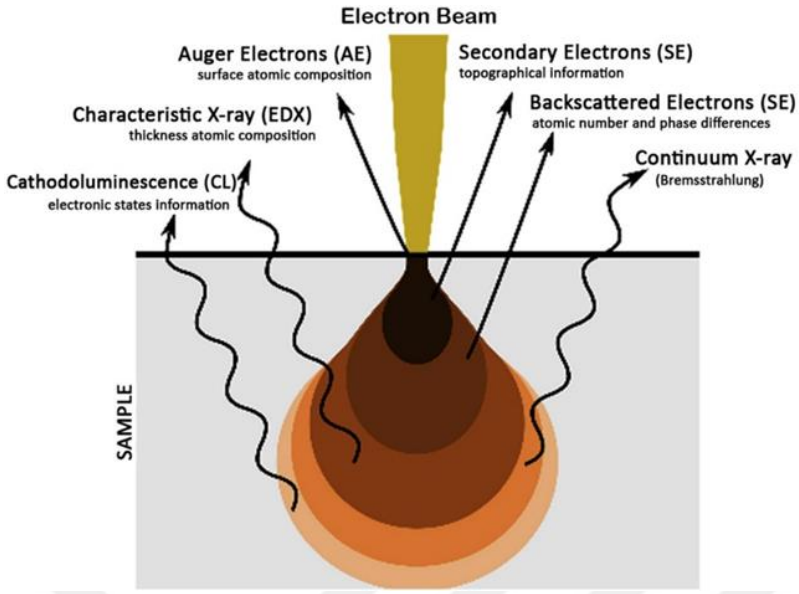

Figure 3.4: Interaction of electron beam with analyzed material [93]

Transmission Electron Microscopy (TEM)

Basic equipment of TEM are electron gun, a set of magnetic lenses and detectors, similar to SEM. While energy of electron beam exceeds to 100 keV in TEM with constant current density, mission of condenser lens is focusing of beam onto specimen. When the incident beam interacts with sample, some of the beam are scattered and remaining ones are transmitted. The objective lenses project on transmitted beams to generate an image. After that, intermediate and projector lenses serve for magnification of generated image. Since transmission of beam on specimen is important to obtain an image, the prepared samples as thin as possible. Therefore, TEM analysis is usually employed in nanomaterials [94].

High resolution transmission electron microscopy (HRTEM) is a more specialized mode of conventional TEM for investigation at atomic scale. In HRTEM, electron beam interacts with crystal lattice and is diffracted, resulting in complex interference patterns. Through some transformation, patterns are used for providing data about crystallographic structure including defects [95].

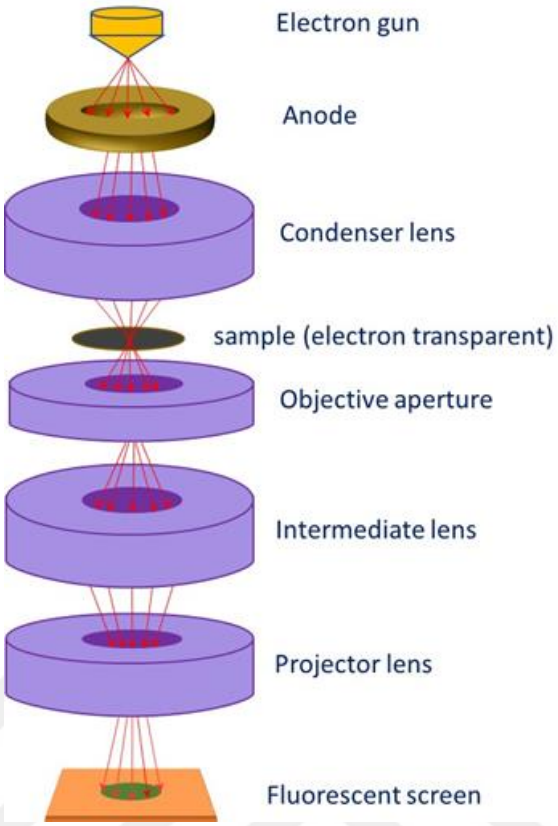

Figure 3.5: Schematic representation of TEM [96]

Energy Dispersive X-ray (EDX) Spectroscopy

EDX analysis is a technique to clarify the chemical composition of a material in (S)TEM analysis [97]. In a material, electron bombardment produces continuous Bremsstrahlung and characteristic X-rays. Identification of elemental composition through EDX is achieved by utilizing characteristic X-rays. This type of X-rays is generated as a consequence of the transition of electrons in electronic states, and they are specific for each element. A detector in EDX instrument collects these generated characteristic X-rays based on their energies. After a set of process, energy of characteristic X-rays are compared to the energy of a specific element in the material via references in database, and in this way, elemental mapping of the analyzed material is obtained [95, 98].

X-ray Photoelectron Spectroscopy (XPS)

XPS is an extremely surface sensitive technique restricted to 2-10 nm. Its working principle based on photoelectric effect phenomena. In short, the photoelectric effect defines that photon with appropriate energy makes the ejection of electrons from the material surface possible [99]. This technique informs about the qualitative elemental analysis of composition, electronic states and chemical environment of these elements along with valance band structure [100].

In the XPS analysis, incident soft X-rays with energy hν causes removal of electrons with some kinetic energy (E_{KE}) from the inner levels under valance shell. The difference between energy hν and E_{KE} gives the binding energy (E_{BE}) which is specific to element [99, 101]. **Eq. 3.5** is used to explain mathematically the relation among the mentioned energies, where ϕ_{Spec} is work function of instrument. Thanks to particular binding energy, this technique can be used for analysis of all elements in the periodic table except H and He due to presence of only one orbital in their configuration [99].

$$E_{BE} = h\nu - E_{KE} - \phi_{Spec} \quad \textbf{(3.5)}$$

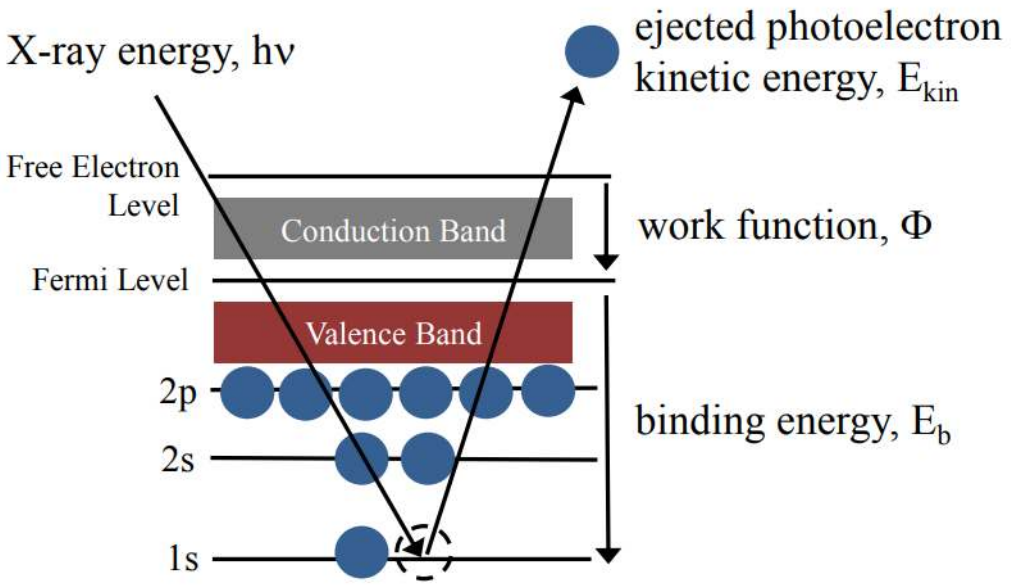

Figure 3.6: Diagram for explanation of photoelectron phenomena behind XPS [102]

Valence Band X-ray Photoelectron Spectroscopy (VB-XPS)

In a typical XPS Survey spectrum, the range of 0-30 eV points out valance electrons in the outer shell [99]. At these binding energies, a large number of energy levels which are overclose to each other forms a band structure, namely valance band. High resolution XPS within this range enable to assign valance band (VB) potential [103]. By applying **Eq. 3.6,** the obtained VB from plot is converted to V vs. NHE [104].

$$E\ (V\ vs\ NHE) = E_{VB\text{-}XPS} + \phi_{Spec} - 4.44 \quad \textbf{(3.6)}$$

3.10.2 Photophysical Characterization

Ultraviolet-Visible-Near Infrared Diffuse Reflectance Spectroscopy (UV-Vis-NIR DRS)

UV-Vis-NIR DRS produces optical data by collecting the reflected lights from material surface. Generally, for opaque and powder materials, DRS is more suitable rather than absorbance or transmission modes because of scattering of light through different directions. Kubelka-Munk function (**Eq. 3.7**) converts reflectance data to absorbance, considering that all incident lights are scattered or absorbed for thick enough sample. In the **Eq. 3.7**, R_∞ is reflectance of infinitely thick material, K is absorption coefficient and S is scattering coefficient [94]. After reflectance/absorbance transformation, to find optical bandgap of a semiconductor, Tauc Plot is constructed with the help of **Eq. 3.8** where α is energy-dependent absorption coefficient, h is Planck constant, ν is frequency of photon, B is constant and Eg is bandgap of material. γ becomes 0.5 or 2 according to bandgap character of semiconductor. If semiconductor has indirect bandgap, γ value is 2 or its bandgap is direct, γ is 0.5. In a Tauc Plot, the point where the tangent line intersects the x-axis is used to estimate the band gap of any semiconductor [105, 106].

$$F(R_\infty) = \frac{K}{S} = \frac{(1 - R_\infty)^2}{2R_\infty} \quad \textbf{(3.7)}$$

$$(\alpha h\nu)^{1/\gamma} = B(h\nu - E_g) \quad \textbf{(3.8)}$$

Photoluminescence (PL) Spectroscopy

PL spectroscopy informs about movement of electrons from excited state to ground state as detecting fluorescence after photoexcitation of charges with a laser beam. It gives a plot of emitted light intensity as a function of wavelength. In a semiconducting material, recombination of photogenerated electrons falling from CB with holes in VB produces a strong fluorescence emission, known as radiative recombination [94]. Therefore, PL is a practical technique to detect and evaluate radiative recombination rate of different semiconductors and their heterojunctions [107].

Time-Resolved Photoluminescence (TRPL) Spectroscopy

TRPL is an advanced analytical technique that luminescence of emissive materials is measured as a function of time. It is frequently used to follow photoinduced charge transfer and recombination kinetics of semiconducting materials [108]. TRPL measurement gives information about radiative and nonradiative decay. Radiative recombination (τ_2) or decay indicates band to band movement of photogenerated charges, and it is based on emission of photon. Volume and surface recombination describes radiative recombination. On the other hand, nonradiative recombination (τ_1) term is used for vibration of lattice that produce phonon. By applying following formula (**Eq. 3.9**), τ_{avg} value which defines the required time for charges to reach surface is calculated [8].

$$\tau_{avg} = \frac{(\tau_1 * A_1 + \tau_2 * A_2)}{(A_1 + A_2)} \quad \textbf{(3.9)}$$

The basic components of a TRPL spectrometer are a tunable pulsed laser, a spectrograph and an intensified CCD camera (**Figure 3.7**) [109]. Pulsed laser source generates excitation radiation that has wavelength within spectral range of UV-Vis-NIR. Spectrograph and intensified CCD camera serve as detectors. Spectrograph resolved emission coming from the sample spectrally within the UV-Vis-NIR region. After spectrograph, the emission was detected by intensified CCD camera [109, 110]. When incoming luminescence strike the photocathode at the entrance of intensified CCD camera, electrons are released. At the next step, by applying high voltage, both number of these electrons multiplied and also they accelerate in the Micro-channel Plate. These accelerated electrons hit the phosphorous coated fluorescent screen, resulting in releasing

of photons again. At the surface of CCD, intensified photons are used for data acquisition [110].

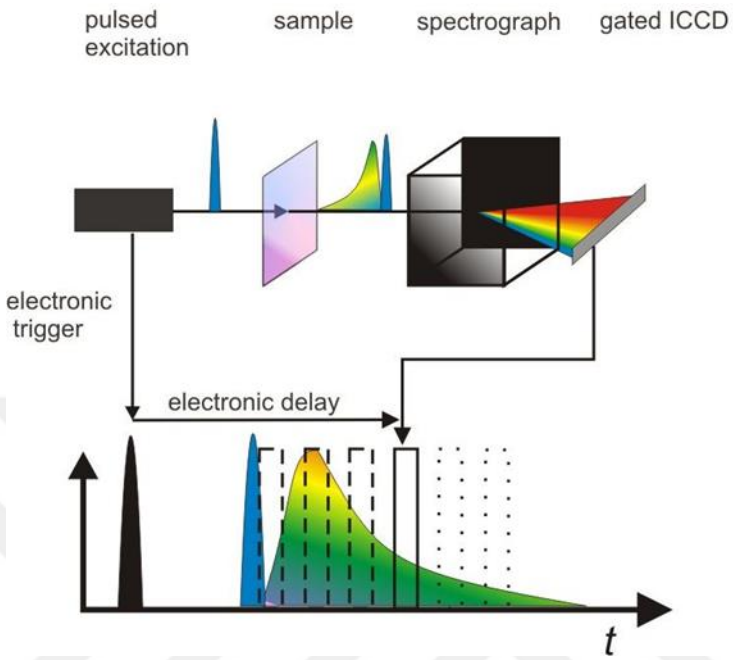

Figure 3.7: Schematic representation of a typical TRPL instrument [111]

3.10.3 Electrochemical Characterization

All electrochemical measurements were conducted in three electrode system with 0.1 M Na_2SO_4 solution. Electrodes are working electrode (WE), Pt counter electrode (CE) and Ag/AgCl (3M KCl) reference electrode (RE) . 2 mg material and 50 µL nafion were dispersed in 5 mL ethanol, and sonicated during 1 hour. Indium tin oxide (ITO) was cleaned separately and respectively with water, ethanol, and acetone by sonication for 15 min each. After these, 60 µL sample solution was dropped onto ITO, and they were dried under room conditions [112].

Electrochemical Impedance Spectroscopy

EIS is utilized to analyze matter-electrode interactions such as mass-transfer, charge-transfer and diffusion behavior. From photocatalysis view, it is preferred to investigate interfacial properties and charge transfer kinetics of heterostructures and their individual forms [113]. First of all, impedance is a general name of opposition to electron flow in a circuit. In a dc circuit, only unit producing impedance is resistors whereas inductors and capacitors are also included in ac circuit. In this regard EIS measurement is applied to

obtain an impedance spectrum within a range of frequency. In a typical EIS measurement, small-amplitude stimulus in the form of voltage or current is applied to system, and response of a system in a wider frequency range was gathered as a voltage or current output. Nyquist plot is graphed by using the obtained impedance data, and for each examined frequency, imaginary part (Z") and real part (Z') of impedance are plotted over y-axis and x-axis respectively, forming a semicircle shape [114]. By interpreting semicircle radius, kinetics and dynamics of material is interpreted.

Transient Photocurrent Measurement

Transient photocurrent method (TPC) is mostly applied in light-driven applications to survey charge carrier transfer across semiconductor/ electrolyte interface. As a result of perturbation of material with modulated light, photocurrent is recorded as a function of time. TPC measurements are performed in a short-curcuit containing a small resistor. By applying laser pulse, a perturbation is created a transient current measured by oscilloscope parallel to resistor [115]. Due to usage of square excitation pulse, light-on and light-off positions are utilized to measure current change. At the light on mode, photogenerated carriers are produced with switching on of excitation pulse, result in increment in photocurrent. Higher current offers effect production of charge carriers and their successful spatial separation. On the one hand, light-off mode demonstrates that carriers decay after pulse turns off, and current becomes almost zero [94, 116].

Mott-Schottky Analysis

Flat band potential (V_{fb}) represents the potential where the conduction and valance bands are flat. In other words, since it is a specific potential to destroy space-charge layer between semiconducting material and electrolyte, there is no junction or band-bending at flat-band potential [117]. As the flat band potential is associated with the Fermi level of the semiconductor, determining this potential is an important point to estimate the band diagram of a semiconductor [118]. Using **Eq. 3.10**, the flat band potential can be transformed to the Fermi level of the material [119].

Mott-Schottky analysis is widely preferred to detect band structure and semiconductor type. A Mott-Schottky plot is built with inverse-square of capacitance ($1/C^2$) on the y-axis, and reverse voltage (V) on the x-axis. As seen from the **Figure 3.8**, dependence of $1/C^2$ is linear to V, and slope of this linear function gives information about

semiconductor type while interception point of slope and x-axis show the V_{fb}. Furthermore, charge carrier density of semiconductors can be calculated through slope of plot [120]. On condition that slope is positive once applied potential (V) is bigger than V_{fb}, semiconductor is n-type due to presence of depletion layer. In the case of p-type semiconductor, slope is negative owing to accumulation [121].

$$E_F \text{ (V vs NHE)} = V_{fb} \text{ (V vs NHE)} = V_{fb} \text{ (V vs Ag/AgCl)} + 0.205 \text{ V} \quad \textbf{(3.10)}$$

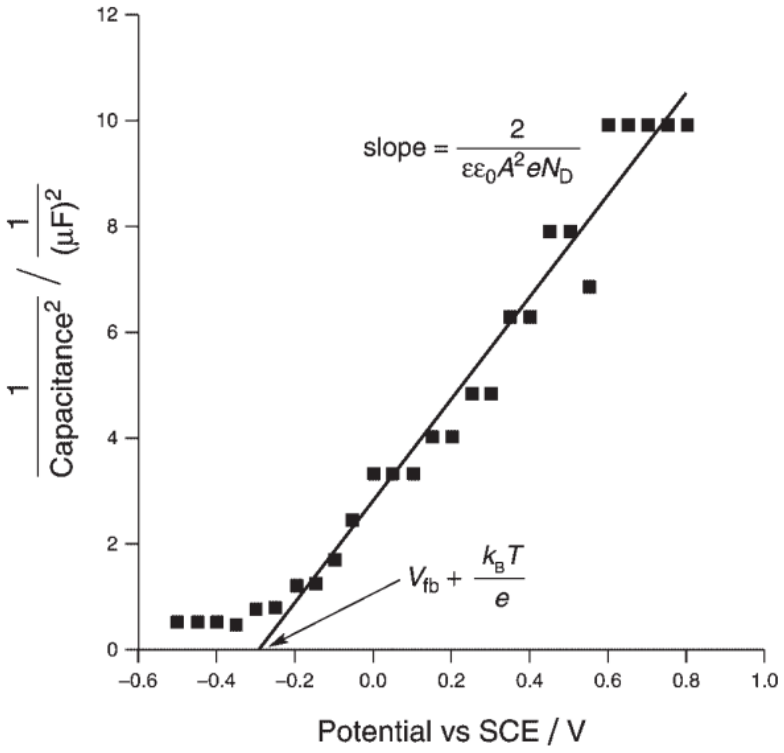

Figure 3.8: A Mott-Schottky plot giving flat-band position [120]

Chapter 4:

RESULTS AND DISCUSSIONS

4.1 Optimization of gCN/WO_{3-x} Synthesis Parameters

In the literature, WO_{3-x} is synthesized by either vapor-phase or solution-based methods [47]. Compared to vapor-phase synthesis such as chemical vapor deposition (CVD) and physical vapor deposition (PVD), solution-based methods are more commonly preferred owing to their simplicities and scalability for large-scale production. Colloidal and solvothermal methods are two well-known solution-based procedure to synthesize WO_{3-x} [47]. Solvothermal method is easier and scalable, and it produces less waste in comparison to colloidal ones. Moreover, the solvothermal method provides stronger interaction in heterojunction synthesis [122]. In this study, in-situ solvothermal synthesis of WO_{3-x} on g-CN nanosheets was achieved in one-pot. Besides, it was claimed that reaction temperature/time, solvent type and concentration of WCl_6 (mg/mL) are very critical parameters effecting the plasmonic property, morphology and activity of the yield g-CN/WO_{3-x} photocatalyst. In this thesis, these factors were evaluated comprehensively. Additionally, it was considered whether there could be a synergism between plasmonic property-morphology and activity. To prove these hypotheses are principal motivation of this thesis project. Furthermore, there is no scientific study that evaluate all these parameters together. In this regard, the results of the current thesis will make significant contribution to the photocatalysis, photonics, and sterilization fields.

4.1.1 Determination of precursor amounts at initial procedure

In the literature, researchers have generally preferred ethanol (EtOH) as a solvent in the solvothermal synthesis of WO_{3-x} at 180°C for 12 hours [50, 123]. Moreover, Li and co-workers reported that optimum concentration between amount of WCl_6 and EtOH is 5 mg/mL [124]. In this regard, 100 mg well-exfoliated g-CN nanosheets and 60 mg WCl_6 were determined as starting amounts, and to find the optimum concentration accurately, solvothermal treatment was applied to 160 mg of starting materials in 12 mL, 22 mL and 32 mL EtOH. The main criterion when deciding on solvent amount was to keep ratio of 5 mg/mL constant by adjusting 60 mg WCl_6/12 mL solvent. The yielded products were characterized by UV-Vis-NIR DRS to compare the intensity of LSPR peaks (**Figure 4.1**).

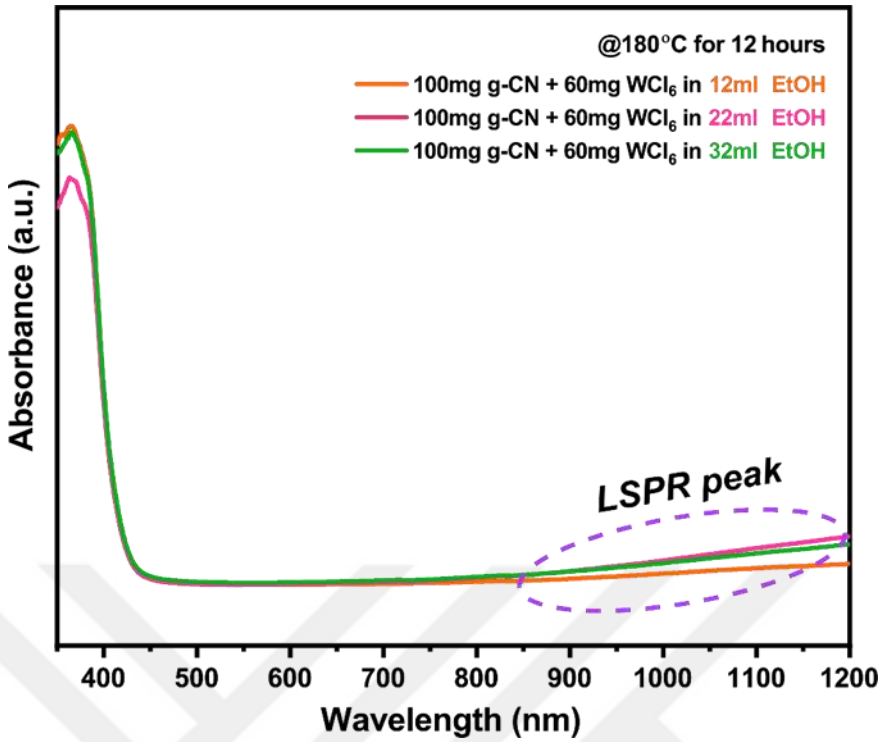

Figure 4.1: UV-Vis-NIR absorption of photocatalysts synthesized in 12 mL, 22 mL and 32 mL ethanol

According to spectra of heterojunctions that synthesized in different amount of EtOH, a more intense LSPR peak was formed synthesized in 22 mL EtOH. Therefore, 100 mg exfoliated g-CN and 60 mg WCl_6 in the presence of 22 mL ethanol was decided as starting amounts of precursors at the initial recipe to optimize synthesis parameters.

4.1.2 Optimum Temperature and Time

Studies in the literature about WO_{3-x} and g-CN/WO_{3-x} photocatalyst has generally used the same temperature, time and solvent in their synthesis procedure. Even though the most used temperature and time values are 180 °C and 12 hours, different temperatures and time parameters are present. Taking into account the literature, for 180°C; 12, 18 and 24 hours were chosen as reaction times while in the case of 160 °C, 18 and 24 hours were evaluated, and reactions took place keeping other parameters constant which are 100 mg exfoliated g-CN and 60 mg WCl_6 in 22 mL EtOH. Again, with the help of UV-Vis-NIR DRS, LSPR peaks of synthesized photocatalysts was observed (**Figure 4.2**). It was seen that 160 °C, which is independent from time, is not ideal temperature to

create oxygen vacancy within WO_3 structure. On the other hand, 180 °C is a proper temperature, and under these circumstances, reaction time has become an important parameter. However, 18 hours and 24 hours at 180°C show similar intensity in the LSPR range. Therefore, strategically, the optimum temperature and time was assigned as 180 °C and 18 hours because of shorter reaction time.

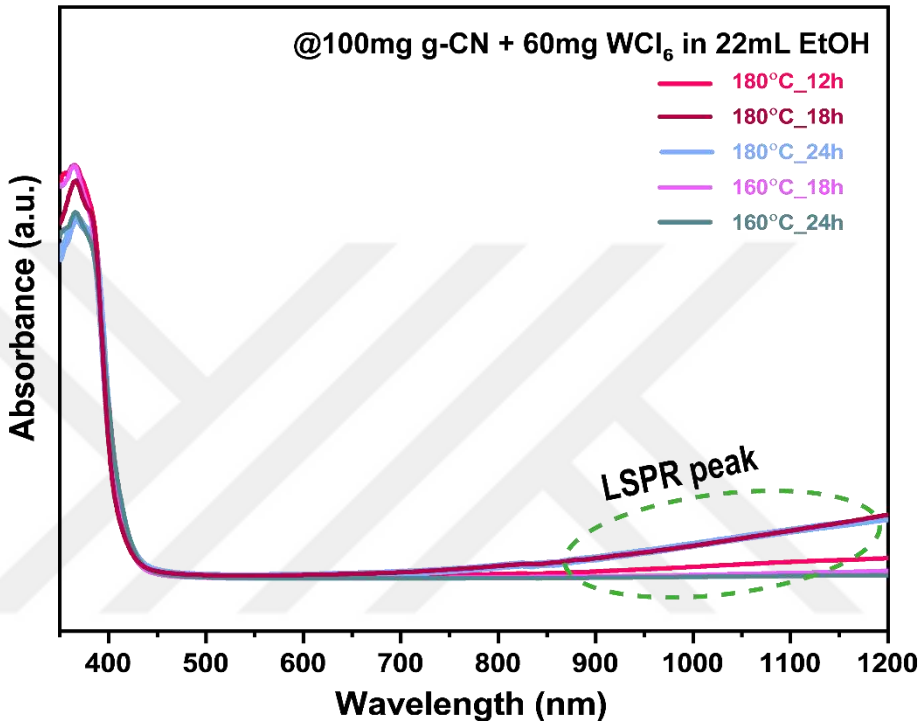

Figure 4.2: UV-Vis-NIR absorbance spectra of g-CN/WO_{3-x} photocatalysts that were synthesized at given temperatures and times

4.1.3 Optimum Solvent

A research conducted by Dickens et al. presented a reducing couple having E°< 0.34 V is enough for reduction of metal oxides by mild reductants under the solvothermal reaction conditions. At that point, alcohols and glycols are magnificent examples of mild reducing agents [125]. Consistent with this, generally ethanol, n-propanol and 2-propanol are preferred as a reaction medium for solvothermal synthesis of WO_{3-x}. Guo and colleagues proposed a reaction mechanism to form WO_{3-x} in the presence of alcohols. According to mechanism, condensation of two alcohol molecules where alkyl group is denoted by R produces ether derivatives and water **(Eq. 4.1)**. For an example, 2 mole of ethanol yields diethyl ether and water as a result of the condensation reaction **(Eq. 4.2)**.

In an autoclave, alcoholysis reaction occurs between WCl_6 and alcohol used as the solvent, and some amount of HCl was produced **(Eq. 4.3)**. In the last section of reaction, $(RCH_2O)_m$-WCl_6 complex utilize water molecule forming owing to etherification reaction in **Eq. 4.1** to create nonstoichiometric WO_{3-x} **(Eq. 4.4)** [126].

$$2\ RCH_2OH \rightarrow RCH_2OCH_2R + H_2O \quad \textbf{(4.1)}$$

$$2\ CH_3CH_2OH \rightarrow CH_3CH_2OCH_2CH_3 + H_2O \quad \textbf{(4.2)}$$

$$WCl_6 + RCH_2OH \rightarrow (RCH_2O)_m\text{-}WCl_n + mHCl \quad \textbf{(4.3)}$$

$$(RCH_2O)_m\text{-}WCl_n + H_2O \rightarrow WO_{3-x} + (RCH_2OH) + HCl \quad \textbf{(4.4)}$$

On the basis of explained reaction mechanism, 2-proponal (isopropanol) (ε= 19.92), ethanol (ε= 24.55), methanol (ε= 32.7), ethylene glycol (ε= 37) and water (ε= 81), were selected as a reaction medium by considering their dielectric constants since dielectric constant of solvent affect morphology and LSPR property of material.

LSPR property, morphology and activity of photocatalysts synthesized in those solvents were evaluated. In this regard, firstly, UV-DRS of these nanocatalysts were examined in **Figure 4.3**, and it could not detect any plasmonic peak in absorbance spectrum of photocatalyst that water and ethylene glycol were used as reaction medium despite limited increment in light absorption ability within visible region. Therefore, it was understood that not enough oxygen vacancy was created in WO_3 to form LSPR peak. In absorption spectra of photocatalysts where 2-propanol, ethanol and methanol were used as solvents, LSPR peak within the range of visible and NIR were present, and 2-propanol was possessed of more intense LSPR, followed by ethanol.

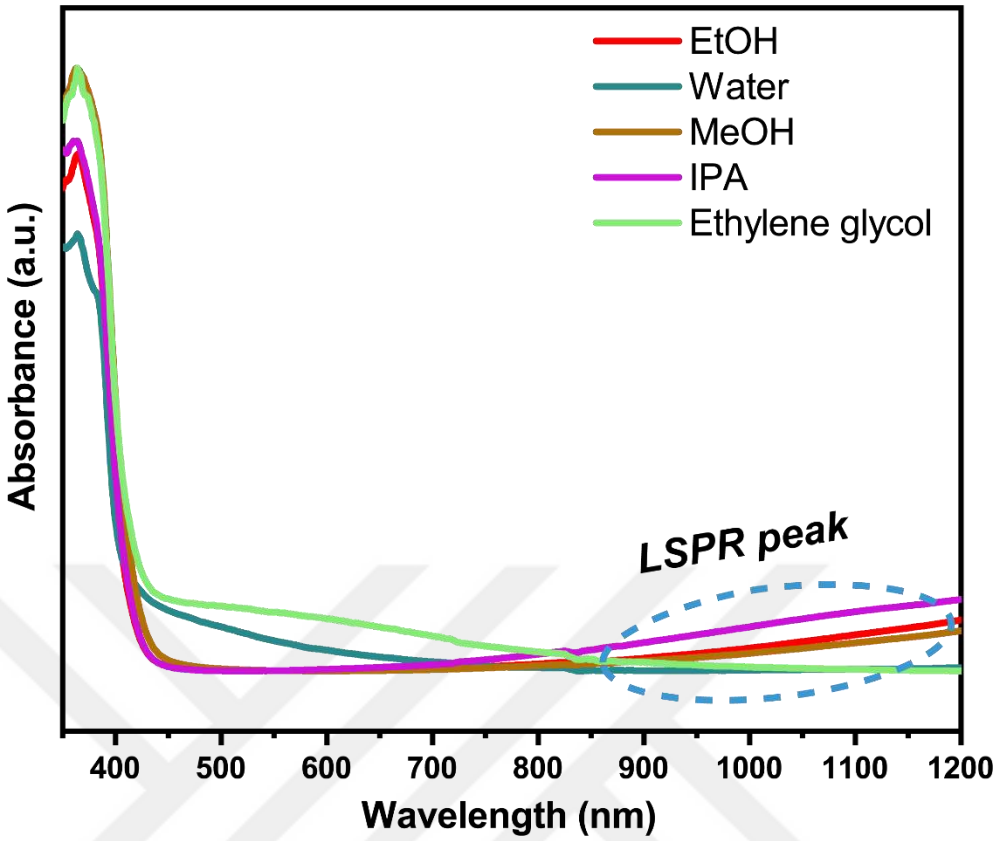

Figure 4.3: UV-Vis-NIR absorbance spectra of photocatalysts synthesized at given solvents

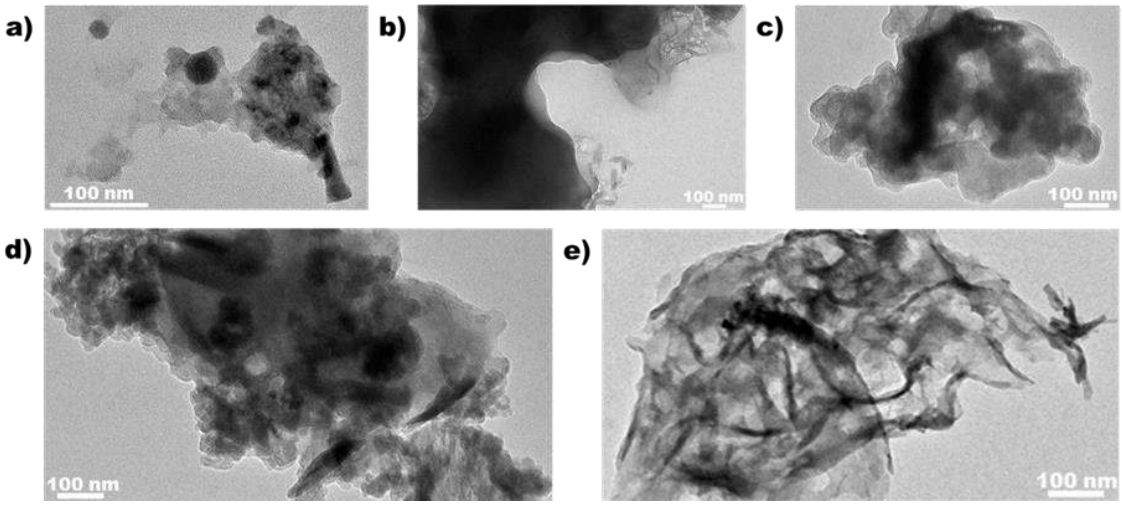

Figure 4.4: TEM images of g-CN/WO_{3-x} photocatalyst that were synthesized in **a)** water **b)** ethylene glycol **c)** ethanol **d)** isopropanol **e)** methanol

At the next step, morphology of as-synthesized photocatalysts in different solvents were analyzed with the help of TEM. Images in **Figure 4.4** pointed out that WO_{3-x}

morphology could be manipulated by changing solvent. **Figure 4.4.a** indicates a g-CN/WO_{3-x} photocatalysts synthesized in water. Owing to poor stability of g-CN in water at solvothermal reaction conditions which were 180°C for 18 hours and fast hydrolysis reaction of WCl_6 in water environment [127], non-uniform distribution of WO_3 as sediment on small g-CN nanosheets was observed. TEM image of g-CN/WO_{3-x} photocatalysts that were synthesized in ethylene glycol revealed that this heterojunction was extremely thick, and morphology of WO_3 was 2D nanosheets similar to g-CN (**Figure 4.4.b**). In case of ethanol (**Figure 4.4.c**), layered structure of g-CN and WO_{3-x} with nanosheets morphology could be seen. However, size of WO_{3-x} is smaller than that of g-CN nanosheets. Structure of g-CN/WO_{3-x} photocatalyst that was fabricated in 2-propanol comprises of thin and porous g-CN nanosheets along with spindle-like and sheet-like WO_{3-x} morphologies (**Figure 4.4.d**). When methanol was served as reaction medium, morphology of g-CN consists of thin nanosheets and worm-like structures while WO_{3-x} are located on g-CN as extremely thin rods (**Figure 4.4.e**). After UV-Vis-NIR DRS and TEM analysis of as-synthesized photocatalyst, to investigate synergism between LSPR property, morphology and activity, methyl orange (MO) degradation was chosen as a model reaction. In the presence of 5 ppm MO, with the aid of **Eq. 3.1** and **3.2**, degradation performance of photocatalyst and kinetic studies were studied in **Figure 4.4**. While only g-CN showed a degradation efficiency of 61.75% for 35 min (k=0.02921 min^{-1}), heterojunction g-CN/WO_{3-x} synthesized in ethylene glycol had too little increment as 62.3% with the rate constant k=0.02796 min^{-1}. In spite of higher LSPR intensity in ethanol (75.35% degradation, k=0.04234 min^{-1}) and isopropanol (77.55% degradation, k=0.04701 min^{-1}), the highest photodegradation efficiency was measured in g-CN/WO_{3-x} binary heterojunction that was synthesized in methanol as 97.1% with the rate constant k=0.09278 min^{-1}.

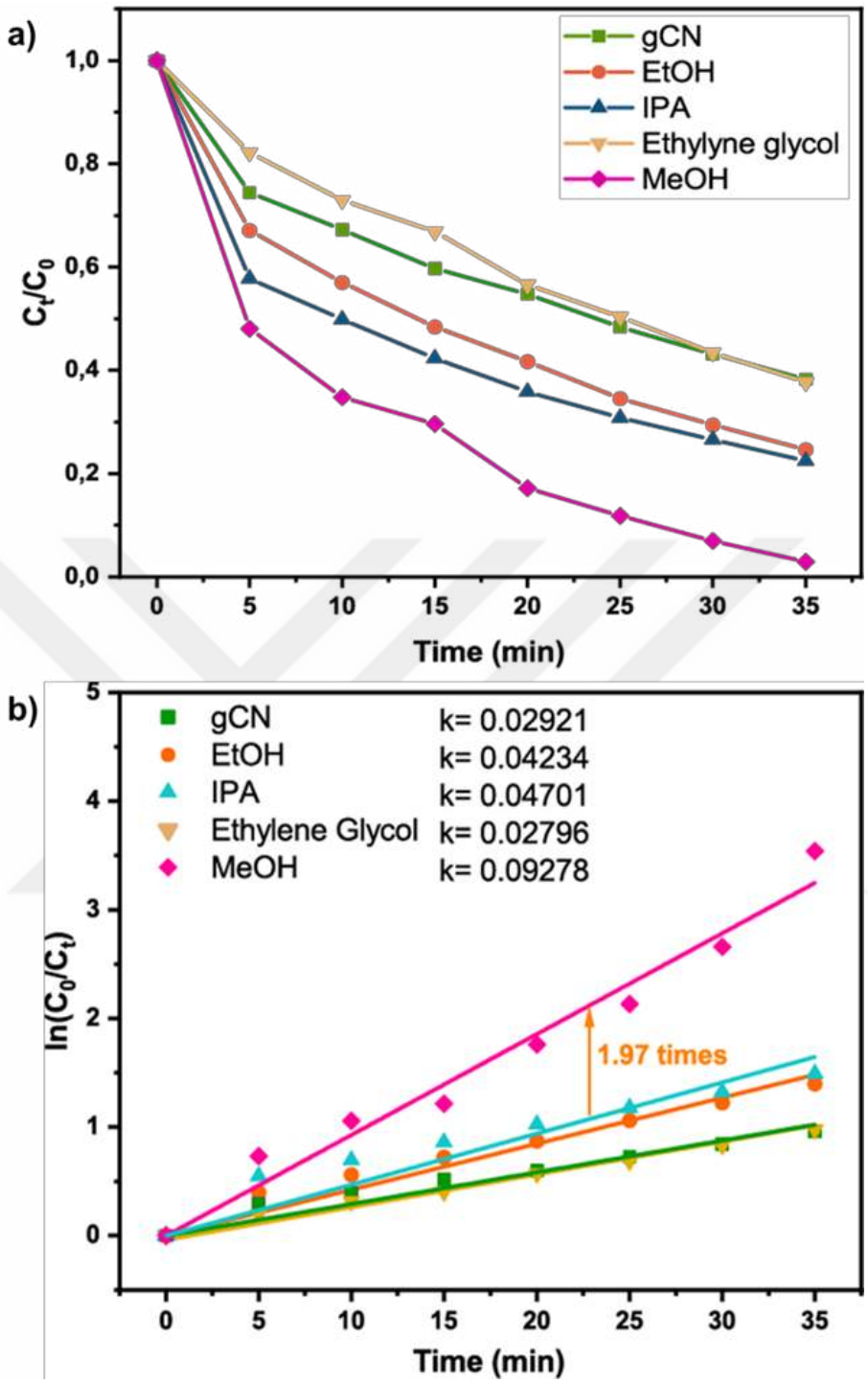

Figure 4.5: a) Degradation efficiencies and **b)** Reaction kinetics of photocatalysts synthesized in given solvents

In the light of these outcomes, methanol was selected as the optimum solvent for synthesis of g-CN/WO_{3-x} binary heterojunction. MeOH has the highest dielectric constant and the shortest carbon chain among the used alcohols in this study. As an additional information, dielectric constant of solvents is proportional to polarity of them, and

polarity affects the hydrolysis rate. In other words, higher polarity leads to higher hydrolysis rate [128]. Also, solvents with high polarity increases possibility of formation of anisotropic morphologies such as rod, wire and twist. Furthermore, Guo et al. presented that reducing power of primary alcohols becomes stronger with decreasing carbon chain, and in the case of secondary alcohols, reducing ability decreases due to position of -OH group [126]. These outputs shed light on why methanol is the best solvent. Also, result displayed that methanol formed to WO_{3-x} with rod-like morphology on layered g-CN, having the highest activity notwithstanding lower LSPR peak intensity of this photocatalyst. The main rationale of this issue could be expressed by near-field enhancement phenomena (NFE), which can be described as ratio of localized electric field with activation of surface plasmons to incident electric field [129]. In the presence of plasmonic materials, NFE amplify photocatalytic activity since it serves as a source to excite other resonant phenomena such as excitations and phonons to enhance signals or accelerate hot carrier generation [52, 130]. Increment in NFE is strongly correlated with shape anisotropy. In the current literature, nanorods produces extremely stronger NFE which is 400 times higher than particle form by means of high asymmetry with raising aspect ratio. In addition, LSPR is dependent on morphology because it was proven that LSPR peak shifts to higher wavelengths with increasing aspect ratio [131].

In summary, there is a relation between LSPR, photocatalytic activity and structure. Binary g-CN/WO_{3-x} heterojunctions that were synthesized in MeOH forms rod-like WO_{3-x}, and this photocatalyst exhibited the highest MO degradation performance under visible light irradiation. In spite of its lower LSPR peak intensity, its anisotropic shape makes possible production of stronger electric field around material that accelerates reaction in different ways.

4.1.4 Optimum Concentration

Fundamental purpose at this step is essentially optimization of WCl_6 amount in the synthesis route of g-CN/WO_{3-x} heterojunction. However, a published study proved that concentration of WCl_6 to solvent amount has a notable impact on WO_{3-x} LSPR property, and as stated before, optimal concentration is 5 mg/mL [124]. In the light of this outcome, solvent amount also needs to be adjusted to optimize amount of WCl_6 for finding the best

binary g-CN/WO_{3-x} heterojunction by conserving ratio of 5 mg WCl_6 in 1 mL solvent. While keeping the amount of exfoliated g-CN, reaction temperature and time as constant at 100 mg, 180°C and18 hours, respectively, WCl_6 and methanol amounts were changed. To begin with, g-CN/WO_{3-x} heterojunction photocatalysts were synthesized using solvothermal method by adding 70 mg WCl_6/24 mL MeOH, 80 mg WCl_6/26mL MeOH, 90 mg WCl_6/28 mL MeOH and 100 mg WCl_6/30 mL MeOH. Concentration operations were calculated based on 10 ml MeOH for 100 mg g-CN, and remaining MeOH is for WCl_6 by keeping 5 mg/mL constant. To investigate photocatalytic performance of the synthesized material, MO degradation was used as model reaction again. **Figure 4.6a** demonstrated that g-CN/WO_{3-x} photocatalyst yielded by the 80 mg WCl_6/26 mL MeOH combination degraded 5 ppm MO with 98% in 25 minutes. Degradation performance of other photocatalysts was 91% for 70 mg WCl_6/24 mL MeOH, 97% for 90 mg WCl_6/28 mL MeOH and 91.2% for 100 mg WCl_6/30 mL MeOH. Indeed, photocatalyst 90 mg WCl_6/28 mL MeOH exhibited satisfactory performance but 80 mg WCl_6/26 mL MeOH was chosen as optimum one since less amount of WCl_6 is better in terms of cost efficiency and sustainability. Furthermore, additional synthesis with 80 mg WCl_6/22 mL MeOH was done to extra find out effect of MeOH amount. MO photodegradation performance of this heterojunction was limited to 85%. Also, photoactivity of the heterojunction, namely 60 mg WCl_6/22 mL MeOH was found as 88% in MO degradation. By keeping MeOH amount constant as 22 mL, when amount of WCl_6 was augmented from 60 mg to 80 mg, MO degradation efficiency decreases to a degree. On the one hand, if MeOH amount was adjusted as 26 mL for 80 mg WCl_6, heterojunction exhibited outstanding photocatalytic activity as 98% within 25 min. These results clearly unveiled significance of concentration.

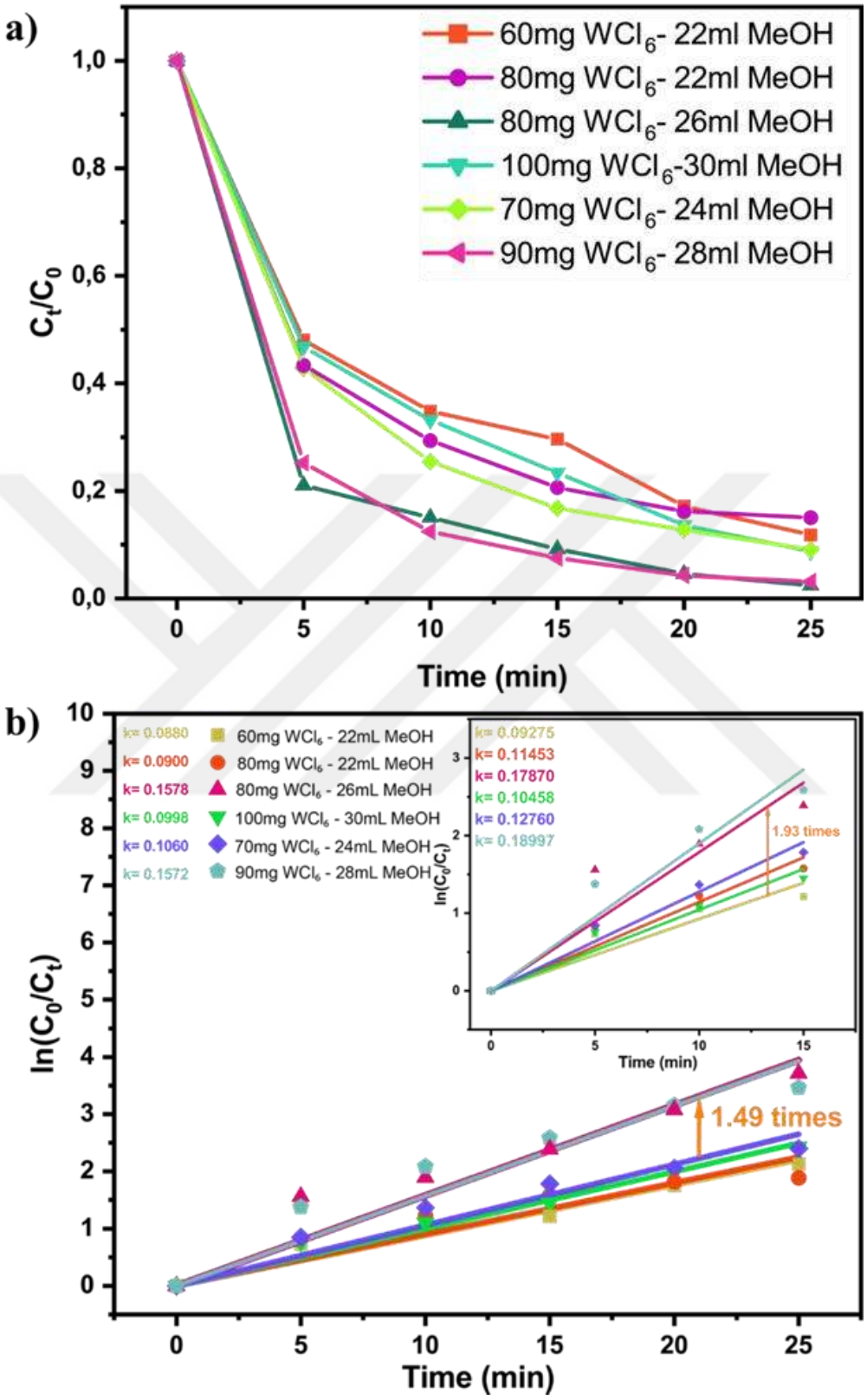

Figure 4.6: a) Degradation efficiencies and **b)** Reaction kinetics of photocatalysts synthesized at varied W precursor and methanol amounts (The inset figure demonstrates reaction kinetics for 15 min.

In **Figure 4.6b**, rate constants of the MO degradation reactions conducted in aqueous medium was calculated by using the formula of first-order reaction (**Eq. 3.2**). As expected, the degradation reactions in which g-CN/WO_{3-x} photocatalysts synthesized by using 80 mg WCl_6/26 mL MeOH and 90 mg WCl_6/28 mL MeOH provided the highest rate constants k=0.1578 and k=0.1572 in the same order. However, g-CN/WO_{3-x} heterojunction in 80 mg/26 mL case degrades approximately 81% of MO within initial 5 minutes so for remaining time interval, degradation becomes more difficult due to low concentration of MO. As a result, with increasing reaction time, k values become smaller. At this point at 15 minute, another reaction kinetic graph was plotted which is inset in **Figure 4.6b**, and it was understood that reaction rates of photocatalysts performing the highest activity increases to k= 0.1870 and 0.18997 min^{-1}, respectively, However, it should be noticed that point belonging to extremely high degradation performance of 80 mg/26 mL case at the 5 minutes exhibits undeniable deviation from line, and it can give rise to calculation of lower rate constant.

4.2 Materials Characterization

Raman spectroscopy was applied to the synthesized WO_3 and WO_{3-x} semiconductors to show successful synthesis of oxygen deficient structure since Raman is sensitive technique to separate stoichiometric and nonstoichiometric tungsten oxides each other [132, 133]. In a typical Raman spectrum, as peak with the highest frequency is attributed to the stretching of the shortest bond and regularity of structure [134], the range within 400 and 900 cm^{-1}, containing the shortest bond were analyzed for WO_3 and WO_{3-x} materials.

Figure 4.7 depicted that synthesis of WO_{3-x} containing oxygen vacancy was accomplished. Nevertheless, nonstoichiometric tungsten oxides are extremely unstable at high temperatures, and on account of local heating of Raman focused laser beam, WO_{3-x} encountered partial phase transition of WO_3 during analysis. Therefore, an accurate amount of oxygen vacancy could not be estimated in this study. In Raman spectrum of WO_3, peaks at 716.4 cm^{-1} and 806.2 cm^{-1} pertain to stretching mode of W-O-W bonds. Moreover, the first peak points out stretching of longer W-O-W bonds while the second bond indicates stretching of the shortest bond. In case of WO_{3-x}, these two peaks exhibited broader characteristic [133]. The peak at higher frequency are wider than that of WO_3, and it causes tailing towards higher energies. This means that WO_{3-x} is more disordered

compared to WO_3, and it contains various W-O-W bonds, having shorter lengths [134]. In addition, the former peak was extremely broader and asymmetric, and it showed Raman shifting to lower wavenumbers, designating longer bonds. Since oxygen vacancy on the WO_{3-x} structure causes different bond lengths between W and O, broadening of peaks make sense. Furthermore, asymmetric broadening peak is assigned to lower crystallinity and improper coordination of surface atoms in the crystal lattice [135].

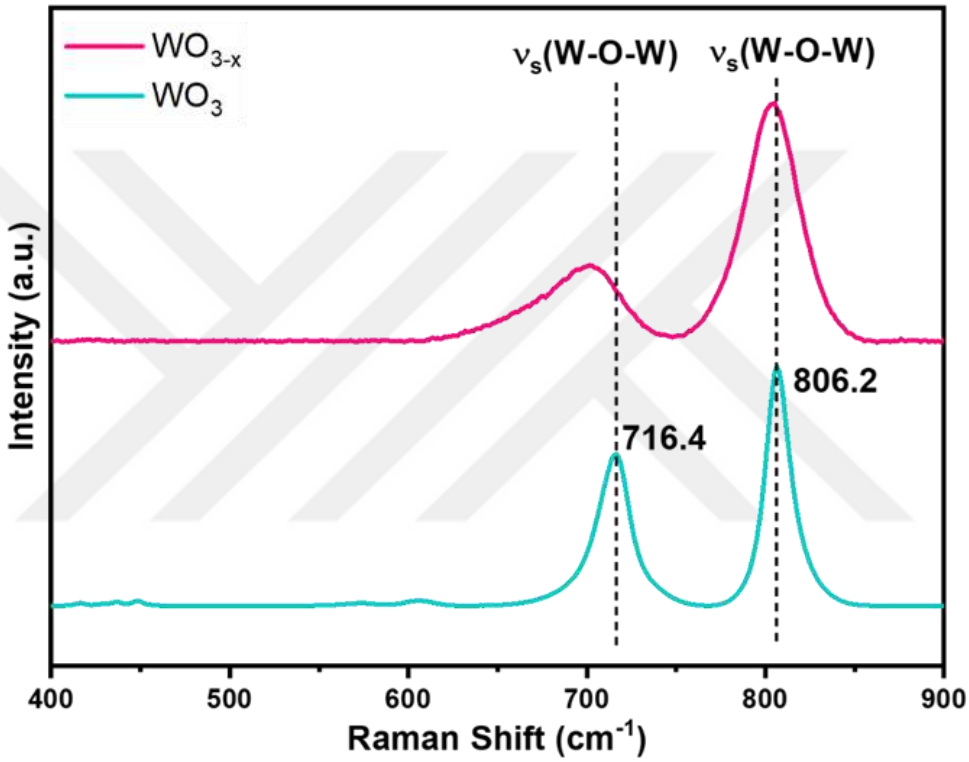

Figure 4.7: Raman spectra of WO_3 and WO_{3-x}

PXRD analysis was employed to pristine materials and heterojunction of them for determination of their crystal structure and identification of present phases (**Figure 4.8**). In the PXRD pattern of g-CN, two peaks were disclosed at 2θ = 12.8° and 2θ = 27.06° attributed to (100) and (002) diffraction planes of g-CN, respectively (JCPDS No. 87-1526). The former peak appeared owing to intralayer distance between repeating motifs in a monolayer, and calculated d-spacing (d = 0.691 nm) was close to theoretic d-spacing value of tri-s-triazine (d= 0.681 nm) [136]. Moreover, the latter peak with high intensity demonstrated d-spacing between two g-CN layers [137]. Another semiconductor in the heterojunction was WO_{3-x}. Peaks at 2θ = 22.76° , 26.71°, 34.6°, 46.97°, 49.8° and 55.8°

that belongs to (010), (203), (114), (020), (315) and (523) planes in PXRD pattern of as-synthesized WO_{3-x} revealed that WO_{3-x} had monoclinic crystal structure, and it did not contain any impurity (JCPDS No. 71-2450) [138]. In the case of the PXRD patterns of g-CN/WO_{3-x} binary heterojunction, the peak of (100) plane at $2\theta = 12.8°$ attributing to the intralayers in g-CN becomes sharper and more intense, indicating increment in crystallinity of g-CN [139]. Peak of (200) diffraction plane considerably shift to higher degree, resulting in lower d-spacing. This occurrence was ascribed to the high electronegativity of oxygen atoms in WO_{3-x} structure, which resulted in a reduction of the interplanar space among the heptazine motifs [140]. On the one hand, characteristic peaks of WO_{3-x}, having remarkable intensity had been detected in XRD profile of g-CN/WO_{3-x}. Especially (114) plane of WO_{3-x} became more intense and sharper for the binary heterojunctions, suggesting more crystalline structure and larger crystallite size. Furthermore, location of WO_{3-x} peaks shifted to higher degrees associated to successful interaction of parent semiconductors. One last word is some WO_{3-x} peaks disappeared in PXRD pattern of binary heterojunction since the integration surface of WO_{3-x} over g-CN could inhibit diffraction on some planes.

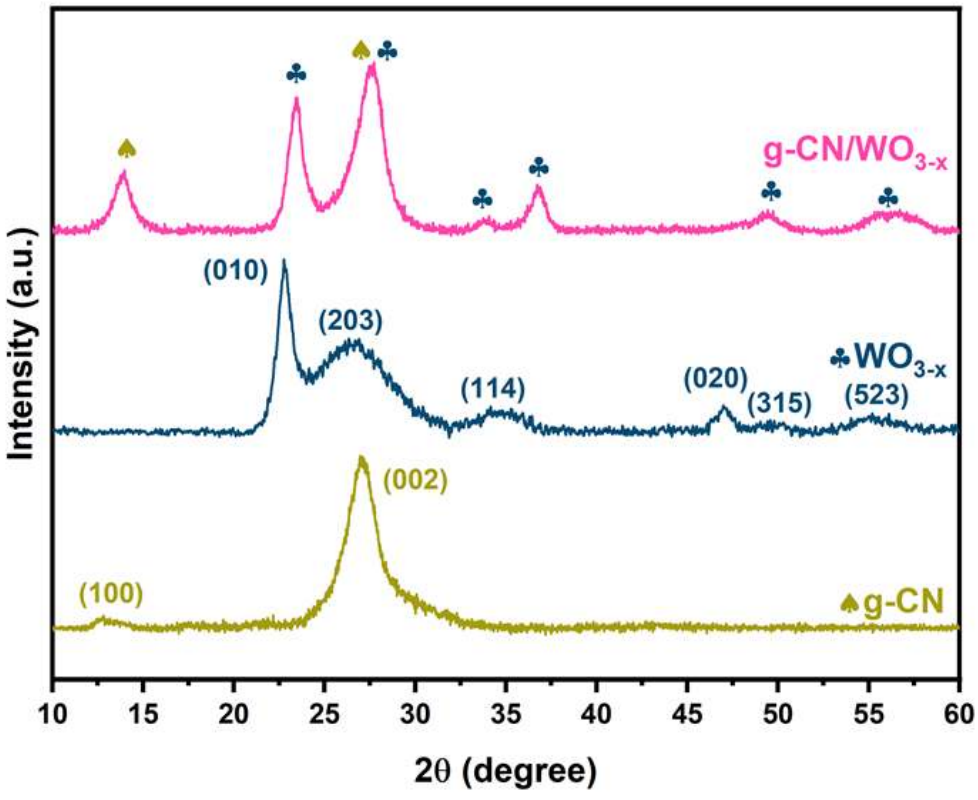

Figure 4.8: PXRD patterns of g-CN, WO_{3-x} and g-CN/WO_{3-x}

SEM analysis was conducted to investigate morphologies of pristine WO_{3-x} and g-CN/WO_{3-x} photocatalysts. In **Figure 4.9a,** at low magnification, morphology of WO_{3-x} resembles to nano-dandelion formed by thin rods. In **Figure 4.9b**, it was seen that nanorod and its bundle-like structure was main blocks forming WO_{3-x} morphology. Moreover, average size of WO_{3-x} nanorods was roughly measured as length of 98.2 nm with diameter of 14.5 nm. SEM images of g-CN/WO_{3-x} heterojunction displayed that WO_{3-x} was distributed onto g- CN, and apart from bundle-like form of WO_{3-x}, ultra-thin nanorods were present on g-CN at **Figure 4.9c-d**. Also, porous and thin structure of layered g-CN was observed.

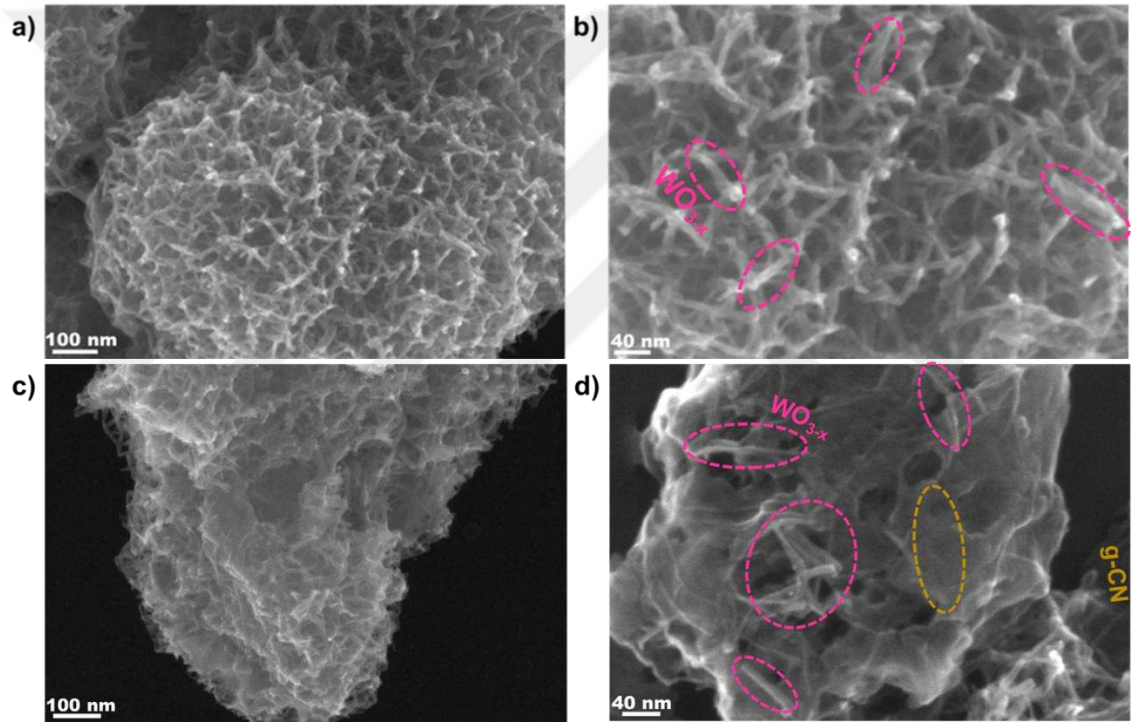

Figure 4.9: SEM image of WO_{3-x} at **a)** low magnification and **b)** high magnification of g-CN/WO_{3-x} at **c)** low magnification **d)** high magnification

TEM and HRTEM techniques were employed for further clarification of morphological features of as-prepared photocatalysts. **Figure 4.10a-b** manifested that g-CN consists of not only expected 2D nanosheets but also worm-like shaped materials are present, which might be attributed to curling of thin nanosheets along different directions. However, it should be noticed that thin and layered morphology of g-CN is evident. The TEM images WO_{3-x} shows one-dimensional (1D) rod-like morphology with almost homogeneous length distribution in terms of diameter (**Figure 10c-d**). However, there

are some rods gathered and formed bundle-like morphology. In the case of TEM images of g-CN/WO_{3-x} photocatalyst depicted in **Figure 4.10e-f**, it is clearly observable that 1D WO_{3-x} rods grew on thin layered g-CN nanosheets. However, coexistence of both worm-like g-CN and rod/bundle-like WO_{3-x} on g-CN made it difficult to identify at low magnification TEM image. At high magnification TEM images (**Figure 4.10g)**, it can be concluded that rod-like WO_{3-x} structures possess sharp and distinct corners and borders whereas worm-like structures (g-CN) have rounded-corners and unclear borders. In **Figure 4.10g**, HRTEM image of binary heterojunction demonstrated rod-like WO_{3-x} and extremely thin g-CN nanosheets apparently and thus this image was used for elemental mapping displayed in **Figure 4.12**. Lattice fringes of g-CN and WO_{3-x} in the binary heterojunction was calculated by using a HRTEM image in **Figure 4.10e**. d-spacing of g-CN and WO_{3-x} was calculated as 0.326 nm and 0.333 nm, respectively, matching with the (002) plane of g-CN and (203) plane of WO_{3-x} determined from XRD patterns.

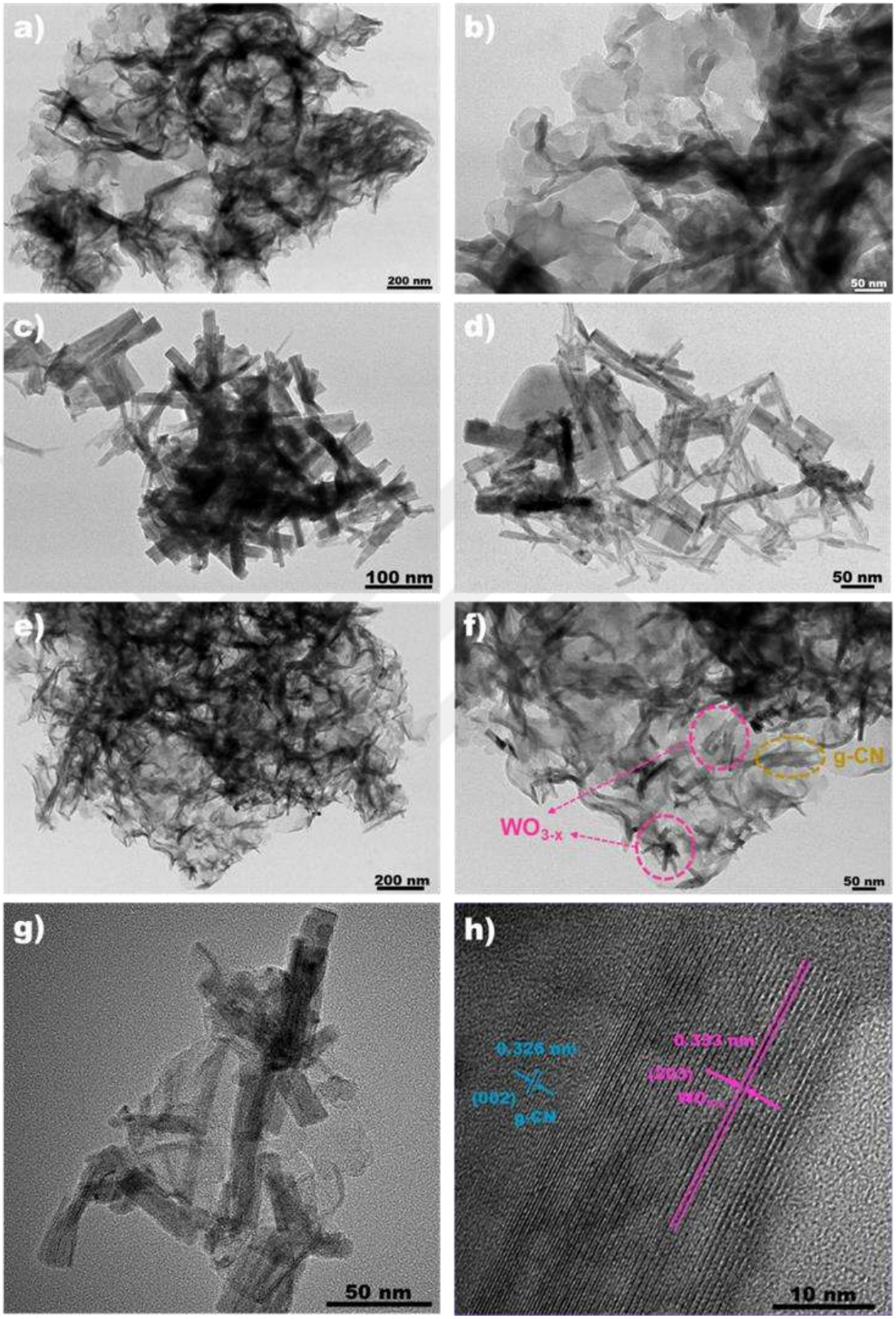

Figure 4.10: TEM images of **a-b)** g-CN **c-d)** WO_{3-x} **e-f)** g-CN/WO_{3-x} and HRTEM images of **g-h)** g-CN/WO_{3-x} at different magnifications

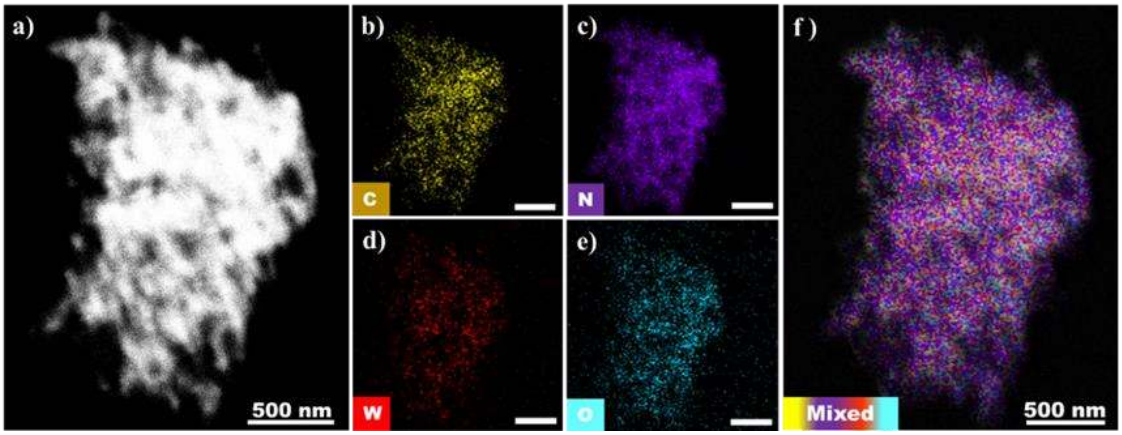

Figure 4.11: a) HAADF-STEM image and **b-f)** elemental mapping of g-CN/WO_{3-x} heterojunction at low magnification

Elemental distribution of g-CN/WO_{3-x} photocatalyst was studied through TEM-EDX analysis at low magnification (**Figure 4.11**). The elemental mapping images proved that all expected elements formed the binary heterojunction (C, N, W and O) are present, and their distribution throughout the structure is almost homogenous. However, low magnification images could not give any information about elemental content of rod-like morphologies that can be seen in TEM images of g-CN/WO_{3-x}. Therefore, another EDX-elemental mapping analysis was conducted at higher magnification. In **Figure 4.12**, it was showed clearly that W and O forms elemental composition of rod-like morphologies, and g-CN acts as support for WO_{3-x}.

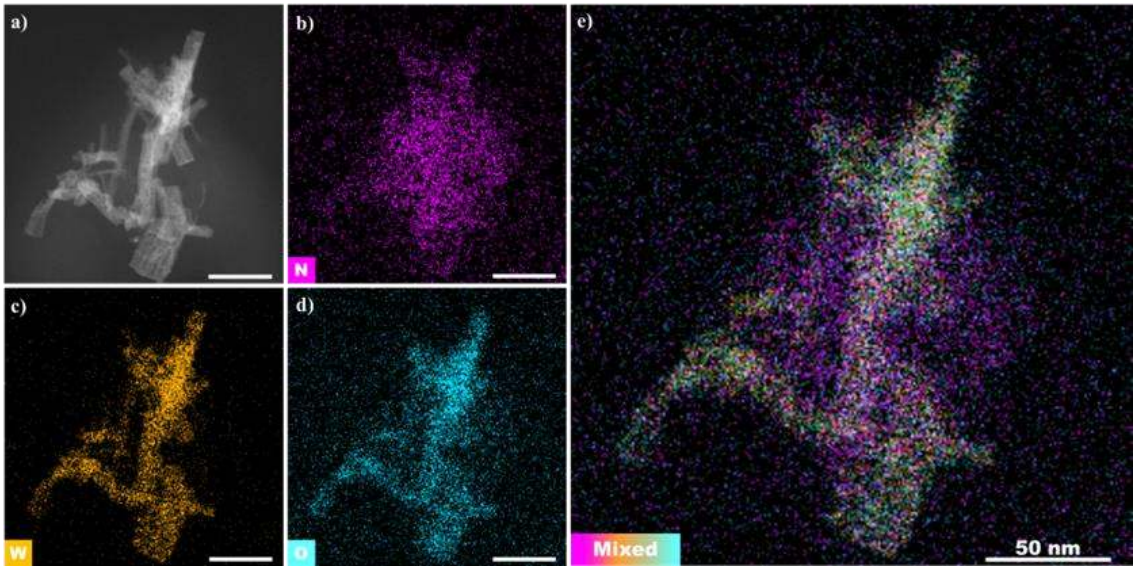

Figure 4.12: a) HAADF-STEM image and **b-e)** elemental mapping of g-CN/WO_{3-x} heterojunction at low magnification

XPS analysis was employed to assign oxidation states of elements and change in chemical environment with construction of binary heterojunction. In this regard, detection of C, N, W and O elements in XPS analysis of g-CN/WO_{3-x} photocatalyst was additional proof for successful synthesis of heterojunction. High resolution XPS spectra of C 1s and N 1s regions for pristine g-CN and g-CN/WO_{3-x} binary heterojunctions along with W 4f and O 1s regions of WO_{3-x} and g-CN/WO_{3-x} were investigated to clarify interaction between g-CN and WO_{3-x} and provide clear insights about the formation of binary heterojunctions (**Figure 4.13**). In **Figure 4.13.a**, C 1s spectrum of g-CN represented three characteristic peaks which were positioned at 284.5 eV, 286.4 eV and 288 eV, respectively. The first peak at 284.5 indicated to C-C/C=C species coming from used carbon tape for XPS analysis and used as refence peak. Before interpretation of results, all peaks in XPS spectra was calibrated with respect to this adventitious C-C/C=C peak. Peak at binding energy of 286.4 eV was attributed to C coordinated to terminal N atoms denoted as C-$(N)_3$. A final peak at 288 eV was assigned to sp^2-hybridized C atom in the aromatic ring (N-C=N) [141, 142]. Since structure of g-CN was examined, number of C atoms in N=C-N was higher than C atoms in C-$(N)_3$. Therefore, binding energy shifting of N=C-N peak in case of g-CN/WO_{3-x} was more critical to understand effect of heterojunction formation on chemical environment. When C 1s spectrum of binary heterojunction was compared with that of g-CN, it was understood that peak at 288 eV shifts to higher binding energies, pointing out decrease in electron density around C atom. High resolution N 1s XPS spectrum of g-CN was deconvoluted into three peaks at 398.5 eV, 400.2 eV and 401.1 eV in order which were ascribed to sp^2-hybridized N atoms in triazine units (C-N=C), bridging sp^3-hybridized N in N-C_3 and N in terminal amino groups [143]. In the case of N 1s spectrum of g-CN/WO_{3-x} heterojunction, peak at the highest binding energy shift to almost 0.02 eV positive whereas the other two peaks shift to lower binding energies in comparison to N 1s of g-CN. Similar to C case, g-CN structure contains more sp^2-hybridized N, and limiting shifting of this peak indicates electron loss around N atoms in C-N=C units (**Figure 4.13b**). High resolution W 4f XPS spectra of WO_{3-x} and g-CN/WO_{3-x} were depicted in **Figure 4.13c** for comparison. Characteristic two-coupled doublet in W 4f spectrum of WO_{3-x} originated from W with different oxidation states. Intense peaks at binding energy of 37.7 eV and 35.5 eV was associated to W^{+6} $4f_{5/2}$ and W^{+6} $4f_{7/2}$, respectively whereas, the less intense two peaks located at 36.4 eV and 34.2 eV indicated W^{+5} $4f_{5/2}$ and W^{+5} $4f_{7/2}$ in the same order [76].

At this point, detection of W^{+5} was notable because oxygen deficiency forms owing to existence of W^{+5} in structure. Comparison of this spectrum with W 4f spectrum of binary heterojunction demonstrated a strong shifting of all peaks to lower binding energies. It means that electron density on W environment increases. The high resolution O 1s XPS spectrum of WO_{3-x} was deconvoluted to two peaks. The peak at 530.3 eV was ascribed to lattice oxygen in WO_{3-x} structure forming W-O bond while the peak at higher binding energy indicating to oxygen vacancies. In reality, since oxygen vacancy is a vacant point which is not containing oxygen, there is no signal coming from oxygen vacancy. However, signal coming from lattice oxygens connected to W^{5+} produces peak belonging to O. With construction of g-CN/WO_{3-x} heterojunction, these peaks shifted to lower binding energies in high resolution O 1s XPS spectrum. This can be explained by enhancement of electron density around oxygen atoms. Moreover, an additional peak belonging to chemisorbed O was appeared due to attachment of –OH on photocatalyst surface (**Figure 4.13d**) [74]. When all results obtained from XPS analysis were evaluated together, it was concluded that there is a strong interfacial interaction between g-CN and WO_{3-x}, and electron flow occurs from g-CN to WO_{3-x} in binary heterojunction.

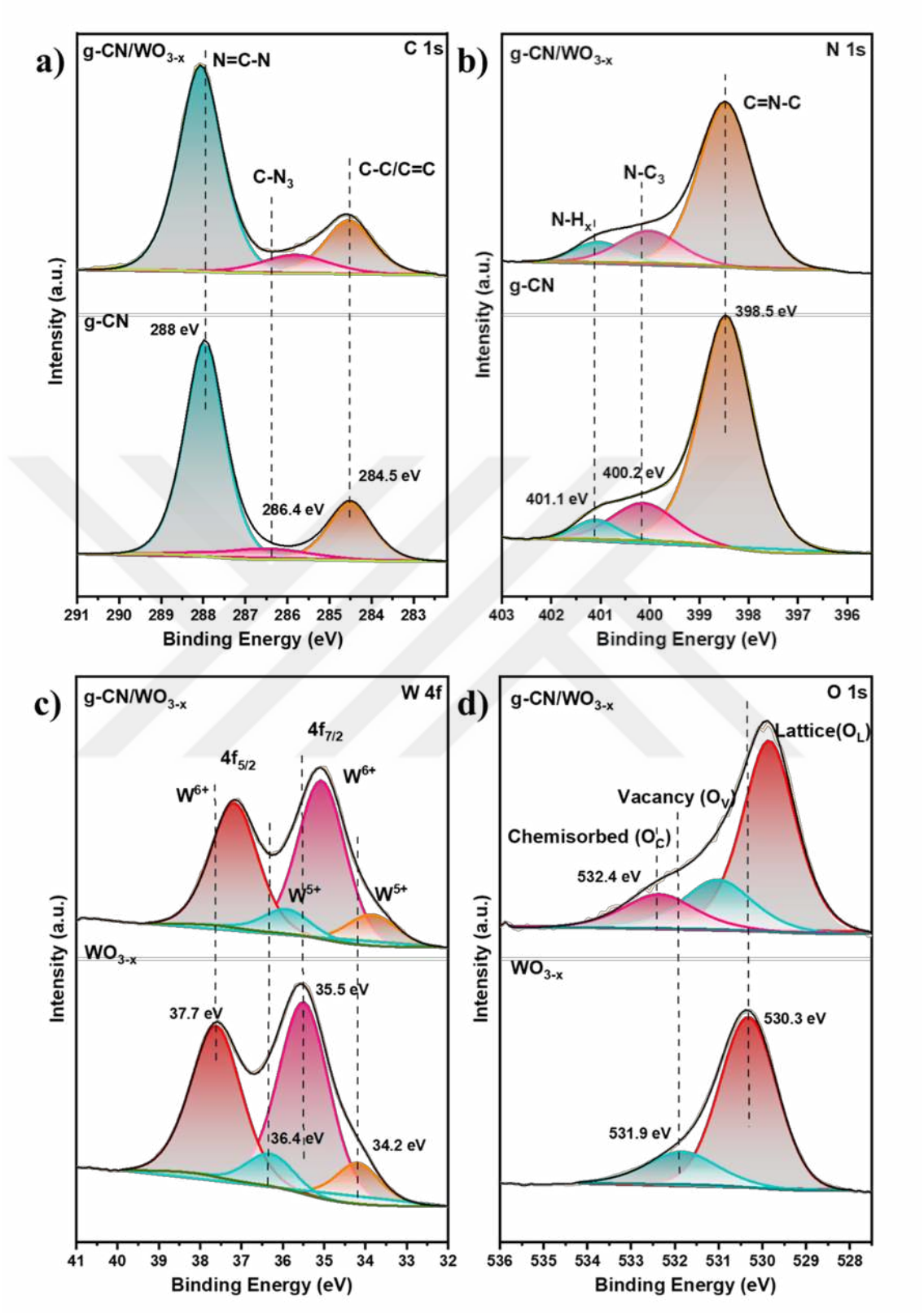

Figure 4.13: High resolution XPS **a)** C 1s **b)** N 1s **c)** W 4f **d)** O 1s spectra of g-CN, WO_{3-x}, g-CN/WO_{3-x}

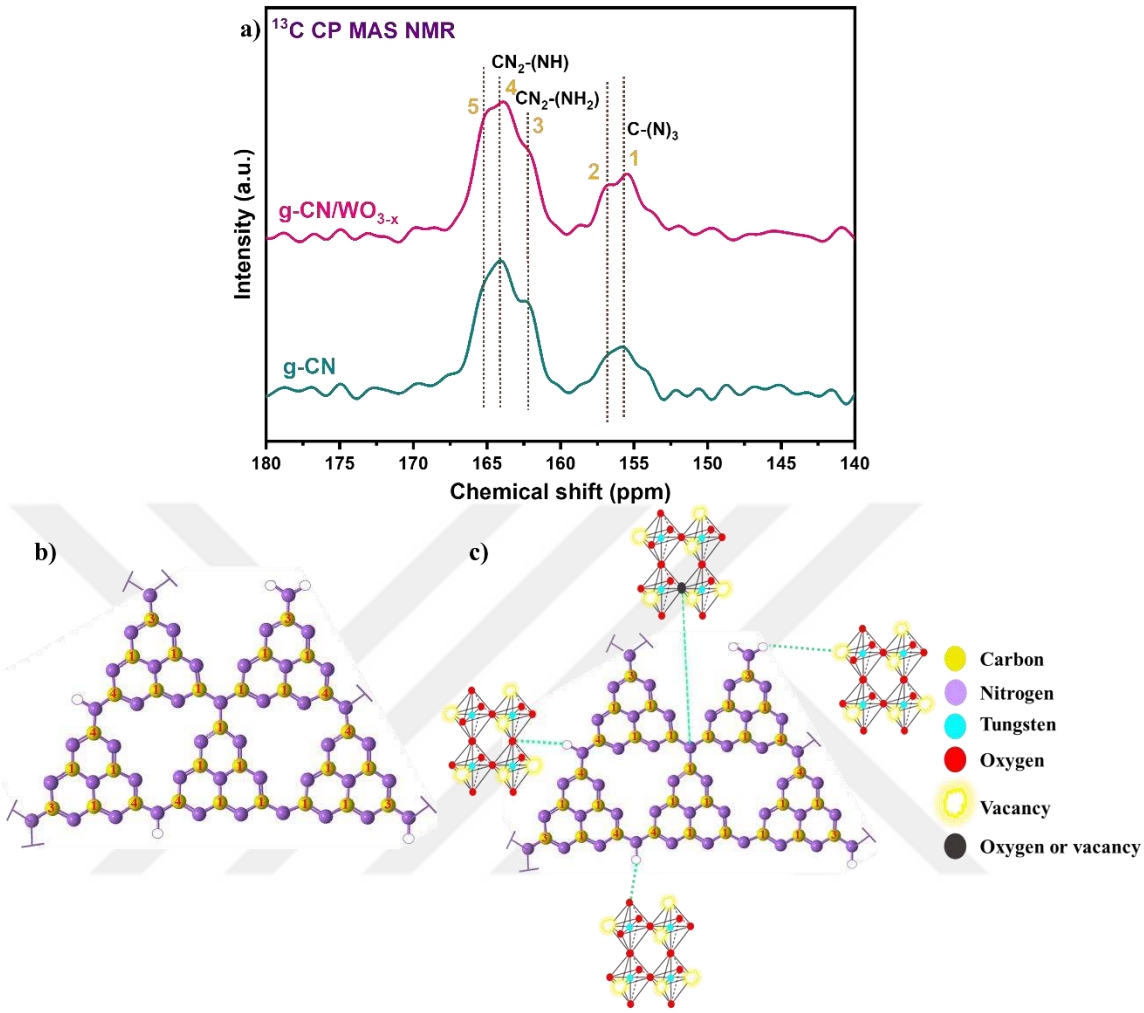

Figure 4.14: a) ^{13}C CP MAS NMR of g-CN and g-CN/WO_{3-x}, and schematic representation of components and their interactions at **b)** g-CN and **c)** WO_{3-x}

To further confirm XPS results, ssNMR of ^{13}C was examined for g-CN and g-CN/WO_{3-x} heterojunction photocatalyst (**Figure 4.14**). Cross polarization (CP) is a ssNMR technique to increase the weak signal of ^{13}C nuclei through polarization transfer from abundant ^{1}H nuclei [144]. For this purpose, H atoms close to C's in the structure is extremely important, and these H atoms generally take position at the edge of material and around defect. Therefore, the observed ^{13}C signals belong to C-containing groups at the edge or defective parts of material [145]. When **Figure 4.14a** was evaluated, the characteristic peaks of g-CN was detected at 155.7 ppm, 162. 24 ppm and 164.19 ppm. Peak at lower ppm was ascribed to CN_3 units in poly(tri-s-triazine) structure, peaks at 162.24 and 164.19 ppm were assigned to CN_2-NH_2 and CN_2-NH labeled as C3 and C4,

respectively [146]. In **Figure 4.14b**, C atoms related to C1, C3, C4 are marked on the schematic structure of g-CN. After the construction of g-CN/WO_{3-x} heterojunction photocatalyst, these distinctive peaks broadened and new shoulder peaks (C2 and C5) at 156.8 and 165.16 ppm towards higher frequency appeared. The addition of WO_{3-x} to g-CN clearly caused a disorder in its structure, thus alteration in the chemical environment of g-CN's repeating motifs. In the parts where there is an interaction between WO_{3-x} and heptazine ring, electron flow from g-CN to WO_{3-x} deshielded C atoms in CN_2-NH_x (x= 1 or 2) and CN_3 due to interaction of O atoms in WO_{3-x} (**Figure 4.14c**). Besides, the augmentation in C2 and C5 may occur owing to close location WO_{3-x} at CN_2-NH_x (x= 1 or 2) forming H bonds through both O and vacant sites, consistent with XPS results. On the other hand, the part where the electron density around C has increased because of intercalation of WO_{3-x} between two g-CN layers. Since the existence of O atoms shortened the distance of g-CN layers as observed in XRD, the heptazine units free from WO_{3-x} share π-π interaction among them thus, the increasing the electron density in the aromatic rings.

To further enlighten the optical behaviors of photocatalysts, several spectroscopic methods were implemented. Optical absorbance properties were probed by UV-Vis-NIR Diffuse Reflectance Spectroscopy (DRS). After measurement, reflectance data were transformed to absorption through Kubelka-Munk function, and absorption spectra were plotted. In **Figure 4.15a**, it was understood that g-CN, having absorption edge at around 444 nm, exhibited extremely limited light absorption ability in visible and near-infrared regions. Although WO_{3-x} possessed lower band absorption edge with approximately 419 nm, it could harvest light within visible and near-infrared regions thanks to presence of LSPR peak as it is aforementioned [8,50]. After construction of heterojunction with g-CN and WO_{3-x}, band edge of composite has shifted to 437 nm. On the other hand, the incorporation of WO_{3-x} to g-CN enabled remarkable absorption in the range of visible and near-infrared lights. In this way, g-CN/WO_{3-x} photocatalyst could be activated by any photon in UV, visible and NIR regions of the solar spectrum without using metallic nanoparticles. Moreover, the Tauc Plot was used to calculate corresponding bandgaps of g-CN and WO_{3-x} (*vide infra*) (**Figure 4.21**).

Photoluminescence (PL) spectroscopy was utilized to investigate and compare photogenerated charge recombination and separation characteristics of photocatalysts **(Figure 4.15b)**. For all analyzed semiconductors, 350 nm was used as the excitation

wavelength. In the PL spectra, contrary to WO_{3-x}, g-CN displayed a strong luminescence peak at around 452 nm. It was a proof that g-CN suffers from high electron-hole recombination. In the case of binary heterojunction, strong PL intensity of g-CN was quenched by 70%. This weak luminescence peak indicated an efficient suppression of charge recombination and successful charge separation.

Time-resolved photoluminescence spectroscopy (TRPL) was performed to explore photocatalysts' charge carrier separation and transfer kinetics in more details [147]. 377 nm laser served to excite target materials, and nanosecond timescale was used to record the lifetimes. Biexponential decay model containing fast (τ_1), and slow (τ_2) decay constituents were used for fitting of TRPL spectra. τ_1 and τ_2 are terms derived from non-radiative decay owing to recombination of photogenerated carriers with defects in the structure and radiative decays due to e^--h^+ recombination respectively, and τ_{avg} was determined by **Eq 3.9** [50, 148]. **Figure 4.15c** showed that τ_{avg} of g-CN diminishes from 6.96 ns to 5.95 ns with introduction of WO_{3-x} into structure, offering strong interaction at the interface that providing faster and easier charge migration at heterojunction [149, 150].

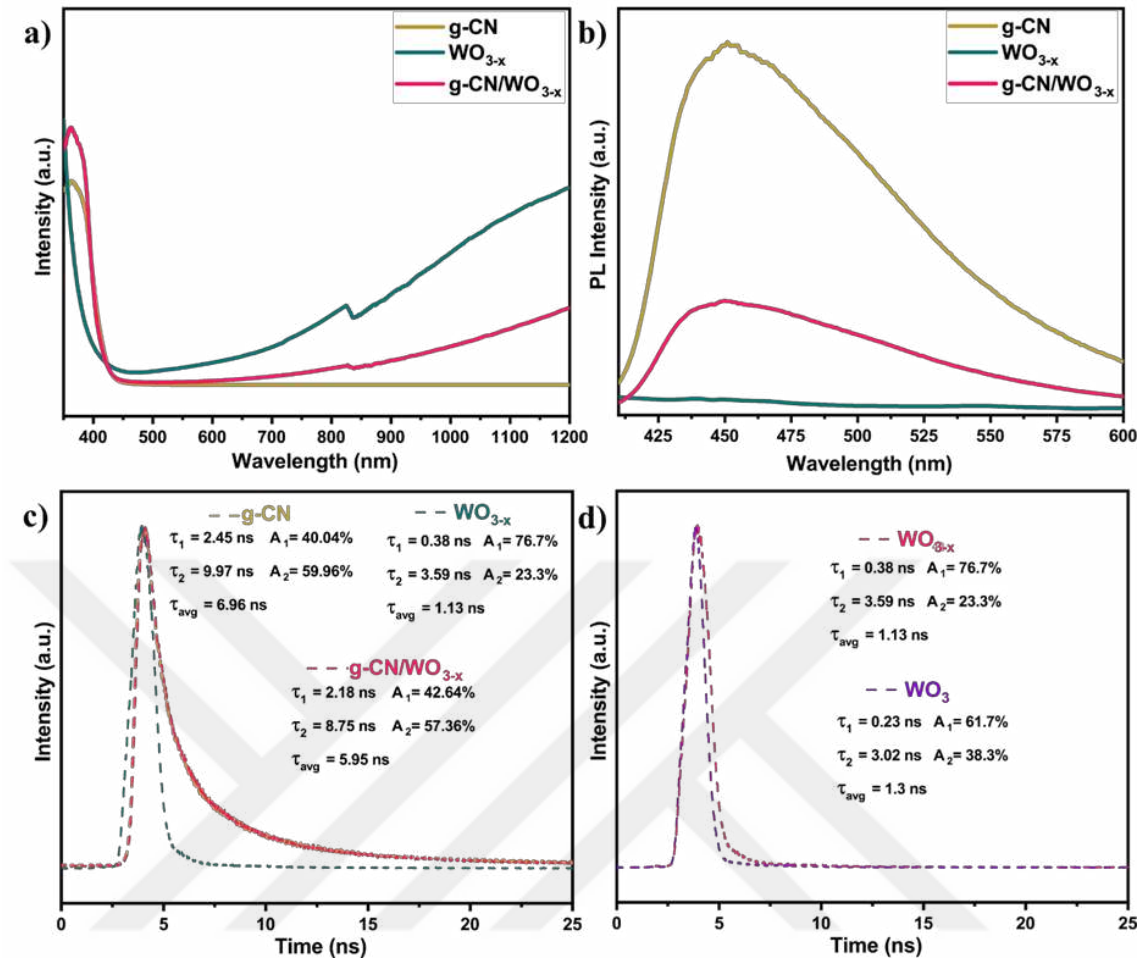

Figure 4.15: a) UV-Vis-NIR absorption **b)** PL **c)** TRPL spectra of g-CN, WO_{3-x} and g-CN/WO_{3-x} **d)** TRPL spectra of WO_3 and WO_{3-x}

In this study, one of the main goals is to synthesize WO_{3-x} by generating oxygen vacancy on the surface of WO_3. In a word, a great number of point defects on the crystal structure were created intentionally, and ultimately, non-radiative recombination become an attention-getting parameter to interpret effect of oxygen vacancy on charge transport mechanism. In this respect, a type of non-radiative decay Shockley-Read-Hall (SRH) recombination, also known as trap-mediated recombination becomes a concern. SRH recombination occurs in the presence of disordered structure, indicating point and structural defects. According to type and location of defect in the structure, they act as a trap states near to band edges or in forbidden gap to catch charge carriers [151]. Vacancy type-point defects as in WO_{3-x} create shallow trap states at band edges, while other defect types including dislocations, voids, interstitials etc. can cause deep traps that are located within forbidden gap (E_g) [152]. In simple, at a SRH recombination process, an electron

falling from CB is captured by a trap state, and if a hole in VB reach to same energy state with electron, e^--h^+ pair is annihilated, and heat is produced instead of photon [153]. Although SRH recombination can be problematic for stability of photocatalyst, it brings some advantages such as photothermal/thermal effect and suppression of radiative decay in chemical reaction. In particular, TRPL spectra of WO_3 and WO_{3-x} were given in **Figure 4.15d**. As compared to A_1 (61.7%) of stoichiometric WO_3 which indicates to amplitude of non-radiative decay, that of WO_{3-x} (76.7%) was more predominating in total amplitude. This outcome stated that more non-radiative decay occurred in WO_{3-x} structure. Since high percentage of non-radiative decay in WO_{3-x} was associated with more hot electron production, during recombination of them at trap states or their emitting into CB from trap states, these electrons dissipated their energy through electron-phonon coupling, resulting in localized heating of photocatalyst surface [154,155]. In addition, τ_{avg} value of WO_{3-x} was faster than WO_3 due to huge concentration of oxygen vacancy, enabling more e^- and h^+ for photochemical reactions by limiting radiative recombination.

To investigate charge migration and separation efficiency of binary heterojunction, transient photocurrent measurement was performed (**Figure 4.16a**). It was recorded that WO_{3-x} manifested the lowest photocurrent density among all-synthesized photocatalyst, but its current density increased with time, indicating more effective charge separation. Photocurrent density of g-CN was quite high in comparison to WO_{3-x}, yet it followed similar behavior that density increases with time. In g-CN/WO_{3-x} heterojunction, photocurrent density raised resplendently, pointing out efficient charge separation of S-scheme heterojunction. However, unlike pristine semiconductors, current density of binary heterojunction declined with increasing time after a while, causing efficiency loss in photocatalytic activity.

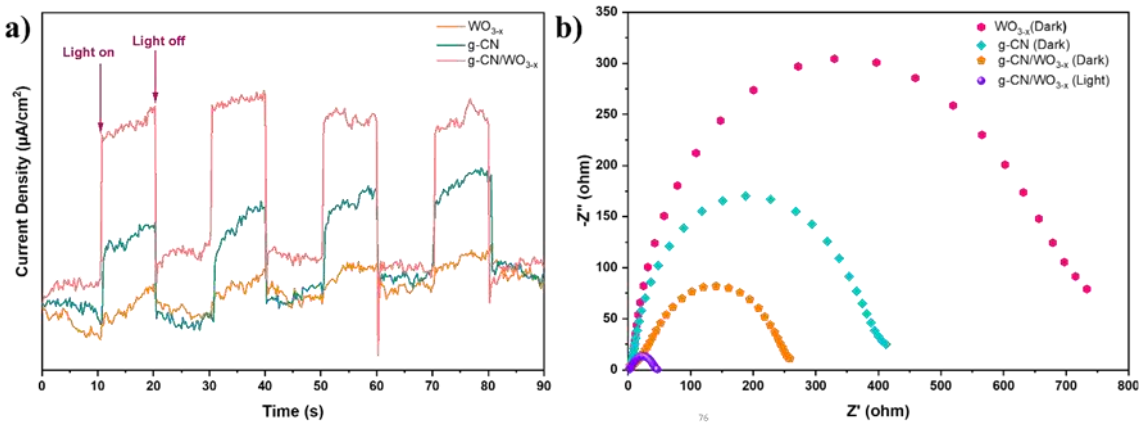

Figure 4.16: a) Transient photocurrent responses and **b)** Nyquist Plots of WO_{3-x}, g-CN and g-CN/WO_{3-x}

4.3 g-CN/WO_{3-x} Heterojunction for Photocatalytic Methyl Orange Degradation

Photodegradation performance of g-CN/WO_{3-x} against MO was found as 98% during optimization experiments. In the following step, g-CN, WO_{3-x}, g-CN/WO_3 and g-CN/WO_{3-x} heterojunctions were assayed to their activities in MO degradation (**Figure 4.17a**). As it can be seen by the plot in **Figure 4.17a**, the photolysis of MO solution was extremely limited. Therefore, severe diminishment in MO concentration with increasing time stemmed from the photocatalytic process. Besides, photocatalytic activity of g-CN/WO_3 against MO was detected as 58%, which can be examined as low in comparison to activity of g-CN/WO_{3-x} (98%). In the case of pristine g-CN, degradation efficiency was measured to be 51.60%. However, surprising photocatalytic activity with 91% was obtained by pristine WO_{3-x} since CB of WO_{3-x} does not have appropriate potential to produce $\bullet O_2^-$ which is the most significant participant for reduction reactions. In this regard, this exceptional activity was ascribed to photothermal effect resulting from hot electron generation and excess number of free electrons in the structure. Also, rate constants of these photocatalyst was calculated by applying first-order equation (**Eq. 3.2**)(**Figure 4.17b**). Results manifested that reaction rate k value of g-CN/WO_{3-x} heterojunction is determined as 0.15816 min^{-1} at the end of experiment which is 4.99 and 1.47 times higher than g-CN (k= 0.03169 min^{-1}) and WO_{3-x} (k= 0.10747 min^{-1}), respectively. As it was aforementioned, 81% of MO is exposed to degradation due to fast

reaction kinetics of g-CN/WO_{3-x} heterojunction photocatalyst in the first 5 minutes. For degradation of remaining dye, more time was spent due to low concentration of MO, causing decrease in rate constant k. In this regard, reaction rate was examined at the end of 15 minute when degradation efficiency of binary photocatalyst exceeds to 90%, and it was seen that rate constant increases to 0.1747 min^{-1} (the **inset plot in Figure 4.17b**). Considering two reaction constants, it can be said that g-CN/WO_{3-x} outperformed in dye degradation as compared to other binary and ternary heterojunctions in current literature (**Table 4.1**).

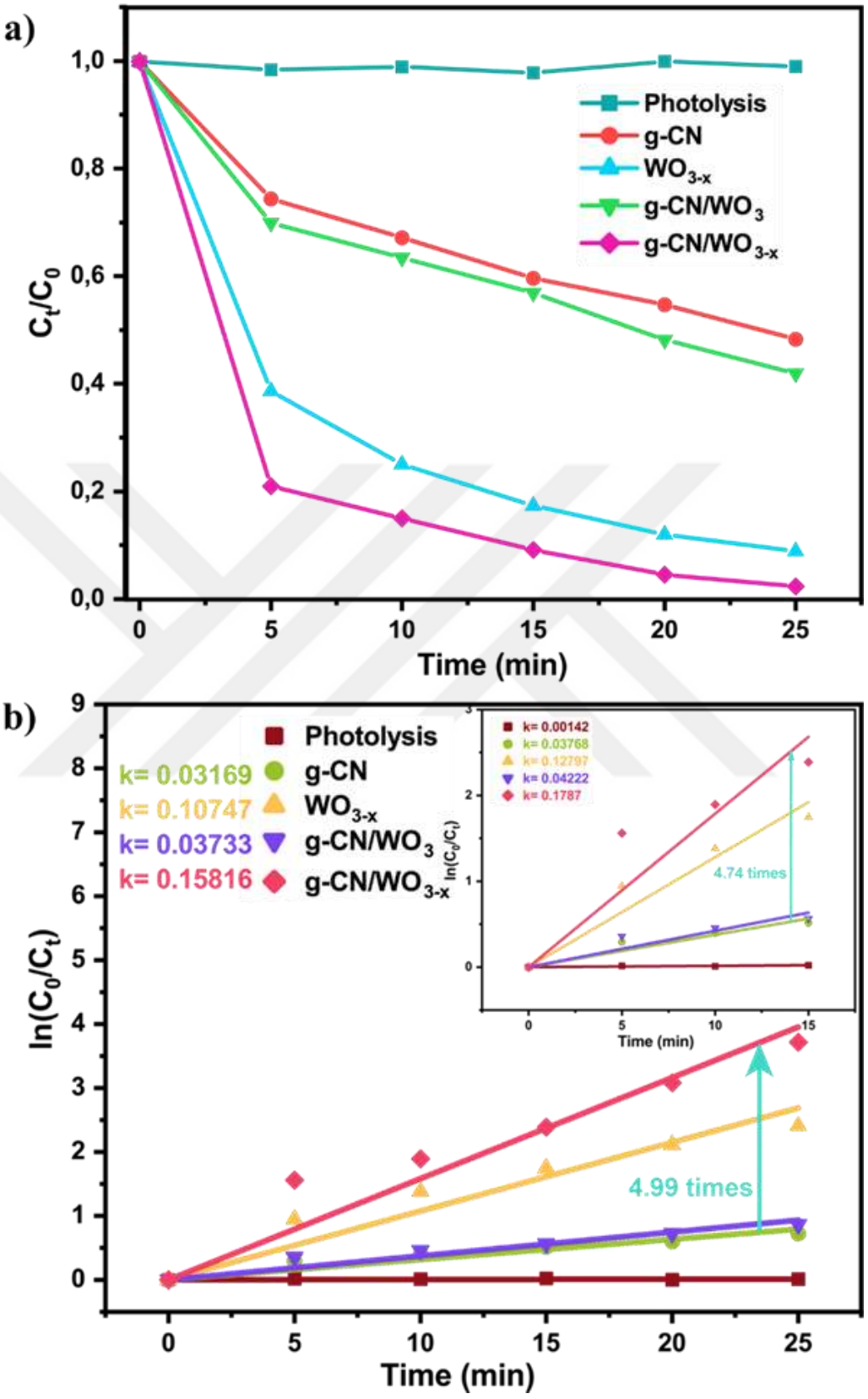

Figure 4.17: a) MO degradation performance of as-synthesized photocatalysts and **b)** related reaction kinetics

Table 4.1: Reported reaction rate (k) values of different heterojunctions in photodegradation of different dyes and antibiotics

Photocatalyst	Amount g/L	Light	Pollution (mg/L)	Reaction rate k (min^{-1})	Reference
$CuNb_2O_6$/g-C_3N_4	0.2	500W Xenon (400-780nm)	RhB MB MO Cr(VI)	0.039 0.02050 0.00103 0.0149	[57]
GQDs@CNBP	0.3	150W Halogen ($\lambda > 400$ nm)	5 (MO) 50 (TC)	0.1415 0.0371	[156]
C_3N_4/N-CQDs/ $W_{18}O_{49}$	0.1	150W Xenon ($\lambda > 365$ nm)	10 (MB) 10 (MO)	≈ 100% (90min) ≈ 100%(120min)	[77]
Ag/$WO_{2.9}$/g-C_3N_4	0.5	500W Xenon ($\lambda > 420$ nm)	10 (RhB) 10 (MB) 10 (MO)	90% (240 min) 96% (270 min) 93% (330 min)	[157]
Black TiO_2/g-C_3N_4	1	300W Xenon ($\lambda > 420$ nm)	10 (MO)	0.0153	[158]
$W_{18}O_{49}$/g-C_3N_4	0.2	300W Xenon ($\lambda > 420$ nm)	10 (RhB)	0.23	[74]
MoS_2/g-C_3N_4	0.625	100W lamb ($\lambda > 400$ nm)	30 (RhB)	0.0038	[159]
BiOBr/g-C_3N_4	0.3	300W Xenon ($\lambda > 400$ nm)	10 (RhB)	0.01274	[55]
B-g-C_3N_4/ $CdIn_2S_4$	1	300W Xenon	10 (MO)	90% (120 min)	[160]
g-CN/WO_{3-x}	0.3	150W Halogen lamp ($\lambda > 400$ nm)	5 (MO)	0.1787 (15 min) 0.1582 (25 min)	**In this study**

4.4 *g-CN/WO_{3-x} Heterojunction for Photocatalytic Hydrogen Peroxide Generation*

4.4.1 Hydrogen Peroxide Generation

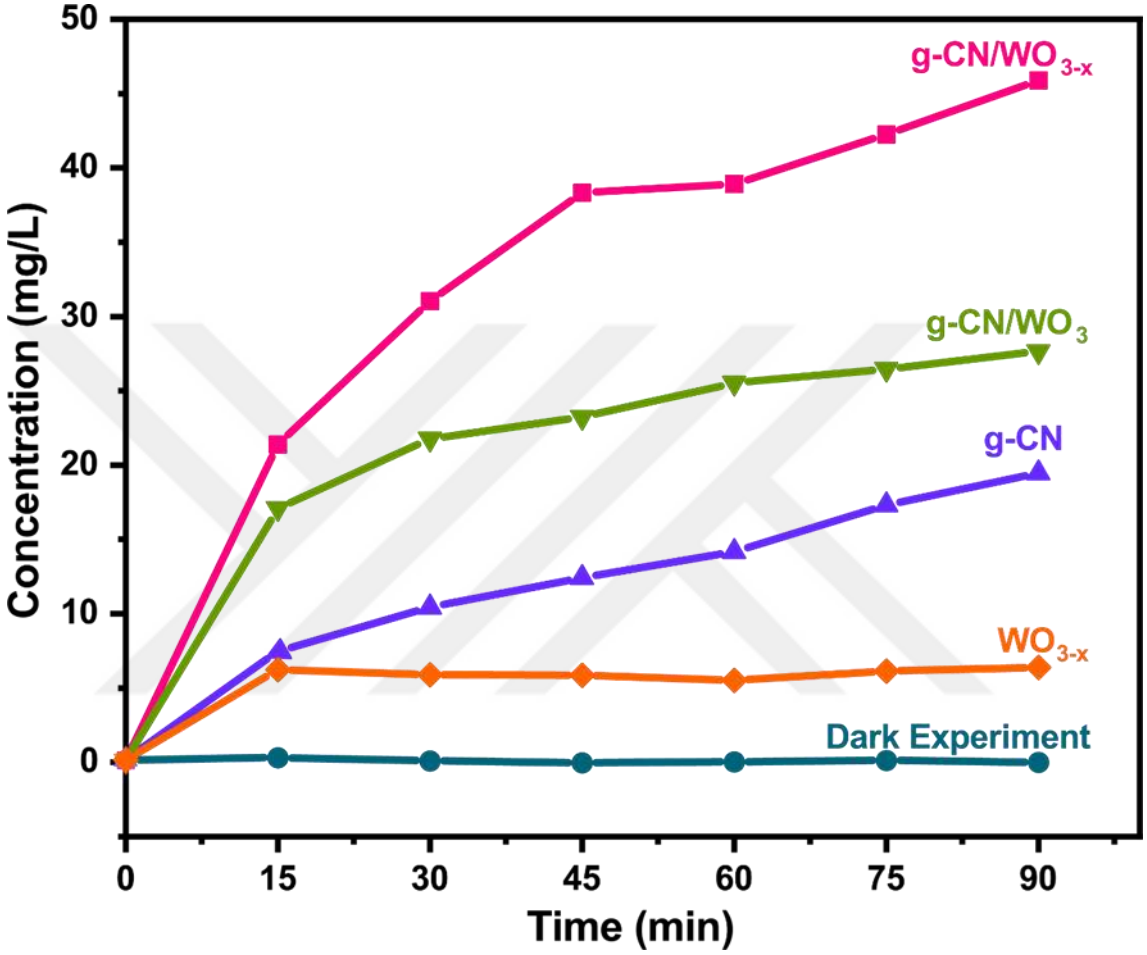

Figure 4.18: Photocatalytic H_2O_2 production activity of g-CN, WO_{3-x}, g-CN/WO_3 and g-CN/WO_{3-x} vs. time

In the presence of only water as a solvent in reaction medium, H_2O_2 decomposition rate became dominant to H_2O_2 generation rate after a while, and although produced H_2O_2 amount was around 12.3 mg/L at first 15 minutes, this value decreased gradually during experiment (**Figure 4.19**). The reason of this issue is a general problem at photocatalytic H_2O_2 production by using semiconductor metal oxides with high VB as photocatalysts, and in current study, the problem is that photo-induced holes at the VB of WO_{3-x} gives rise to decomposition of the photo-catalytically generated H_2O_2. Therefore, 10 wt% MeOH was included in the reaction media to scavenge holes in VB. First experiments

were conducted in dark conditions, and it was seen that there was no considerable H_2O_2 production. When the same reaction was conducted under visible light illumination, superior photocatalytic activity of 45.9 mg/L H_2O_2 was obtained. Results in dark and light conditions revealed that generation of H_2O_2 was a success of totally photocatalytic reactions (**Figure 4.18**). Furthermore, the H_2O_2 generation performance of g-CN/WO_{3-x} heterojunction photocatalyst is competitive among other metal-free binary and ternary heterojunctions reported in the literature (**Table 4.2**). In addition to g-CN/WO_{3-x} heterojunctions, photocatalytic activities of g-CN, WO_{3-x} and g-CN/WO_3 was examined. While in g-CN case, it was found that concentration of H_2O_2 was 19.46 mg/L, photoactivity of WO_{3-x} was restricted with 6.40 mg/L H_2O_2. Keeping in mind its MO degradation performance, this H_2O_2 production value could be evaluated as low. However, W-OOH forms due to attack of the generated H_2O_2 on vacant site of W metal [161]. This operation caused dissociation of H_2O_2, and reduction in photocatalytic activity of WO_{3-x}. The last photocatalyst g-CN/WO_3 showed a performance of 27.67 mg/L in H_2O_2 generation. The performance difference between g-CN/WO_{3-x} and g-CN/WO_3 could be ascribed to effect of hot electrons, and their photothermal contribution, and oxygen-vacancies on the crystal structure of WO_{3-x}. First, the generated high-energy electrons driving by LSPR were extra electrons for photochemical reactions, increasing photo-efficiency [155]. Moreover, current literature remarked that relaxation of these highly energetic electrons brings about extreme temperature increase, and through electron-phonon coupling, their energies released to surface of photocatalyst in the form of heat to cool lattice [162]. Wang and colleagues demonstrated that oxygen reduction reaction (ORR) and water oxidation reaction (WOR) kinetics are enhanced as photothermal effect lowers the energy barrier of related reactions, and consequently, more H_2O_2 was produced [62]. Besides providing hot electron to heterojunction, the other mission of oxygen vacancies is to behave as active sites for adsorption of reactant molecules onto photocatalyst surface [68].

4.4.2 Effect of Different Alcohols as Hole Scavenger on the Photocatalytic Hydrogen Peroxide Production in the presence of g-CN/WO_{3-x} heterojunction

In this study, methanol was added to reaction environment for analyzing H_2O_2 generation potentiality of all synthesized photocatalysts. However, aliphatic alcohols are employed as hole scavenger in general, and their performance alter according to carbon chain length and position of -OH bond. In this scope, ethanol, isopropanol and n-butanol were also examined as hole scavengers for g-CN/WO_{3-x} binary heterojunction by keeping the 10 wt % scavenger rate constant. Their effects on H_2O_2 generation was graphed in **Figure 4.19.**

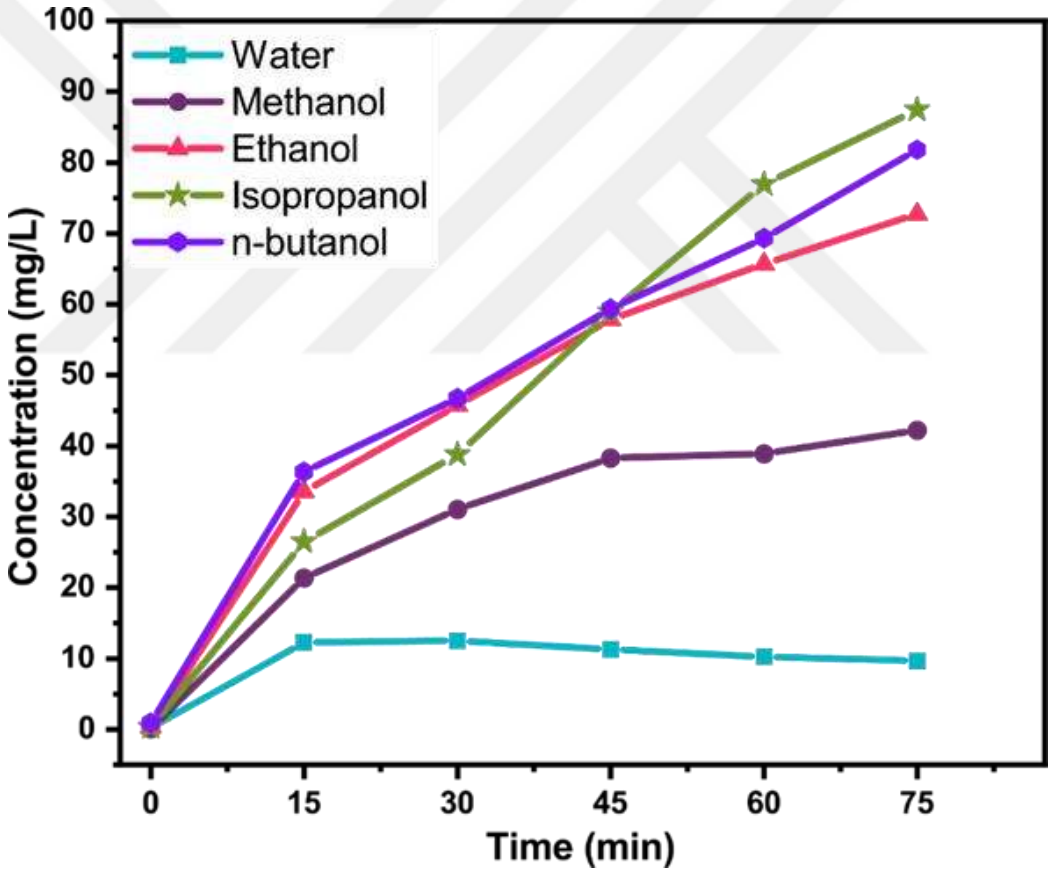

Figure 4.19: Photocatalytic H_2O_2 production activity of g-CN/WO_{3-x} heterojunction in only water and in water-10 wt% alcohol solutions vs. time

g-CN/WO_{3-x} in water-10 wt% methanol mixed solution displayed 42.3 mg/L of H_2O_2 generation in 75 minutes, while the amount of formed H_2O_2 was measured as 72.71 mg/L, 87.44 mg/L and 81.85 mg/L in the presence of ethanol, isopropanol and n-butanol

as hole scavengers. In the literature, efficiency of different scavengers varies at different applications. However, result of only study that focused on effect of aliphatic alcohols as scavengers on photocatalytic H_2O_2 production over TiO_2 is consistent with outcomes in this work [169]. Furthermore, in the current literature, it was proven that iso-alcohols exhibit stronger capability to produce H_2O_2 as compared to n-alcohols [170]. Another important parameter about scavengers is their adsorption energy to photocatalyst surface since the higher adsorption energy indicates more stable and stronger interaction of scavenger with photocatalyst surface. In the current literature, studies on metal oxides were inferred the adsorption energy of isopropanol is the highest among alcohols in this work. In addition, reason of higher adsorption energy of isopropanol than n-butanol is attributed to –OH position, stemming from more repulsive force between 2 methyl group and bridging surface oxygen [171]. This result explained activity difference between isopropanol and n-butanol. Besides, HOMO levels of substances evince reactivity of them against electrophilic species. In this regard, DFT calculations revealed that isopropanol has higher HOMO energy than ethanol and methanol but slightly lower than n-butanol. This means that photogenerated holes of semiconductor attack to isopropanol and n-butanol in a faster and stronger way. Moreover, HOMO-LUMO gap is one of the indicators to explain the highest activity in isopropanol since isopropanol has smaller gap among these alcohols, causing robust tendency to oxidation [169, 171]. In this way, isopropanol supplies more electron to heterojunction system. Another reason is back-oxidation process of alcohols. Diffusion rate of produced $\bullet C_3H_6OH$ free radicals in case of isopropanol is poor as compared to that of ethanol and methanol owing to larger and weightier molecule. Moreover, its reactivity is less. In this way, back-oxidation process is suppressed almost completely in isopropanol case, and it feeds CB of photocatalyst by sending e^-s [172]. All these reasons stated clearly why g-CN/ WO_{3-x} generates the highest amount of H_2O_2 in the presence of isopropanol as a hole scavenger.

Table 4.2: Comparison about H_2O_2 generation of g-CN/WO_{3-x} with reported results in the literature

Photocatalyst	Amount g/L	Light	Sacrificial Agent (wt)	H_2O_2 Yield	Ref
$Bi_4O_5Br_2$/g-C_3N_4	1	300W Xenon ($\lambda > 420$ nm)	—	124 μM (1h)	[59]
C_3N_4/ $NiIn_2S_4$	0.4	300W Xenon ($\lambda > 420$ nm)	10% ethanol *O_2 saturated*	1080 $\mu mol \cdot L^{-1} \cdot h^{-1}$	[60]
ZnO/g-C_3N_4	0.4	300W Xenon ($\lambda > 350$ nm)	10% ethanol *O_2 saturated*	1544 $\mu mol \cdot L^{-1} \cdot h^{-1}$	[163]
CoO_x/Mo:$BiVO_4$ /Pd	2	300W Xenon ($\lambda > 420$ nm)	— *O_2 saturated*	1425 $\mu M \cdot h^{-1}$	[164]
FS-COF	0.25	300W Xenon ($\lambda > 420$ nm)	— *O_2 saturated*	3904.2 $\mu mol \cdot h^{-1} \cdot g^{-1}$	[165]
$ZnIn_2S_4$@$BiVO_4$	0.333	300W Xenon (400 nm-1000 nm)	— *O_2 saturated*	1.8 $mmol \cdot g^{-1} \cdot h^{-1}$	[166]
WO_3/CN	0.5	300W Xenon ($\lambda > 400$ nm)	5% ethanol *O_2 saturated*	322 $\mu mol \cdot g^{-1} \cdot h^{-1}$	[167]
rGO decorated $W_{18}O_{49}$ @g-C_3N_4	0.2	300W Xenon (400 nm-780 nm)	— *O_2 saturated*	49.4 $\mu mol \cdot g^{-1} \cdot h^{-1}$	[80]
Co_9S_8/$CoZnIn_2S_4$	0.286	300W Xenon ($\lambda > 420$ nm)	29% benzyl alcohol *O_2 saturated*	49.5 $mmol \cdot L^{-1}$	[168]
gCN/WO_{3-x}	1	150W Halogen ($\lambda > 400$ nm)	10% methanol	1349.7 $\mu mol \cdot L^{-1}$ (1.5h)	**This study**
gCN/WO_{3-x}	1	150W Halogen ($\lambda > 400$ nm)	10% ethanol	1.712 $mmol \cdot L^{-1} \cdot h^{-1}$	**This study**
gCN/WO_{3-x}	1	150W Halogen ($\lambda > 400$ nm)	10% isopropanol	2.1 $mmol \cdot L^{-1} \cdot h^{-1}$	**This study**
gCN/WO_{3-x}	1	150W Halogen ($\lambda > 400$ nm)	10% n-butanol	1.93 $mmol \cdot L^{-1} \cdot h^{-1}$	**This study**

4.5 Band Alignments

Understanding of individual semiconductors' band structures and heterojunction mode between them are crucial to get maximum efficiency from photochemical reaction. Considering this strategy, first, investigating band edge potentials of g-CN and WO_{3-x} was planned. However, there is no electrochemical or optical method to determine valance and conduction bands directly. At this point, to know flat band potential of a semiconductor is an option to estimate band potentials of semiconductor [118].

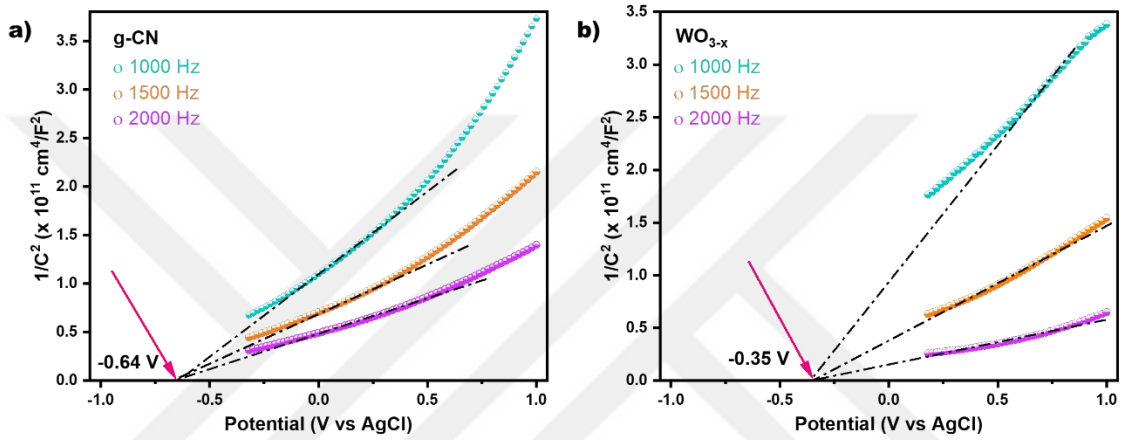

Figure 4.20: Mott-Schottky plot of **a)** g-CN **b)** WO_{3-x} at 1000, 1500 and 2000 Hz

To find flat band potential (V_{fb}) and semiconductor type, Mott-Schottky plot was considered. **Figure 4.20** demonstrates Mott-Schottky plots belonging to g-CN and WO_{3-x} at 1000, 1500 and 2000 Hertz. For both g-CN (**Figure 4.20a**) and WO_{3-x} (**Figure 4.20b**), slopes at various frequencies are positive, indicating the n-type semiconductors. Interception point of tangent lines with x axis, namely flat-band potential was found as -0.64 V for g-CN and -0.35 V for WO_{3-x}. By using **Eq. 3.10** flat band potential was converted from Ag/AgCl to NHE. As mentioned in **chapter 3.10.3**, flat band potential is described as Fermi level [118] and consequently, Fermi levels of g-CN and WO_{3-x} were calculated as -0.435 V and -0.145 V respectively. In n-type semiconductor, conduction band potential is located at a position 0-0.2 V more negative than Fermi level [173]. Therefore, by presuming the value as 0.1 V, conduction band potentials of g-CN and WO_{3-x} was set as -0.54 V and -0.25 V in order.

Tauc Plot is an extensively used method for determination of optical bandgap. By using **Eq. 3.8** where γ value is 2 because semiconductors g-CN and WO_{3-x} show the

indirect bandgap profile, the Tauc Plot was drawn, and it was seen that band gap energies of g-CN and WO_{3-x} was 2.71 eV and 2.94 eV, respectively in **Figure 4.21.**

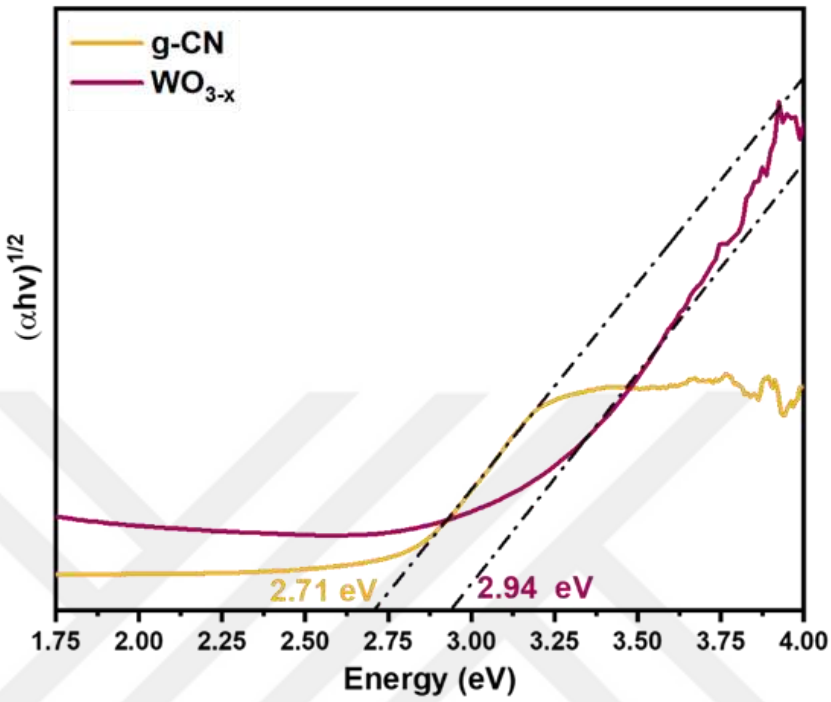

Figure 4.21: Tauc plots of g-CN and WO_{3-x}

In the final step, XPS-VB potential of g-CN and WO_{3-x} was calculated with linear extrapolation in **Figure 4.22**. The VB values were 2.06 eV **(Figure 4.22a)** and 2.6 eV **(Figure 4.22b)** for g-CN and WO_{3-x}, respectively. After application of conversion formula **Eq. 3.6**, VB_{g-CN} was found to be 2.16 V vs. NHE, and VB_{WO3-x} was found as 2.7 V vs NHE. All Mott-Schottky, Tauc Plot and VB-XPS results were consistent with each other. When these were evaluated together, band structures of individual semiconductors were illuminated in **Figure 4.22c**. The proposed band positions tended to form staggered-type heterojunction. In this regard, for accurate determination of heterojunction type, the migration routes of electrons and holes were studied.

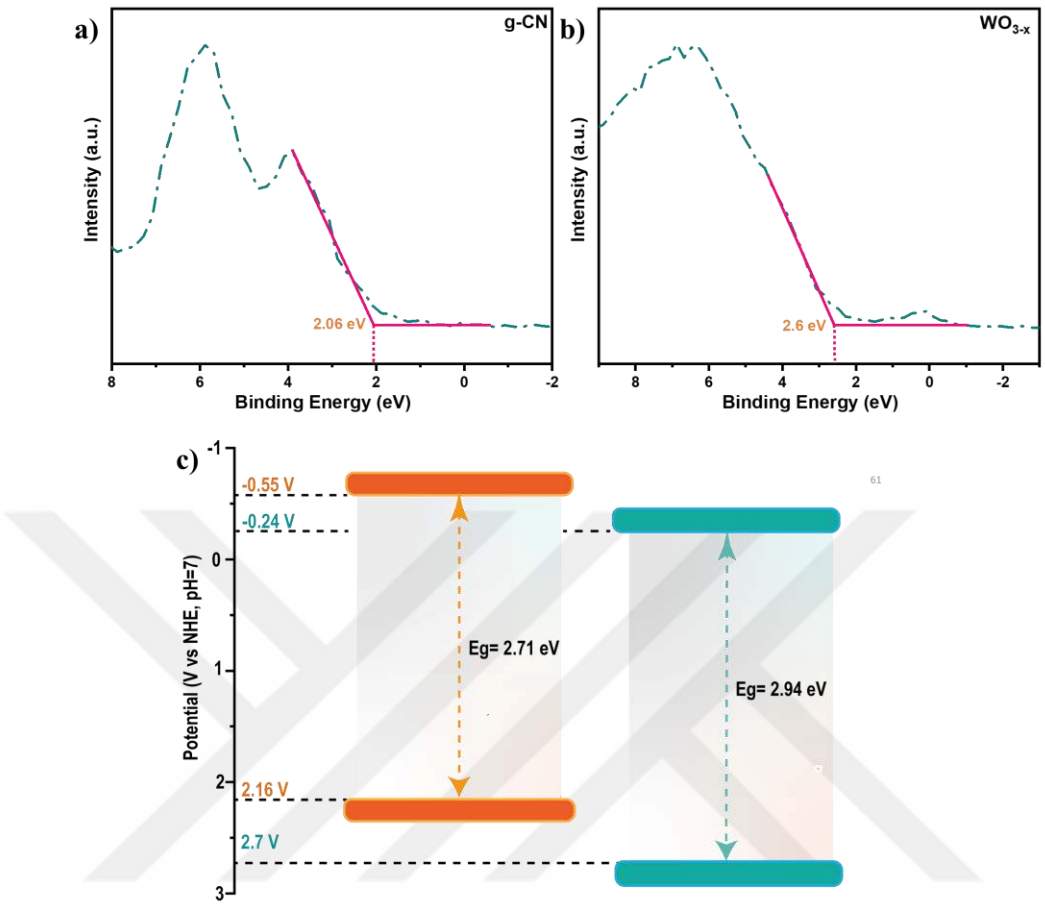

Figure 4.22: XPS-VB spectrum of **a)** g-CN **b)** WO_{3-x} and **c)** band structure of g-CN and WO_{3-x}

Work function (ϕ) is a term to describe the minimum required energy for the removal of an electron from material surface to external vacuum. Its value can be found by subtracting Fermi energy from energy level in vacuum [174]. When a heterojunction forms between two semiconductors, work function difference of material undertakes a key role to design fruitful heterojunction. Reason of that is work function difference arranges electron density at the interface, eventuating in creation of internal electric field that promotes the efficacious charge separation [175]. Therefore, the work functions of g-CN, WO_{3-x} and g-CN/WO_{3-x} were calculated by using XPS-VB spectra based on the following relationship $\phi = \Delta V + \varphi$ which ΔV is contact potential difference and φ is work function of XPS instrument (φ= 4.543 eV) [77]**.** To calculate work function of materials, firstly, ΔV which is energy difference between two inflection points (IP1 and IP2) was

found from XPS-VB spectrum. As shown in **Figure 4.23,** ΔV for g-CN, WO_{3-x} and g-CN/WO_{3-x} was calculated as 6.96, 8.66 and 7.90 eV, respectively. The fact that the work function of the g-CN/WO_{3-x} binary heterojunction had a value between work functions of g-CN and WO_{3-x} showed that the calculations were made correctly and the heterojunction synthesis was successful.

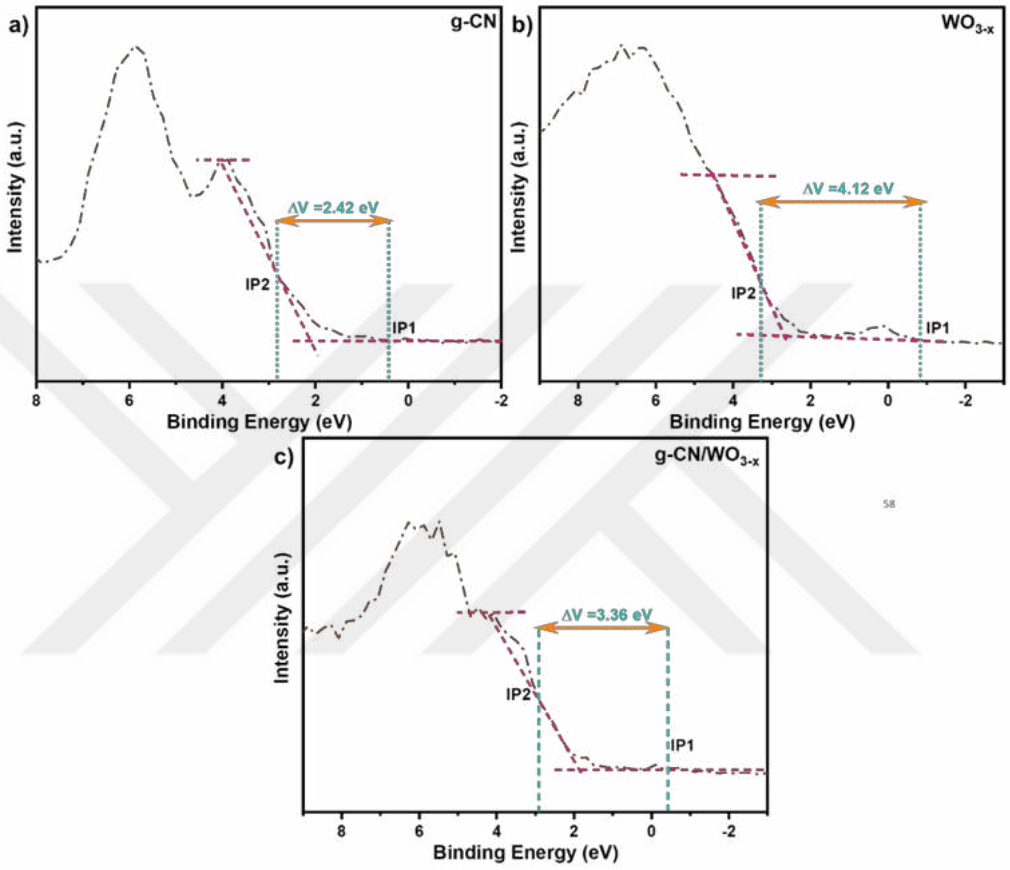

Figure 4.23: Contact potential difference of **a)** g-CN **b)** WO_{3-x} **c)** g-CN/WO_{3-x}

Schematic illustration of individual semiconductors' band positions before contact was given in **Figure 4.24a**. In contact position, since g-CN has smaller work function and higher Fermi level position compared to those of WO_{3-x}, electron flows from g-CN to WO_{3-x} at the interface until their Fermi level will be aligned. As a result, g-CN become positively charged due to loss of an electron, and WO_{3-x} is negatively charged due to the gaining an electron at the interface. Electron depletion layer on g-CN and electron accumulation layer on WO_{3-x} at contact region forms strong polarization, and this polarization is a source of created internal electric field and band bending. While bands

of g-CN bend to upward, WO_{3-x} subjects to downward bending. Furthermore, direction of internal electric field (IEF) is from g-CN to WO_{3-x}, and IEF encourages to electron migration in opposite direction (**Figure 4.24b**) [159]. Upon light irradiation, g-CN and WO_{3-x} produces photo-generated electrons moving to CB of semiconductors. By means of proper band bending, strong IEF and coulombic interaction between opposite charges, electrons in CB of WO_{3-x} and holes in VB of g-CN recombine at heterojunction interface. In this way, photo-induced charges on CB of g-CN and on VB of WO_{3-x}, which they have high redox capability, are retained. This charge transfer mechanism proposed that S-scheme heterojunction is formed between g-CN and WO_{3-x} (**Figure 4.24c**).

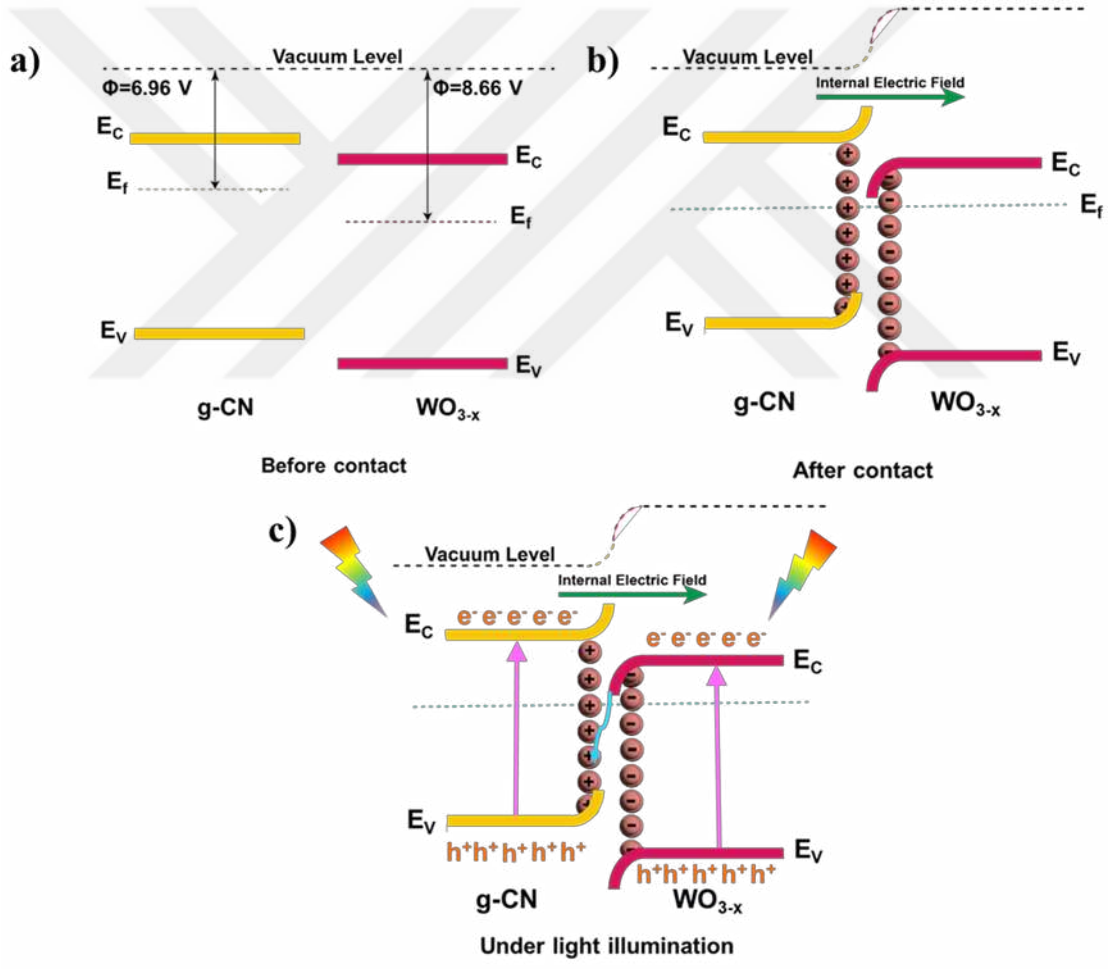

Figure 4.24: Schematic representation of band structures **a)** before contact **b)** after contact **c)** under light illumination

4.6 Reaction Mechanisms

To enlighten reasons of impressively efficacious photoactivity of g-CN/WO_{3-x} heterojunction, some mechanistic studies were designed. In accordance with this purpose, after exploring band positions of semiconductors and heterojunction type that they formed, not only generated radicals and their responsibility in the photochemical reactions, but also effect of hot electrons to the photocatalytic activity was investigated.

4.6.1 Hot electron effects

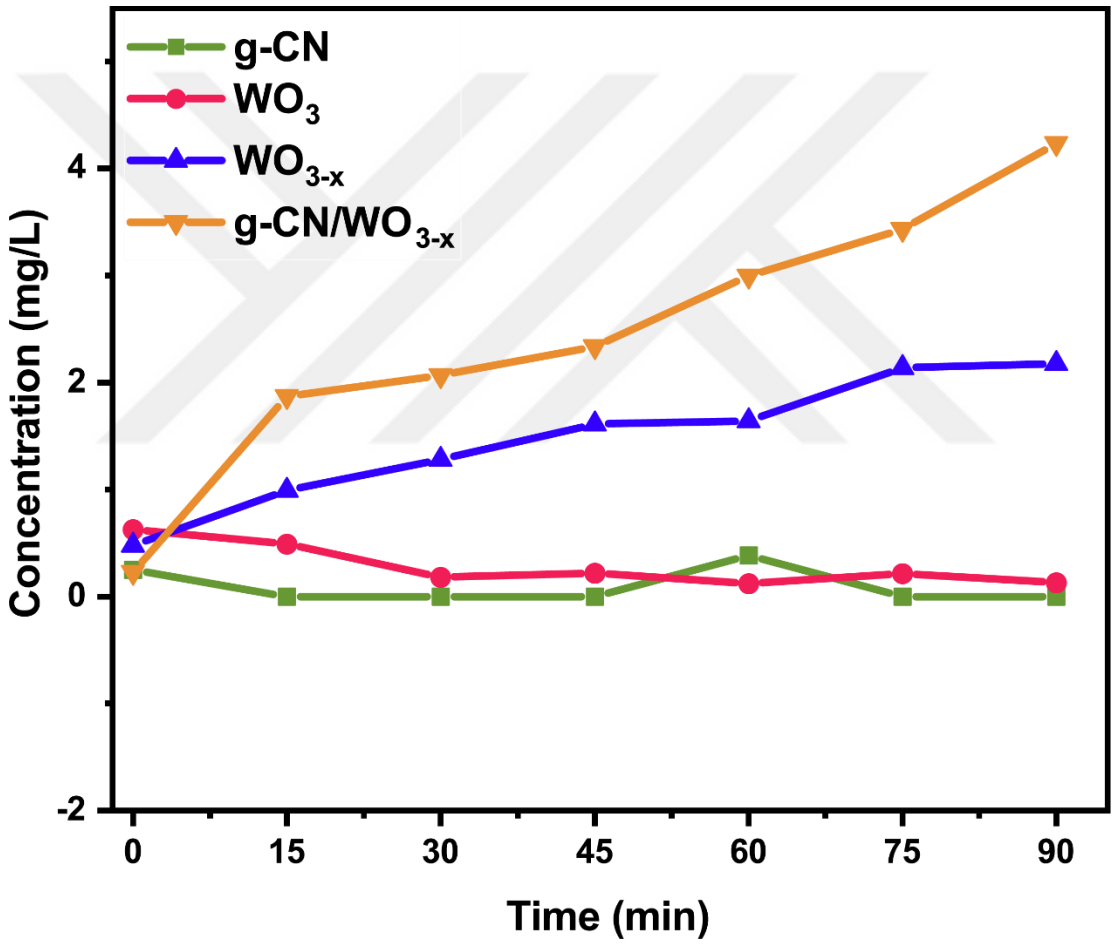

Figure 4.25: H_2O_2 production results of g-CN, WO_{3-x}, g-CN/WO_3 and g-CN/WO_{3-x} vs. time at green light with 530 nm wavelength

g-CN/WO_{3-x} heterojunction has LSPR absorption band owing to huge amount of oxygen vacancy as UV-Vis-NIR DRS showed. LSPR peak makes possible excitation of heterojunction by photons in the range of visible and near-infrared region. In this regard, an experiment was designed, and green light with 530 nm wavelength (LED, 24W) was

chosen as radiation source. H_2O_2 experiment in the presence of MeOH was used for observation of hot electron movement. Results were given in **Figure 4.25**. As expected, g-CN could not generate any H_2O_2 under green light irradiation since it had very low light harvesting ability at this wavelength. Likewise, stoichiometric WO_3 cannot be excited with green light by virtue of limited absorption in visible and near-infrared. However, in the case of WO_{3-x}, small amount of H_2O_2 generation as 2.18 mg/L was observed despite absence of powerful light source. However, it should also be noted that CB potential of WO_{3-x} is not enough for oxygen reduction reaction (ORR) through $\cdot O_2^-$ which requires -0.33 V of CB potential. With the creation of g-CN/WO_{3-x} heterojunction, H_2O_2 production amount increased to 4.23 mg/L under the green light irradiation. As previously explained, g-CN/WO_{3-x} heterojunction photocatalyst has S-scheme heterojunction type, and CB of g-CN and VB of WO_{3-x} serve for reduction and oxidation, respectively. In this context, the increment of H_2O_2 production can be explained by the flow of hot electrons from CB of WO_{3-x} to CB of g-CN. Therefore, both recombination of hot charge carriers was suppressed, and H_2O_2 was produced via $\cdot O_2^-$ thanks to more negative CB of g-CN. These experiments revealed hot electron generation ability of photocatalyst and their plausible pathways during reaction.

4.6.2 Scavenger Experiments

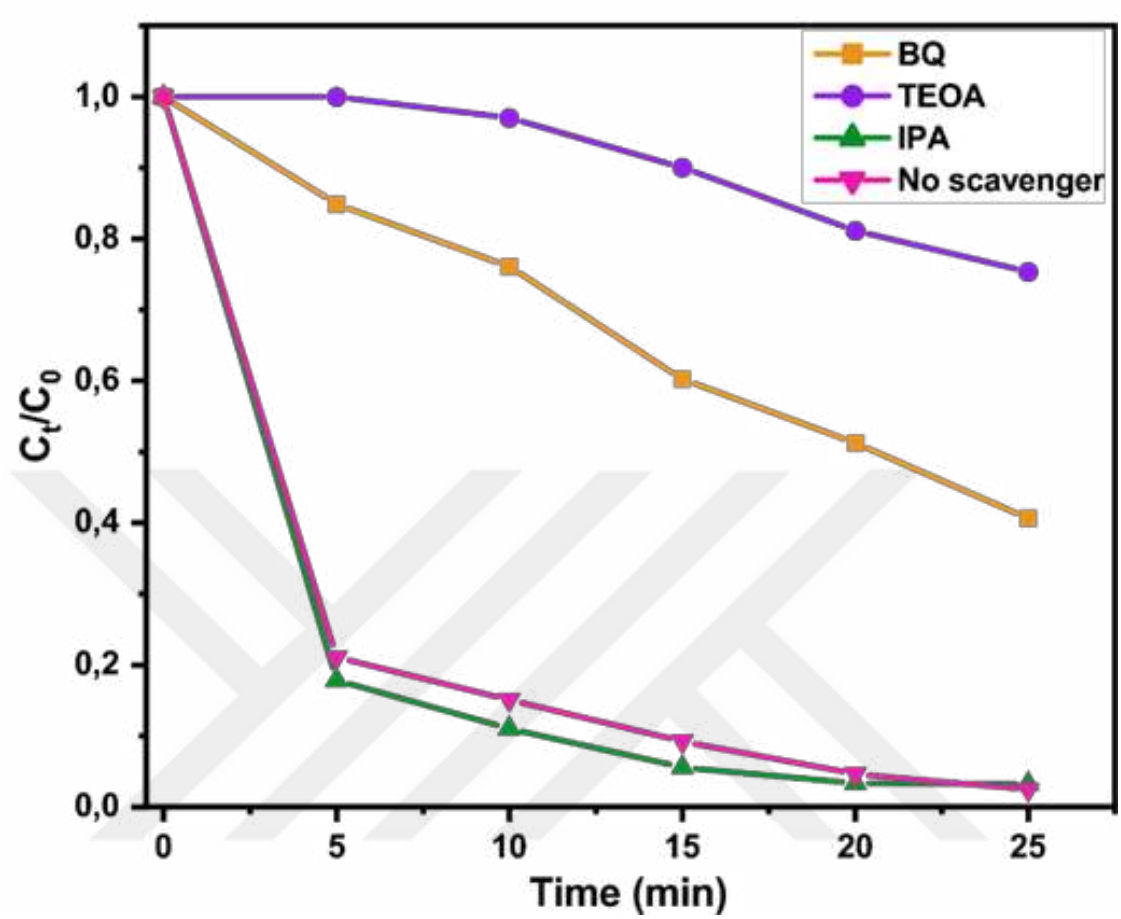

Figure 4.26: MO degradation efficiency of g-CN/WO_{3-x} without scavenger and in the presence of scavengers (BQ, TEOA, IPA)

The first step to explain reaction mechanisms of the photocatalytic MO degradation and H_2O_2 production was the conducting scavenger experiments. In this way, reactive oxygen species (ROS) were involved in reaction medium. Photocatalytic MO degradation was used for scavenger experiments. Sacrificial agents, 1,4-benzoquinone (BQ), triethanolamine (TEOA) and isopropanol (IPA) was used to trap e^-/•O_2^- , h^+ and •OH radicals. Due to extremely fast reaction kinetics, 3 equivalent of specific trapping agent was added in the reaction medium just before halogen lamp was opened. In the absence of scavenger, g-CN/WO_{3-x} degraded 5 ppm MO 98% in 25 min. When BQ was added to MO solution, degradation efficiency of binary heterojunction decreased to 59%. In the presence of TEOA as a hole scavenger, a surprising result was obtained since MO photodegradation performance of g-CN/WO_{3-x} against became 24.7%, which is less than

that of BQ. As a result of scavenger experiments, it was unveiled that photogenerated h^+s give main contribution to reaction and then followed by e^-/$\bullet O_2^-$ (**Figure 4.26**). However, WO_{3-x} behaves as highly doped n-type semiconductor with excess number of e^-, and hot electrons are released from WO_{3-x} under appropriate light irradiation. BQ has ability to scavenge superoxide ($\bullet O_2^-$) radicals and electrons in CB of material. However, BQ is not the best option to trap hot electrons since these electrons move in femtoseconds but BQ is slower [176]. Therefore, effect of e^- to photochemical reactions could not be illuminated clearly because BQ could not capture hot electrons. At the next step, MO degradation experiment was conducted in the presence of IPA for trapping of •OH. However, IPA did not show any negative effect to reaction, contrarily reaction kinetics enhanced at observed time intervals as IPA traps •OH radicals as well as photogenerated holes vigorously by explained causes in **chapter 4.5.2**.

Terephthalic acid (TA) test was performed for determination of ·OH radicals in reaction medium after unsuccessful IPA experiments. TA forms hydroxylated terephthalic acid (HTA) in the presence of •OH radical, and HTA is a PL-active material, giving strong emission around 425 nm. In this case, photocatalytic H_2O_2 formation experiments were conducted and PL results at the end of reaction time (90 min) were compared (**Figure 4.27**). At the first experiment, namely no-scavenger, there was no sacrificial agent for hole or electron in the reaction medium because total amount of generated •OH radicals was aimed to defined. The PL result of no-scavenger case proved that g-CN/WO_{3-x} binary heterojunctionhas ability to produce •OH radical under light illumination. In the second experiment, methanol was added to reaction medium as a hole scavenger to analyze whether hydroxyl produced through e^-/$\bullet O_2^-$. According to PL results, it can be said that there was almost no peak formation in the presence of MeOH. It means that produced ·OH radicals in the no-scavenger experiment is associated to available holes in the VB of WO_{3-x}. In the last experiment, BQ as e^-/$\bullet O_2^-$ scavenger was added to reaction medium instead of MeOH. In this way, the contribution of e^-/$\bullet O_2^-$ to production of •OH was eliminated, and only effect of h^+s on •OH production was evaluated. PL result of third experiment revealed that holes are the main species responsible from •OH generation. Another result of these experiments, g-CN/WO_{3-x} has required valance band potential to produce •OH.

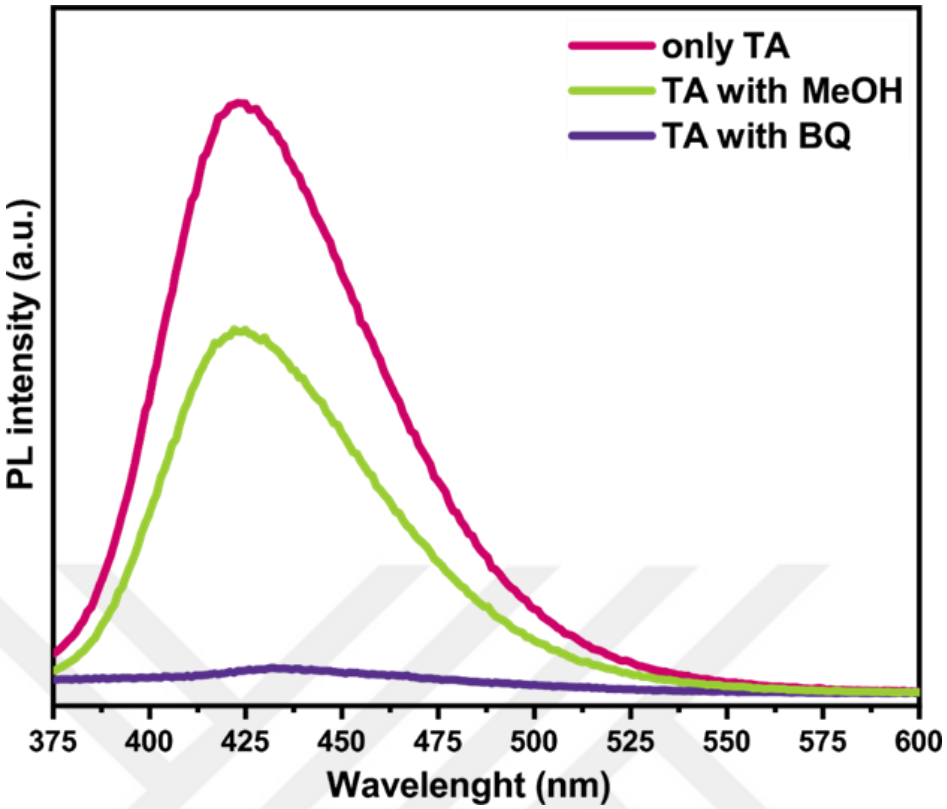

Figure 4.27: PL spectra change of terephthalic acid with addition of methanol and 1,4-benzoquinone

General reaction mechanisms for MO degradation and H_2O_2 generation proceeding from reactive species was explained in detail at the introduction section of thesis (**Eq. 1.1- Eq. 1.9** and **Eq. 1.10-Eq. 1.18**). At this section with the help of scavenger experiments and TA tests, reaction mechanisms of MO degradation and H_2O_2 generation on g-CN/WO_{3-x} was proposed (**Fig. 4.28**). Based on scavenger experiments, first the potential MO degradation mechanism was explained. After excitation of g-CN/WO_{3-x}, a great number of electron and hole was generated **(Eq. 1.1)**. Due to lack of hole scavenger in MO solution, present holes in reaction medium could be used effectively. In this regard, reaction in **Eq. 1.2** took place, and •OH was formed through water oxidation reaction as TA tests unveiled. The reason why holes have the most powerful contribution on the photodegradation performance of the g-CN/WO_{3-x} was that they supplied dissolved oxygen and H^+ to the system through water ionization (**Eq. 1.10**) for the continuation of the reaction, and then produced •OH radicals to reaction environment. According to scavenger experiment results, e^-/•O_2^- couple has also an impact on the photoreaction mechanism severely owing to reactions in **Eq. 1.3 - Eq. 1.6 and 1.9**.

In H_2O_2 production case, owing to availability of MeOH as hole scavenger, holes were not main species to drive reaction. As TA tests illuminated, MeOH also suppressed most of •OH generation. Therefore, it is believed that the vast portion of generated H_2O_2 comes from reduction reactions containing e^- and $\bullet O_2^-$. Therefore, ORR were dominant than WOR. Moreover, due to S-scheme heterojunction formation and appropriate band positions of g-CN and WO_{3-x}, it was thought that limited number of holes on WO_{3-x} were used for water oxidation to provide dissolved O_2 (**Eq. 1.10**) because reaction environment was not O_2-saturated in this work. In addition to this, binary heterojunction could conduct both indirect and direct ORR thanks to CB potential of g-CN (-0. 55 V). Therefore, photocatalytic H_2O_2 generation with exceptional performance was achieved through successive reactions shown in **Eq. 1.11-1.15**.

Hot electrons has also positive influence on activity of photocatalyst based on experiments conducted at 530 nm wavelength. These experiments displayed that WO_{3-x} and g-CN/WO_{3-x} photocatalysts have ability to produce hot electron in the presence of green light to participate in redox reactions. For two reactions which are MO degradation and H_2O_2 generation, firstly, g-CN/WO_{3-x} have to be excited with a light that its wavelength in the range of its LSPR peak. Since white light (λ> 400 nm) is used in this study, both photo-induced charges and hot electrons are produced in experiments carried out, concurrently. After excitation, generated hot electrons presumably move to a state which exist due to introduction of huge amount of vacancy below CB of WO_{3-x} denoted as *I*. Hot electrons reaching to this state can follow 2 pathways designated *II* and *III* in **Figure 4.28**. The reason WO_{3-x} exhibited activity at green light was because route *II* was worked. In pathway *II*, hot electrons act to CB of WO_{3-x} to be used in reduction reactions. However, these hot electrons can recombine with hot holes at the state in a nonradiative way, and it is ended up with heat production as proved in the current literature. Presence of pathway *III* was also stated in the literature [162]. Furthermore, hot electron experiments in this thesis is additional proof about pathway III. At this pathway, hot electrons reaching to state jump to CB of g-CN thanks to their highly energetic nature, and thus its recombination is hindered. This explained mechanism demonstrated that LSPR property of binary heterojunction contributed to reaction, resulting in magnificent activity in both photocatalytic MO degradation and H_2O_2 generation.

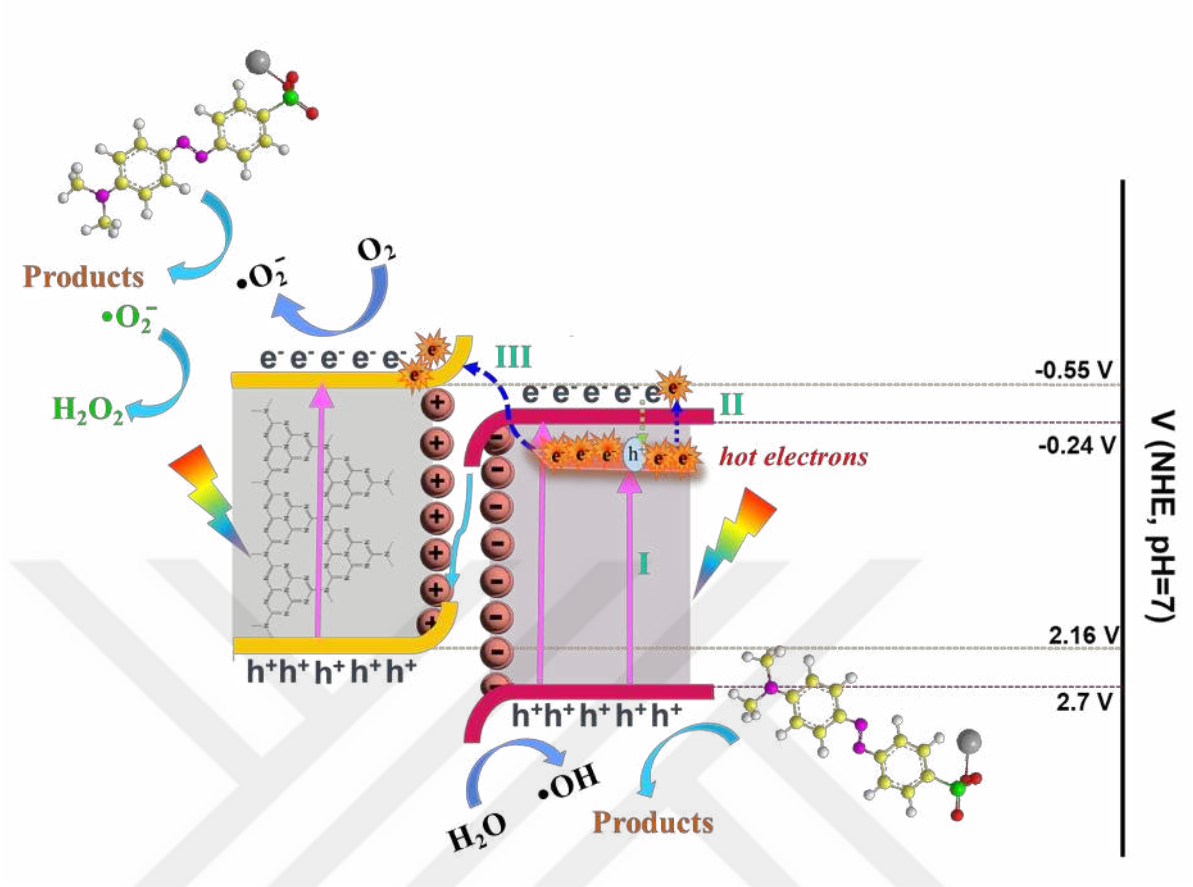

Figure 4.28: Schematic Illustration of proposed reaction mechanism for MO degradation and H_2O_2 generation

4.7 Recyclability of g-CN/WO_{3-x} Heterojunction Photocatalyst

Recyclability tests were carried out to scrutinize stability of photocatalyst, and the test was kept on until outlandish reduction in photoactivity for MO degradation. The variation of the photocatalyst's degradation ability with increasing cycle was reported in **Figure 4.29a**. The photocatalyst that gave 99% degradation efficiency in the first cycle maintained its performance including the third cycle, showing a relatively high activity of 92.68%. Even though photoactivity of g-CN/WO_{3-x} dropped to 83.8% at the end of fourth cycle, the dramatic loss in photocatalyst performance as 20.58% was observed in the fifth cycle compared to fourth one.

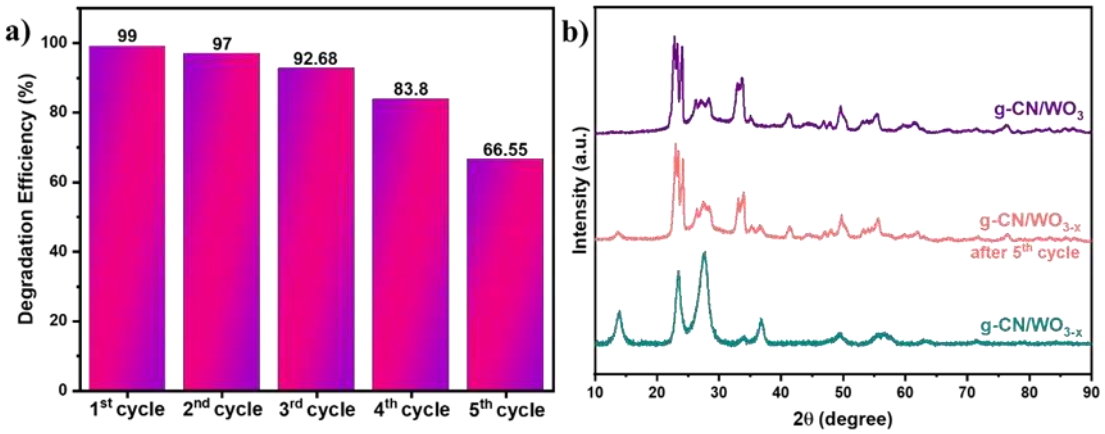

Figure 4.29: g-CN/WO_{3-x} heterojunction's **a)** degradation efficiency for 5 cycle and **b)** XRD analysis after 5th cycle

A post-characterization was performed to explain the dramatic decrease in photocatalytic activity at the 5-cycle. Post-XRD analysis of the binary heterojunction is given in **Figure 4.29.b**. The original XRD pattern of as-synthesized heterojunction was labelled as g-CN/WO_{3-x}. The XRD pattern of used photocatalyst was denoted as g-CN/WO_{3-x} after 5th cycle. As it can be clearly seen, XRD patterns of these two materials differ from one another, and after the 5th cycle, XRD patterns of the heterojunction resembles to that of g-CN/WO_3. This means that crystal structure of WO_{3-x} converts to stoichiometric WO_3 because of the filled vacancies. Occupation of WO_{3-x} vacant sites reduce the number of excess electrons in the structure, and thus disappearing or decreasing the LSPR effect, resulting in activity loss.

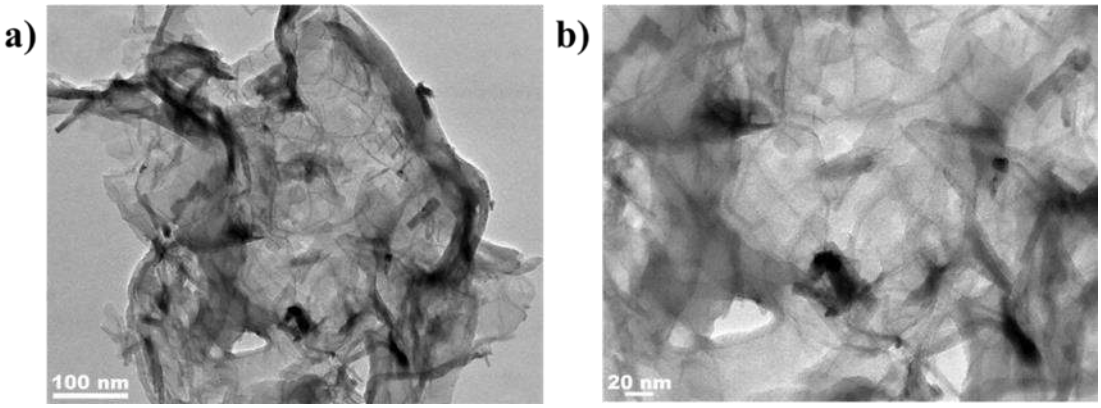

Figure 4.30: TEM images of 5 cycle-used photocatalyst **a)** at high magnification and **b)** at low magnification

On the other hand, morphology of the g-CN/WO_{3-x} heterojunction after the 5th cycle demonstrated that g-CN conserved its nanosheet- and worm-like morphologies but its bundle-like structure disappeared although thin rod morphology of WO_{3-x} were present in heterojunction structure (**Figure 4.30**). Moreover, elemental mapping of g-CN/WO_{3-x} in **Figure 4.31** demonstrated that despite the 5th cycle, distribution of elements was still uniform, and W and O were present in the structure. Considering these results, it can be assumed that g-CN/WO_{3-x} has some stability issues after the 4th cycle owing to crystal structure and nonstoichiometric change of WO_{3-x}.

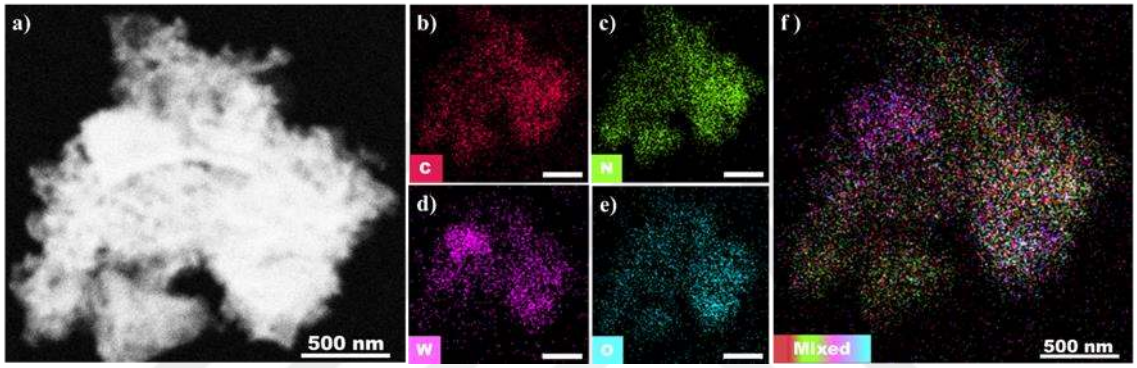

Figure 4.31: a) HAADF-STEM image and **b-f)** elemental mapping of 5-cyle used g-CN/WO_{3-x} heterojunction

Chapter 5:

CONCLUSION

In this thesis, g-CN/WO_{3-x} binary heterojunctions were successfully synthesized through a facile solvothermal method. Within the scope of photocatalyst optimization, influence of synthesis parameters including temperature, time, reaction medium and amount of WCl_6 and solvent was examined through UV-DRS, TEM and photocatalytic MO degradation as a model reaction. It was concluded that solvothermal reaction of 100 mg g-CN and 80 mg WCl_6 in the presence of 26 mL methanol at 180°C for 18 hours provides the optimum photocatalysts, denoted as g-CN/WO_{3-x}. Efficient incorporation of WO_{3-x} to g-CN was proved by XRD, XPS and ssNMR, and rod-like morphology of WO_{3-x} over g-CN containing sheet- and worm-like structures were observed. Photophysical and electrochemical characterizations unveiled that creation of heterojunction improve the charge carrier dynamics. Especially, TRPL results demonstrated that radiative recombination of e^-- h^+ was rendered severely by virtue of oxygen vacancies in WO_{3-x}. The photocatalytic activity of binary heterostructures was tested in the MO degradation and H_2O_2 generation under visible light irradiation. Whereas g-CN/WO_{3-x} degrades 98% of MO (k= 0.15816) within 25 minutes, its H_2O_2 generation was stated as 45.9 mg/L (1349.7 $\mu mol*L^{-1}$) at the end of 90 minutes which are higher than those of g-CN (51.60%; 19.46 mg/L) and WO_{3-x} (91%; 6.40 mg/L). Enhanced activity in g-CN/WO_{3-x} heterojunction photocatalyst was attributed to following reasons. i) integration of WO_{3-x} on g-CN increases the light absorption and response ability of heterojunction in the ultra-broad spectrum from UV to NIR thanks to LSPR of WO_{3-x}, ii) hot electron generation in the LSPR range since they are extra electrons to use in redox reactions, iii) non-radiative decay of hot-carriers, suppressing of photogenerated electron-hole recombination along with utilizing photothermal effect which accelerates the reactions and iv) S-scheme heterojunction formation between pristine semiconductors g-CN and WO_{3-x}, facilitating charge recombination at bands with inadequate redox potential while preserving electrons and holes, exhibiting higher redox capability. To prove S-scheme heterojunction formation, band potentials of g-CN and WO_{3-x} were determined via Mott-Schottky, Tauc plot and XPS-VB analysis, followed by work function calculations from XPS-VB to clarify electron flow pathways. Scavenger and then terephthalic acid experiments were conducted to investigate contribution of electrons, holes and ·OH radicals to reactions.

Besides, performance of photocatalysts was evaluated in H_2O_2 generation at green light to enlighten hot electron effect and the path that they follow in the binary heterojunction. After these experiments, a reaction mechanism was proposed. Finally, recyclability g-CN/WO_{3-x} photocatalyst was evaluated. It retained its high activity up to third cycle but a slight loss in activity was observed at 4^{th} cycle. At the 5^{th} cycle, a severe decrease in activity which photocatalyst lost 32.6% of its initial activity due to transformation of WO_{3-x} to WO_3.

In conclusion, g-CN/WO_{3-x} exhibited outstanding activity in both photocatalytic MO degradation and H_2O_2 generation with outperformed mostly the current literature. However, stability of WO_{3-x} at longer usage should be improved in the future works. Moreover, photothermal effect induced by hot electrons should be studied in detail. Besides, we believed that g-CN/WO_{3-x} enables production of new ideas on defective structures because they introduce many elegant features to material without using any costly equipment. As a lost word, g-CN/WO_{3-x} heterojunctions would be excellent candidate to be applied in different areas mainly photocatalysis, solar cells, photonics and biomedicine-related applications.

BIBLIOGRAPHY

[1] Forgacs, E., Cserháti, T., & Oros, G. (2004). Removal of synthetic dyes from wastewaters: A review. Environment International, 30(7), 953–971. https://doi.org/10.1016/j.envint.2004.02.001

[2] Priyadarshini, M., Das, I., Ghangrekar, M. M., & Blaney, L. (2022). Advanced oxidation processes: Performance, advantages, and scale-up of emerging technologies. Journal of Environmental Management, 316. https://doi.org/10.1016/J.JENVMAN.2022.115295

[3] Kumar, A., Choudhary, P., Chhabra, T., Kaur, H., Kumar, A., Qamar, M., & Krishnan, V. (2023). Frontier nanoarchitectonics of graphitic carbon nitride based plasmonic photocatalysts and photoelectrocatalysts for energy, environment and organic reactions. Cite This: Mater. Chem. Front, 7, 1197. https://doi.org/10.1039/d2qm01064j

[4] Hoffmann, M. R., Martin, S. T., Choi, W., & Bahnemann, D. W. (1995). Environmental Applications of Semiconductor Photocatalysis. Chemical Reviews, 95(1), 69–96. https://doi.org/10.1021/cr00033a004

[5] Guo, Y., Tong, X., & Yang, N. (2023). Photocatalytic and Electrocatalytic Generation of Hydrogen Peroxide: Principles, Catalyst Design and Performance. Nano-Micro Letters 2023 15:1, 15(1), 1–49. https://doi.org/10.1007/S40820-023-01052-2

[6] Fukuzumi, S., Yamada, Y., & Karlin, K. D. (2012). Hydrogen peroxide as a sustainable energy carrier: Electrocatalytic production of hydrogen peroxide and the fuel cell. Electrochimica Acta, 82, 493–511. https://doi.org/10.1016/J.ELECTACTA.2012.03.132

[7] Zhu, B., Cheng, B., Fan, J., Ho, W., & Yu, J. (2021). g-C_3N_4-Based 2D/2D Composite Heterojunction Photocatalyst. Small Structures, 2(12), 2100086. https://doi.org/10.1002/SSTR.202100086

[8] Li, J., Lou, Z., & Li, B. (2021). Engineering plasmonic semiconductors for enhanced photocatalysis. *Journal of Materials Chemistry A*, *9*(35), 18818-18835. https ://doi.org/10.1039/d1ta04541e

[9] Song, J., Huang, Z. F., Pan, L., Zou, J. J., Zhang, X., & Wang, L. (2015). Oxygen-Deficient Tungsten Oxide as Versatile and Efficient Hydrogenation Catalyst. *ACS Catalysis*, *5*(11), 6594–6599. https://doi.org/10.1021/acscatal.5b01522

[10] Bafana, A., Devi, S. S., & Chakrabarti, T. (2011). Azo dyes: Past, present and the future. *Environmental Reviews*, *19*(1), 350–370. https://doi.org/10.1139/a11-018

[11] Benkhaya, S., M' rabet, S., & El Harfi, A. (2020). A review on classifications, recent synthesis and applications of textile dyes. *Inorganic Chemistry Communications*, *115*(January), 107891. https://doi.org/10.1016/j.inoche.2020.107891

[12] Camargo, B. de C. V., & Morales, M. A. M. (2013). Azo Dyes : Characterization and Toxicity – A Review. *Textiles and Light Industrial Science and Technology, 2(2)*, *2*(2), 85–103.

[13] Saeed, M., Muneer, M., Haq, A. ul, & Akram, N. (2022). Photocatalysis: an effective tool for photodegradation of dyes—a review. *Environmental Science and Pollution Research*, *29*(1), 293–311. https://doi.org/10.1007/s11356-021-16389-7

[14] Hou, H., Zeng, X., & Zhang, X. (2020). Production of Hydrogen Peroxide by Photocatalytic Processes. *Angewandte Chemie International Edition*, *59*(40), 17356–17376. https://doi.org/10.1002/ANIE.201911609

[15] Chen, Z., Yao, D., Chu, C., & Mao, S. (2023). Photocatalytic H2O2 production Systems: Design strategies and environmental applications. *Chemical Engineering Journal*, *451*, 138489. https://doi.org/10.1016/J.CEJ.2022.138489

[16] Nash, D., Aklil, D., Johnson, E., Gazey, R., & Ortisi, V. (2012). Hydrogen Storage: Compressed Gas. *Comprehensive Renewable Energy*, 131–155. https://doi.org/10.1016/B978-0-08-087872-0.00413-3

[17] Wen, H., Huang, S., Meng, X., Xian, X., Zhao, J., & Roy, V. A. L. (2022). Recent progress in the design of photocatalytic H2O2 synthesis system. *Frontiers in Chemistry*, *10*, 1098209. https://doi.org/10.3389/FCHEM.2022.1098209/BIBTEX

[18] Yang, S., Verdaguer-Casadevall, A., Arnarson, L., Silvioli, L., Čolić, V., Frydendal, R., Rossmeisl, J., Chorkendorff, I., & Stephens, I. E. L. (2018). Toward the Decentralized Electrochemical Production of H2O2: A Focus on the Catalysis. *ACS Catalysis*, *8*(5), 4064–4081. https://doi.org/10.1021/ACSCATAL.8B00217

[19] Rothenberg, G. (2008). Catalysis: Concepts and Green Applications. In *Catalysis: Concepts and Green Applications*. https://doi.org/10.1002/9783527621866

[20] Helmenstine, A. M. *Catalysis Definition in Chemistry*. Retrieved March, 8 2023 from https://www.thoughtco.com/definition-of-catalyst-604402

[21] Yuryev, R., & Liese, A. (2010). Biocatalysis: The outcast. *ChemCatChem*, *2*(1), 103–107. https://doi.org/10.1002/cctc.200900126

[22] Leite, M. J. L., Marques, I. R., Proner, M. C., Araújo, P. H. H., Ambrosi, A., & Di Luccio, M. (2023). Catalytically active membranes for esterification: A review. *Chinese Journal of Chemical Engineering*, *53*, 142–154. https://doi.org/10.1016/J.CJCHE.2022.03.009

[23] Bertini, Ivano. (2009). *Inorganic and bio-inorganic chemistry*.

[24] Buzzetti, L., Crisenza, G. E. M., & Melchiorre, P. (2019). Mechanistic Studies in Photocatalysis. *Angewandte Chemie - International Edition*, *58*(12), 3730–3747. https://doi.org/10.1002/ANIE.201809984

[25] Tong, H., Ouyang, S., Bi, Y., Umezawa, N., Oshikiri, M., Ye, J., Tong, H., Bi, Y., Ye, J., Ouyang, S., Umezawa, N., & Oshikiri, M. (2012). Nano-photocatalytic Materials: Possibilities and Challenges. *Advanced Materials*, *24*(2), 229–251. https://doi.org/10.1002/ADMA.201102752

[26] Guan, X., Zong, S., & Shen, S. (2022). Homojunction photocatalysts for water splitting. *Nano Research 2022 15:12*, *15*(12), 10171–10184. https://doi.org/10.1007/S12274-022-4704-9

[27] Agrawal, D. C. (2013). Introduction to nanoscience and nanomaterials. *Introduction to Nanoscience and Nanomaterials*, 1–556. https://doi.org/10.1142/8433

[28] Rogers, B., Pennathur, S., & Adams, J. (2014). *Nanotechnology : understanding small systems* (CRC Press). https://doi.org/10.1201/9781439896716

[29] *Material Classification based on Energy Band Diagram | Electricalvoice*. (n.d.). Retrieved April 30, 2023, from https://electricalvoice.com/material-classification-based-energy-band-diagram/

[30] Callister Jr, W. D., & Rethwisch, D. G. (2020). *Callister's materials science and engineering*. John Wiley & Sons.

[31] Smallman, R. E., & Bishop, R. J. (1999). *Modern physical metallurgy and materials engineering*. Butterworth-Heinemann.

[32] *Semiconductor - Definition, Types, Examples, Uses*. (n.d.). Retrieved April 30, 2023, from https://www.priyamstudycentre.com/2021/09/semiconductor.html

[33] Wang, H., Zhang, L., Chen, Z., Hu, J., Li, S., Wang, Z., Liu, J., & Wang, X. (2014). Semiconductor heterojunction photocatalysts: design, construction, and photocatalytic performances. *Chemical Society Reviews*, *43*(15), 5234–5244. https://doi.org/10.1039/C4CS00126E

[34] Su, Q., Li, Y., Hu, R., Song, F., Liu, S., Guo, C., Zhu, S., Liu, W., & Pan, J. (2020). Heterojunction Photocatalysts Based on 2D Materials: The Role of Configuration. *Advanced Sustainable Systems*, *4*(9). https://doi.org/10.1002/ADSU.202000130

[35] Chen, X., & Zhu, H. (2011). Catalysis by Supported Gold Nanoparticles. *Comprehensive Nanoscience and Technology*, *1–5*, 1–11. https://doi.org/10.1016/B978-0-12-374396-1.00095-7

[36] Zhang, L., Zhang, J., Yu, H., Yu, J., Zhang, L., Zhang, J., Yu, H., & Yu, J. (2022). Emerging S-Scheme Photocatalyst. *Advanced Materials*, *34*(11), 2107668. https://doi.org/10.1002/ADMA.202107668

[37] Low, J., Yu, J., Jaroniec, M., Wageh, S., & Al-Ghamdi, A. A. (2017). Heterojunction Photocatalysts. Advanced Materials, 29(20). https://doi.org/10.1002/ADMA.201601694

[38] Anwer, H., Mahmood, A., Lee, J., Kim, K. H., Park, J. W., & Yip, A. C. K. (2019). Photocatalysts for degradation of dyes in industrial effluents: Opportunities and challenges. Nano Research, 12(5), 955–972. https://doi.org/10.1007/S12274-019-2287-0/METRICS

[39] Zhu, D., & Zhou, Q. (2019). Action and mechanism of semiconductor photocatalysis on degradation of organic pollutants in water treatment: A review. Environmental Nanotechnology, Monitoring and Management, 12. https://doi.org/10.1016/J.ENMM.2019.100255

[40] Ajmal, A., Majeed, I., Malik, R. N., Idriss, H., & Nadeem, M. A. (2014). Principles and mechanisms of photocatalytic dye degradation on TiO2 based photocatalysts: a comparative overview. RSC Advances, 4(70), 37003–37026. https://doi.org/10.1039/C4RA06658H

[41] Zeng, X., Liu, Y., Hu, X., & Zhang, X. (2021). Photoredox catalysis over semiconductors for light-driven hydrogen peroxide production. Green Chemistry, 23(4), 1466–1494. https://doi.org/10.1039/D0GC04236F

[42] Ong, W. J., Tan, L. L., Ng, Y. H., Yong, S. T., & Chai, S. P. (2016). Graphitic Carbon Nitride (g-C3N4)-Based Photocatalysts for Artificial Photosynthesis and Environmental Remediation: Are We a Step Closer to Achieving Sustainability? Chemical Reviews, 116(12), 7159–7329. https://doi.org/10.1021/acs.chemrev.6b00075

[43] Wang, Y., Wang, X., & Antonietti, M. (2012). Polymeric graphitic carbon nitride as a heterogeneous organocatalyst: From photochemistry to multipurpose catalysis to sustainable chemistry. Angewandte Chemie - International Edition, 51(1), 68–89. https://doi.org/10.1002/anie.201101182

[44] Cao, S., Low, J., Yu, J., & Jaroniec, M. (2015). Polymeric Photocatalysts Based on Graphitic Carbon Nitride. Advanced Materials, 27(13), 2150–2176. https://doi.org/10.1002/adma.201500033

[45] Goettmann, F., Fischer, A., Antonietti, M., & Thomas, A. (2006). Chemical synthesis of mesoporous carbon nitrides using hard templates and their use as a metal-free catalyst for Friedel-Crafts reaction of benzene. Angewandte Chemie - International Edition, 45(27), 4467–4471. https://doi.org/10.1002/ANIE.200600412

[46] Wang, X., Blechert, S., & Antonietti, M. (2012). Polymeric graphitic carbon nitride for heterogeneous photocatalysis. ACS Catalysis, 2(8), 1596–1606. https://doi.org/10.1021/cs300240x

[47] Zhang, L., Wang, H., Liu, J., Zhang, Q., & Yan, · Hui. (2020). Nonstoichiometric tungsten oxide: structure, synthesis, and applications. Journal of Materials Science: Materials in Electronics, 31, 861–873. https://doi.org/10.1007/s10854-019-02596-z

[48] Zheng, H., Ou, J. Z., Strano, M. S., Kaner, R. B., Mitchell, A., & Kalantar-Zadeh, K. (2011). Nanostructured tungsten oxide - Properties, synthesis, and applications. Advanced Functional Materials, 21(12), 2175–2196. https://doi.org/10.1002/ADFM.201002477

[49] Lundberg, M., Sundberg, M., & Magnéli, A. (1982). The “pentagonal column” as a building unit in crystal and defect structures of some groups of transition metal compounds. Journal of Solid State Chemistry, 44(1), 32–40. https://doi.org/10.1016/0022-4596(82)90398-X

[50] Zhang, Z., Huang, J., Fang, Y., Zhang, M., Liu, K., & Dong, B. (2017). A Nonmetal Plasmonic Z-Scheme Photocatalyst with UV- to NIR-Driven Photocatalytic Protons Reduction. Advanced Materials, 29(18). https://doi.org/10.1002/ADMA.201606688

[51] Kim, M., Lin, M., Son, J., Xu, H., & Nam, J. M. (2017). Hot-Electron-Mediated Photochemical Reactions: Principles, Recent Advances, and Challenges. Advanced Optical Materials, 5(15), 1700004. https://doi.org/10.1002/ADOM.201700004

[52] Mayer, K. M., & Hafner, J. H. (2011). Localized surface plasmon resonance sensors. Chemical Reviews, 111(6), 3828–3857. https://doi.org/10.1021/cr100313v

[53] Masson, J. F. (2020). Portable and field-deployed surface plasmon resonance and plasmonic sensors. Analyst, 145(11), 3776–3800. https://doi.org/10.1039/D0AN00316F

[54] Fu, J., Yu, J., Jiang, C., & Cheng, B. (2018). g-C3N4-Based Heterostructured Photocatalysts. Advanced Energy Materials, 8(3), 1701503. https://doi.org/10.1002/AENM.201701503

[55] Zhang, B., Hu, X., Liu, E., & Fan, J. (2021). Novel S-scheme 2D/2D BiOBr/g-C3N4 heterojunctions with enhanced photocatalytic activity. Chinese Journal of Catalysis, 42(9), 1519–1529. https://doi.org/10.1016/S1872-2067(20)63765-2

[56] Ahmad, I., Shukrullah, S., Naz, M. Y., & Bhatti, H. N. (2023). Dual S-scheme ZnO–g-C3N4–CuO heterosystem: a potential photocatalyst for H2 evolution and wastewater treatment. Reaction Chemistry & Engineering. https://doi.org/10.1039/D2RE00576J

[57] Ahmad, N., Kuo, C. F. J., & Mustaqeem, M. (2022). Synthesis of novel CuNb2O6/g-C3N4 binary photocatalyst towards efficient visible light reduction of Cr (VI) and dyes degradation for environmental remediation. Chemosphere, 298, 134153. https://doi.org/10.1016/J.CHEMOSPHERE.2022.134153

[58] Eroglu, Z., Ozer, M. S., & Metin, O. (2023). Black Phosphorus Quantum Dots/Carbon Nitride-Reduced Graphene Oxide Ternary Heterojunction as a Multifunctional Metal-Free Photocatalyst for Photooxidation Reactions. ACS Sustainable Chemistry and Engineering, 11(19), 7560–7572. https://doi.org/10.1021/acssuschemeng.3c01055

[59] Zhao, X., You, Y., Huang, S., Wu, Y., Ma, Y., Zhang, G., & Zhang, Z. (2020). Z-scheme photocatalytic production of hydrogen peroxide over Bi4O5Br2/g-C3N4 heterostructure under visible light. Applied Catalysis B: Environmental, 278, 119251. https://doi.org/10.1016/J.APCATB.2020.119251

[60] Wang, A., Liang, H., Chen, F., Tian, X., Yin, S., Jing, S., & Tsiakaras, P. (2022). Facile synthesis of C3N4/NiIn2S4 heterostructure with novel solar steam evaporation efficiency and photocatalytic H2O2 production performance. Applied Catalysis B: Environmental, 310, 121336. https://doi.org/10.1016/J.APCATB.2022.121336

[61] Liu, B., Bie, C., Zhang, Y., Wang, L., Li, Y., & Yu, J. (2021). Hierarchically porous zno/g-c3n4s-scheme heterojunction photocatalyst for efficient H2O2production. Langmuir, 37(48), 14114–14124. https://doi.org/10.1021/acs.langmuir.1c02360

[62] Wang, W., Song, Q., Luo, Q., Li, L., Huo, X., Chen, S., Li, J., Li, Y., Shi, S., Yuan, Y., Du, X., Zhang, K., & Wang, N. (2023). Photothermal-enabled single-atom catalysts for high-efficiency hydrogen peroxide photosynthesis from natural seawater. Nature Communications 2023 14:1, 14(1), 1–10. https://doi.org/10.1038/s41467-023-38211-3

[63] Chen, H., Xing, Y., Liu, S., Liang, Y., Fu, J., Wang, L., & Wang, W. (2023). Mechanistic insights into efficient photocatalytic H2O2 production of 2D/2D g-C3N4/In2S3 photocatalyst by tracking charge flow direction. Chemical Engineering Journal, 462, 142038. https://doi.org/10.1016/J.CEJ.2023.142038

[64] Das, K. K., Mansingh, S., Mohanty, R., Sahoo, D. P., Priyadarshini, N., & Parida, K. (2023). 0D-2D Fe2O3/Boron-Doped g-C3N4 S-Scheme Exciton Engineering for Photocatalytic H2O2 Production and Photo-Fenton Recalcitrant-Pollutant Detoxification: Kinetics, Influencing Factors, and Mechanism. Journal of Physical Chemistry C, 127(1), 22–40. https://doi.org/10.1021/ACS.JPCC.2C06369

[65] Dutta, V., Sharma, S., Raizada, P., Thakur, V. K., Khan, A. A. P., Saini, V., Asiri, A. M., & Singh, P. (2021). An overview on WO3 based photocatalyst for environmental remediation. Journal of Environmental Chemical Engineering, 9(1), 105018. https://doi.org/10.1016/J.JECE.2020.105018

[66] Theerthagiri, J., Chandrasekaran, S., Salla, S., Elakkiya, V., Senthil, R. A., Nithyadharseni, P., Maiyalagan, T., Micheal, K., Ayeshamariam, A., Valan Arasu, M., Al-Dhabi, A., & Kim, H.-S. (2018). Recent developments of metal oxide based

heterostructures for photocatalytic applications towards environmental remediation. https://doi.org/10.1016/j.jssc.2018.08.006

[67] Yan, M., Li, G., Guo, C., Guo, W., Ding, D., Zhang, S., & Liu, S. (2016). WO3−x sensitized TiO2 spheres with full-spectrum-driven photocatalytic activities from UV to near infrared. Nanoscale, 8(41), 17828–17835. https://doi.org/10.1039/C6NR06767K

[68] Chen, X., Guo, R. tang, Pan, W. Guo, Yuan, Y., Hu, X., Bi, Z. Xu, & Wang, J. (2022). A novel double S-scheme photocatalyst Bi7O9I3/Cd0.5Zn0.5S QDs/WO3−x with efficient full-spectrum-induced phenol photodegradation. Applied Catalysis B: Environmental, 318, 121839. https://doi.org/10.1016/J.APCATB.2022.121839

[69] Yang, Z., Xia, X., Yang, W., wang, L., & Liu, Y. (2021). Photothermal effect and continuous hot electrons injection synergistically induced enhanced molecular oxygen activation for efficient selective oxidation of benzyl alcohol over plasmonic W18O49/ZnIn2S4 photocatalyst. Applied Catalysis B: Environmental, 299, 120675. https://doi.org/10.1016/J.APCATB.2021.120675

[70] Guo, M., Xing, Z., Zhao, T., Li, Z., Yang, S., & Zhou, W. (2019). WS2 quantum dots/MoS2@WO3-x core-shell hierarchical dual Z-scheme tandem heterojunctions with wide-spectrum response and enhanced photocatalytic performance. Applied Catalysis B: Enviro*nmental*, *257*, 117913. https://doi.org/10.1016/J.APCATB.2019.117913

[71] Huang, Y., Xu, H., Luo, D., Zhao, Y., Fang, Y., Guo, Q., Wei, Y., Fan, L., & Wu, J. (2019). Facile synthesis of three-dimensional WO3-x/Bi/BiOCl hierarchical heterostructures with broad spectrum driven photocatalytic activity. *Journal of Alloys and Compounds*, *806*, 418–427. https://doi.org/10.1016/J.JALLCOM.2019.07.137

[72] Jiang, H., Wang, L., Yu, X., Sun, L., Li, J., Yang, J., & Liu, Q. (2023). Precise regulation of built-in electric field over NH2-MIL-125-Ti/WO3-x S-scheme heterojunction for achieving simultaneous formation of CO and H2O2 from CO2 and H2O. *Chemical Engineering Journal*, *466*, 143129. https://doi.org/10.1016/J.CEJ.2023.143129

[73] Zhang, F., Huang, L., Ding, P., Wang, C., Wang, Q., Wang, H., Li, Y., Xu, H., & Li, H. (2019). One-step oxygen vacancy engineering of WO3-x/2D g-C3N4 heterostructure: Triple effects for sustaining photoactivity. *Journal of Alloys and Compounds*, *795*, 426–435. https://doi.org/10.1016/J.JALLCOM.2019.04.297

[74] Shang, Y., Wang, C., Yan, C., Jing, F., Roostaeinia, M., Wang, Y., Chen, G., & Lv, C. (2023). An efficient and multifunctional S-scheme heterojunction photocatalyst constructed by tungsten oxide and graphitic carbon nitride: Design and mechanism study. *Journal of Colloid and Interface Science*, *634*, 195–208. https://doi.org/10.1016/J.JCIS.2022.12.039

[75] Shao, T., Chang, Y., Li, Z., Song, Y., Jin, D., Gao, J., Sun, L., & Hou, J. (2023). A chemically bonded and plasmonic Z-scheme junction for high-performance artificial photosynthesis of hydrogen peroxide. *Journal of Materials Chemistry A*, *11*(3), 1199–1207. https://doi.org/10.1039/D2TA09122D

[76] Li, X., Kang, B., Dong, F., Zhang, Z., Luo, X., Han, L., Huang, J., Feng, Z., Chen, Z., Xu, J., Peng, B., & Wang, Z. L. (2021). Enhanced photocatalytic degradation and H2/H2O2 production performance of S-pCN/WO2.72 S-scheme heterojunction with appropriate surface oxygen vacancies. *Nano Energy*, *81*, 105671. https://doi.org/10.1016/J.NANOEN.2020.105671

[77] He, Y., Huang, J., Wang, B., & Qu, Y. (2023). Construction of Z-scheme heterojunction C3N4/N-CQDs@W18O49 for full-spectrum photocatalytic organic pollutant degradation. *Applied Surface Science*, *610*, 155255. https://doi.org/10.1016/J.APSUSC.2022.155255

[78] Zhang, L., Liu, L., Zhang, X., Ge, C., & Liao, J. (2022). WO3−x /S-Doped g-C3N4 Step-Scheme Heterojunction for High-Efficiency and Stable Vis–NIR Photocatalytic Removal of Pharmaceuticals and Personal Care Products. *Advanced Energy and Sustainability Research*, *3*(12), 2200138. https://doi.org/10.1002/AESR.202200138

[79] Hong, I., Chen, Y. A., Hsu, Y. J., & Yong, K. (2021). Triple-channel charge transfer over w18o49/au/g-c3n4 z-scheme photocatalysts for achieving broad-spectrum solar

hydrogen production. *ACS Applied Materials and Interfaces*, *13*(44), 52670–52680. https://doi.org/10.1021/ACSAMI.1C15883/SUPPL_FILE/AM1C15883_SI_001.PDF

[80] Li, X., Ye, F., Zhang, H., Ahmad, M., Zeng, Z., Wang, S., Wang, S., Gao, D., & Zhang, Q. (2023). Ternary rGO decorated W18O49 @g-C3N4 composite as a full-spectrum-responded Z-scheme photocatalyst for efficient photocatalytic H2O2 production and water disinfection. *Journal of Environmental Chemical Engineering*, *11*(4), 110329. https://doi.org/10.1016/J.JECE.2023.110329

[81] Eroglu, Z., Ozer, M. S., Kubanaliev, T., Kilic, H., & Metin, Ö. (2022). Synergism between few-layer black phosphorus and graphitic carbon nitride enhances the photoredox C–H arylation under visible light irradiation. *Catalysis Science & Technology*, *12*(17), 5379–5389. https://doi.org/10.1039/D2CY01090A

[82] Zhang, G., Guan, W., Shen, H., Zhang, X., Fan, W., Lu, C., Bai, H., Xiao, L., Gu, W., & Shi, W. (2014). Organic additives-free hydrothermal synthesis and visible-light-driven photodegradation of tetracycline of WO3 nanosheets. *Industrial and Engineering Chemistry Research*, *53*(13), 5443–5450. https://doi.org/10.1021/IE4036687

[83] Wang, M., Qiu, S., Yang, H., Huang, Y., Dai, L., Zhang, B., & Zou, J. (2021). Spectrophotometric determination of hydrogen peroxide in water with peroxidase-catalyzed oxidation of potassium iodide and its applications to appropriate surface oxygen vacancies. *Nano Energy*, *81*, 105671. https://doi.org/10.1016/J.NANOEN.2020.105671

[84] Altan, O., Altintas, E., Alemdar, S., & Metin, Ö. (2022). The rational design of a graphitic carbon nitride-based dual S-scheme heterojunction with energy storage ability as a day/night photocatalyst for formic acid dehydrogenation. *Chemical Engineering Journal*, *441*, 136047. https://doi.org/10.1016/J.CEJ.2022.136047

[85] Jones, R. R., Hooper, D. C., Zhang, L., Wolverson, D., & Valev, V. K. (2019). Raman Techniques: Fundamentals and Frontiers. *Nanoscale Research Letters 2019 14:1*, *14*(1), 1–34. https://doi.org/10.1186/S11671-019-3039-2

[86] Smith, E., & Dent, G. (2019). Modern raman spectroscopy: A practical approach. In *Modern Raman Spectroscopy: A Practical Approach*. https://doi.org/10.1002/0470011831

[87] Holder, C. F., & Schaak, R. E. (2019). Tutorial on Powder X-ray Diffraction for Characterizing Nanoscale Materials. *ACS Nano*, *13*(7), 7359–7365. https://doi.org/10.1021/ACSNANO.9B05157

[88] Epp, J. (2016). X-ray diffraction (XRD) techniques for materials characterization. *Materials Characterization Using Nondestructive Evaluation (NDE) Methods*, 81–124. https://doi.org/10.1016/B978-0-08-100040-3.00004-3

[89] Raja, P. B., Munusamy, K. R., Perumal, V., & Ibrahim, M. N. M. (2022). Characterization of nanomaterial used in nanobioremediation. *Nano-Bioremediation: Fundamentals and Applications*, 57–83. https://doi.org/10.1016/B978-0-12-823962-9.00037-4

[90] Razeghi, M. (2009). Semiconductor Characterization Techniques. *Fundamentals of Solid State Engineering*, 1–29. https://doi.org/10.1007/978-0-387-92168-6_16

[91] Henini, M. (2000). Scanning electron microscopy: an introduction. *III-Vs Review*, *13*(4), 40–44. https://doi.org/10.1016/S0961-1290(00)80006-X

[92] Zhou, W., Apkarian, R., Wang, Z. L., & Joy, D. (2007). Fundamentals of scanning electron microscopy (SEM). *Scanning Microscopy for Nanotechnology: Techniques and Applications*, 1–40. https://doi.org/10.1007/978-0-387-39620-0_1/COVER

[93] Ezzahmouly, M., Elmoutaouakkil, A., Ed-Dhahraouy, M., Khallok, H., Elouahli, A., Mazurier, A., ElAlbani, A., & Hatim, Z. (2019). Micro-computed tomographic and SEM study of porous bioceramics using an adaptive method based on the mathematical

[94] Hernández-Ramírez, A., & Medina-Ramírez, I. (2015). Photocatalytic semiconductors: Synthesis, characterization, and environmental applications. Photocatalytic Semiconductors: Synthesis, Characterization, and Environmental Applications, 1–289. https://doi.org/10.1007/978-3-319-10999-2

[95] Inkson, B. J. (2016). Scanning electron microscopy (SEM) and transmission electron microscopy (TEM) for materials characterization. Materials Characterization Using Nondestructive Evaluation (NDE) Methods, 17–43. https://doi.org/10.1016/B978-0-08-100040-3.00002-X

[96] Basic operations of Transmission Electron Microscope (Imaging and Diffraction Pattern). (n.d.). Retrieved December 7, 2023, from https://emb-iitk.vlabs.ac.in/exp/transmission-electron-microscope/theory.html

[97] Scimeca, M., Bischetti, S., Lamsira, H. K., Bonfiglio, R., & Bonanno, E. (2018). Energy Dispersive X-ray (EDX) microanalysis: A powerful tool in biomedical research and diagnosis. European Journal of Histochemistry : EJH, 62(1), 89–99. https://doi.org/10.4081/EJH.2018.2841

[98] Fitzgerald, A. G. (Ed.). (2017). Quantitative microbeam analysis. Routledge.

[99] Stevie, F. A., & Donley, C. L. (2020). Introduction to x-ray photoelectron spectroscopy. Journal of Vacuum Science & Technology A, 38(6), 063204. https://doi.org/10.1116/6.0000412/1024200

[100] Handbook of Applied Solid State Spectroscopy. (2006). Handbook of Applied Solid State Spectroscopy. https://doi.org/10.1007/0-387-37590-2

[101] Fadley, C. S. (2010). X-ray photoelectron spectroscopy: Progress and perspectives. Journal of Electron Spectroscopy and Related Phenomena, 178–179(C), 2–32. https://doi.org/10.1016/J.ELSPEC.2010.01.006

[102] Lemon, C. E. (2012). Atmospheric Corrosion of Silver Investigated by X-ray Photoelectron Spectroscopy. https://doi.org/10.1520/B0117-11

[103] Foerch, R., Beamson, G., & Briggs, D. (1991). XPS valence band analysis of plasma–treated polymers. Surface and Interface Analysis, 17(12), 842–846. https://doi.org/10.1002/SIA.740171204

[104] Trasa'tti, S. (1986). The absolute electrode potential: An explanatory note (Recommendations 1986). Pure and Applied Chemistry, 58(7), 955–966. https://doi.org/10.1351/PAC198658070955

[105] Zhong, H., Pan, F., Yue, S., Qin, C., Hadjiev, V., Tian, F., Liu, X., Lin, F., Wang, Z., & Bao, J. (2023). Idealizing Tauc Plot for Accurate Bandgap Determination of Semiconductor with Ultraviolet-Visible Spectroscopy: A Case Study for Cubic Boron Arsenide. Journal of Physical Chemistry Letters, 14(29), 6702–6708. https://doi.org/10.1021/ACS.JPCLETT.3C01416

[106] Makuła, P., Pacia, M., & Macyk, W. (2018). How To Correctly Determine the Band Gap Energy of Modified Semiconductor Photocatalysts Based on UV-Vis Spectra. Journal of Physical Chemistry Letters, 9(23), 6814–6817. https://doi.org/10.1021/ACS.JPCLETT.8B02892

[107] Krishna, R., Yadaw, P. K., Dubey, V., & Kumar Swamy, N. (2022). Properties and characterization of rare-earth-activated phosphors. Rare-Earth-Activated Phosphors: Chemistry and Applications, 43–58. https://doi.org/10.1016/B978-0-323-89856-0.00014-6

[108] Nevin, A., Cesaratto, A., Bellei, S., D'Andrea, C., Toniolo, L., Valentini, G., & Comelli, D. (2014). Time-Resolved Photoluminescence Spectroscopy and Imaging: New Approaches to the Analysis of Cultural Heritage and Its Degradation. Sensors, 14(4), 6338. https://doi.org/10.3390/S140406338

[109] Cannas, M., & Vaccaro, L. (2021). Time-Resolved Photoluminescence. Spectroscopy for Materials Characterization, 35–63. https://doi.org/10.1002/9781119698029.CH2

[110] Metzger, W. K., Ahrenkiel, R. K., Dippo, P., Geisz, J., Wanlass, M. W., & Kurtz, S. (2005). Time-resolved photoluminescence and photovoltaics (No. NREL/CP-520-37028). National Renewable Energy Lab.(NREL), Golden, CO (United States).

[111] Time Resolved Photoluminescence Spectroscopy (TRPL). (n.d.). Retrieved September 22, 2023, from https://ufd.kaust.edu.sa/detail/facilities/time-resolved-photoluminescence-spectroscopy-(trpl)

[112] Sermin Ozer, M., Eroglu, Z., Yalin, A. S., Kılıç, M., Rothlisberger, U., & Metin, O. (2021). Bismuthene as a versatile photocatalyst operating under variable conditions

for the photoredox C-H bond functionalization. https://doi.org/10.1016/j.apcatb.2021.120957

[113] Magar, H. S., Hassan, R. Y. A., & Mulchandani, A. (2021). Electrochemical Impedance Spectroscopy (EIS): Principles, Construction, and Biosensing Applications. Sensors (Basel, Switzerland), 21(19). https://doi.org/10.3390/S21196578

[114] Lazanas, A. C., & Prodromidis, M. I. (2023). Electrochemical Impedance Spectroscopy─A Tutorial. ACS Measurement Science Au, 3(3), 162–193. https://doi.org/10.1021/ACSMEASURESCIAU.2C00070/ASSET/IMAGES/LARGE/TG2C00070_0032.JPEG

[115] Palomares, E., Montcada, N. F., Méndez, M., Jiménez-López, J., Yang, W., & Boschloo, G. (2020). Photovoltage/photocurrent transient techniques. Characterization Techniques for Perovskite Solar Cell Materials, 161–180. https://doi.org/10.1016/B978-0-12-814727-6.00007-4

[116] McNeill, C. R., Hwang, I., & Greenham, N. C. (2009). Photocurrent transients in all-polymer solar cells: Trapping and detrapping effects. Journal of Applied Physics, 106(2), 24507. https://doi.org/10.1063/1.3177337/393630

[117] Radecka, M., Rekas, M., Trenczek-Zajac, A., & Zakrzewska, K. (2008). Importance of the band gap energy and flat band potential for application of modified TiO2 photoanodes in water photolysis. Journal of Power Sources, 181, 46–55. https://doi.org/10.1016/j.jpowsour.2007.10.082

[118] Lee, S. F., Jimenez-Relinque, E., Martinez, I., & Castellote, M. (2023). Effects of Mott–Schottky Frequency Selection and Other Controlling Factors on Flat-Band Potential and Band-Edge Position Determination of TiO2. Catalysts, 13(6), 1000. https://doi.org/10.3390/CATAL13061000/S1

[119] Lee, S. F., Jimenez-Relinque, E., Martinez, I., & Castellote, M. (2022). Photoelectrochemical global approach to the behaviour of nanostructured anatase under different irradiation conditions. Catalysis Today, 397–399, 286–295. https://doi.org/10.1016/J.CATTOD.2021.09.006

[120] Gelderman, K., Lee, L., & Donne, S. W. (2007). Flat-band potential of a semiconductor: Using the Mott-Schottky equation. Journal of Chemical Education, 84(4), 685–688. https://doi.org/10.1021/ED084P685

[121] Bott, A. W. (1998). Electrochemistry of semiconductors. Current Separations, 17, 87–92. http://www.currentseparations.com/issues/17-3/cs-17-3d

[122] Zhang, L., Liu, L., Zhang, X., Ge, C., & Liao, J. (2022). WO3−x /S-Doped g-C3N4 Step-Scheme Heterojunction for High-Efficiency and Stable Vis–NIR Photocatalytic Removal of Pharmaceuticals and Personal Care Products. Advanced Energy and Sustainability Research, 3(12), 2200138. https://doi.org/10.1002/AESR.202200138

[123] Shang, Y., Wang, C., Yan, C., Jing, F., Roostaeinia, M., Wang, Y., Chen, G., & Lv, C. (2023). An efficient and multifunctional S-scheme heterojunction photocatalyst constructed by tungsten oxide and graphitic carbon nitride: Design and mechanism study. Journal of Colloid and Interface Science, 634, 195–208. https://doi.org/10.1016/J.JCIS.2022.12.039

[124] Li, J., Chen, G., Yan, J., Huang, B., Cheng, H., Lou, Z., & Li, B. (2020). Solar-driven plasmonic tungsten oxides as catalyst enhancing ethanol dehydration for highly selective ethylene production. Applied Catalysis B: Environmental, 264, 118517. https://doi.org/10.1016/J.APCATB.2019.118517

[125] Ayyappan, S., & Rao, C. N. R. (1995). A simple method of hydrogen insertion in transition metal oxides to obtain bronzes. Materials research bulletin, 30(8), 947-951.

[126] Guo, C., Yin, S., Yan, M., Kobayashi, M., Kakihana, M., & Sato, T. (2012). Morphology-controlled synthesis of W 18O 49 nanostructures and their near-infrared absorption properties. Inorganic Chemistry, 51(8), 4763–4771. https://doi.org/10.1021/IC300049J

[127] Wang, Y., Wang, X., Xu, Y., Chen, T., Liu, M., Niu, F., Wei, S., & Liu, J. (2017). Simultaneous Synthesis of WO3−x Quantum Dots and Bundle-Like Nanowires Using a One-Pot Template-Free Solvothermal Strategy and Their Versatile Applications. Small, 13(13), 1603689. https://doi.org/10.1002/SMLL.201603689

[128] Joshi, D. P., Pant, G., Arora, N., & Nainwal, S. (2017). Effect of solvents on morphology, magnetic and dielectric properties of (α-Fe2O3@SiO2) core-shell nanoparticles. Heliyon, 3(2), e00253. https://doi.org/10.1016/J.HELIYON.2017.E00253

[129] Dridi, M., Jaouadi, A., Colas, F., & Compère, C. (2021). Theoretical Study of High Near-Field Enhancement Associated with the Lasing Action in Strongly Coupled Plasmonic Nanocavity Arrays. Journal of Physical Chemistry C, 125(1), 749–756. https://doi.org/10.1021/ACS.JPCC.0C08669

[130] Han, C., Gómez, D. E., Xiao, Q., & Xu, J. (2021). Near-field enhancement by plasmonic antennas for photocatalytic Suzuki-Miyaura cross-coupling reactions. Journal of Catalysis, 397, 205–211. https://doi.org/10.1016/J.JCAT.2021.03.020

[131] Kim, J., Agrawal, A., Krieg, F., Bergerud, A., & Milliron, D. J. (2016). The Interplay of Shape and Crystalline Anisotropies in Plasmonic Semiconductor Nanocrystals. Nano Letters, 16(6), 3879–3884. https://doi.org/10.1021/ACS.NANOLETT.6B01390

[132] Wang, S., Xu, H., Hao, T., Wang, P., Zhang, X., Zhang, H., Xue, J., Zhao, J., & Li, Y. (2021). In situ XRD and operando spectra-electrochemical investigation of tetragonal WO3-x nanowire networks for electrochromic supercapacitors. NPG Asia Materials 2021 13:1, 13(1), 1–11. https://doi.org/10.1038/s41427-021-00319-7

[133] Lu, D. Y., Chen, J., Zhou, J., Deng, S. Z., Xu, N. S., & Xu, J. B. (2007). Raman spectroscopic study of oxidation and phase transition in W 18O49 nanowires. Journal of Raman Spectroscopy, 38(2), 176–180. https://doi.org/10.1002/JRS.1620

[134] Frey, G. L., Rothschild, A., Sloan, J., Rosentsveig, R., Popovitz-Biro, R., & Tenne, R. (2001). Investigations of Nonstoichiometric Tungsten Oxide Nanoparticles. Journal of Solid State Chemistry, 162(2), 300–314. https://doi.org/10.1006/JSSC.2001.9319

[135] Gao, Y., & Yin, P. (2017). Origin of asymmetric broadening of Raman peak profiles in Si nanocrystals. Scientific Reports 2017 7:1, 7(1), 1–4. https://doi.org/10.1038/srep43602

[136] Gao, J., Zhou, Y., Li, Z., Yan, S., Wang, N., & Zou, Z. (2012). High-yield synthesis of millimetre-long, semiconducting carbon nitride nanotubes with intense photoluminescence emission and reproducible photoconductivity. *Nanoscale*, *4*(12), 3687–3692. https://doi.org/10.1039/C2NR30777D

[137] Fina, F., Callear, S. K., Carins, G. M., & Irvine, J. T. S. (2015). Structural investigation of graphitic carbon nitride via XRD and neutron diffraction. *Chemistry of Materials*, *27*(7), 2612–2618 . https://doi.org/10.1021/ACS.CHEMMATER.5B00411

[138] Zhu, C., Zheng, S., Cao, T., Lin, C., & Xie, Z. (2018). Surface oxygen vacancies induced peroxidase-like activity for W18O49 nanospheres and their application in degradation of methylene blue. *Journal of Nanoparticle Research*, *20*(7), 1–10. https://doi.org/10.1007/S11051-018-4271-X

[139] Zhang, L., Jin, Z., Lu, H., Lin, T., Ruan, S., Zhao, X. S., & Zeng, Y. J. (2018). Improving the Visible-Light Photocatalytic Activity of Graphitic Carbon Nitride by Carbon Black Doping. ACS Omega, 3(11), 15009–15017. https://doi.org/10.1021/ACSOMEGA.8B01933

[140] Sun, N., Liang, Y., Ma, X., & Chen, F. (2017). Reduced Oxygenated g-C3N4 with Abundant Nitrogen Vacancies for Visible-Light Photocatalytic Applications. Chemistry – A European Journal, 23(61), 15466–15473. https://doi.org/10.1002/CHEM.201703168

[141] Aksoy, M., & Metin, Ö. (2020). Pt Nanoparticles Supported on Mesoporous Graphitic Carbon Nitride as Catalysts for Hydrolytic Dehydrogenation of Ammonia Borane. *ACS Applied Nano Materials*, *3*(7), 6836–6846. https://doi.org/10.1021/ACSANM.0C01208/ASSET/IMAGES/LARGE/AN0C01208_0010.JPEG

[142] Aksoy, M., Eken Korkut, S., & Metin, Ö. (2022). AuPt alloy nanoparticles supported on graphitic carbon nitride: In situ synthesis and superb catalytic performance in the light-assisted hydrolytic dehydrogenation of ammonia borane.

Applied Surface Science, *602*, 154286. https://doi.org/10.1016/J.APSUSC.2022.154286

[143] Li, J., Tian, C., Zhao, H., Mei, J., Zhang, J., & Yang, S. (2019). Controllable fabrication of a red phosphorus modified g-C3N4 photocatalyst with strong interfacial binding for the efficient removal of organic pollutants. *Journal of Alloys and Compounds*, *810*, 151885. https://doi.org/10.1016/J.JALLCOM.2019.151885

[144] Laws, D. D., Bitter, H. M. L., & Jerschow, A. (2002). Solid-state NMR spectroscopic methods in chemistry. *Angewandte Chemie International Edition*, *41*(17), 3096-3129.

[145] Wang, R., Xu, B. B., Wang, J., Wang, X. L., & Yao, Y. F. (2021). Selective hydrogen–deuterium exchange in graphitic carbon nitrides: probing the active sites for photocatalytic water splitting by solid-state NMR. *Journal of Materials Chemistry A*, *9*(7), 3985–3994. https://doi.org/10.1039/D0TA10148F

[146] Kubanaliev, T., Eroglu, Z., Ozer, M. S., & Metin, Ö. (2023). The effect of N-vacancy on the photocatalytic activity of graphitic carbon nitride in the oxidative Mannich reaction. *Catalysis Science & Technology*, *13*(8), 2317-2329. https://doi.org/10.1039/D3CY00046J

[147] Xia, B., He, B., Zhang, J., Li, L., Zhang, Y., Yu, J., Ran, J., & Qiao, S. Z. (2022). TiO2/FePS3 S-Scheme Heterojunction for Greatly Raised Photocatalytic Hydrogen Evolution. Advanced Energy Materials, 12(46). https://doi.org/10.1002/AENM.202201449

[148] Lv, Z., Guo, Z., Li, D., Jiang, H., Wang, F., Fan, L., Wei, M., & Yang, L. (2022). Perovskite/Hole Transport Layer Interfacial Engineering with Substoichiometric Tungsten Oxide Rich in Oxygen Vacancies to Boost the Photovoltaic Performance of Perovskite Solar Cells. *Solar RRL*, *6*(12). https://doi.org/10.1002/SOLR.202200720

[149] Zhu, E., Zhao, Y., Dai, Y., Wang, Q., Dong, Y., Chen, Q., & Li, Y. (2020). Heterojunction-Type Photocatalytic System Based on Inorganic Halide Perovskite CsPbBr3†. *Chinese Journal of Chemistry*, *38*(12), 1718–1722. https://doi.org/10.1002/CJOC.202000333

[150] Hong, I., Chen, Y. A., Hsu, Y. J., & Yong, K. (2021). Triple-channel charge transfer over w18o49/au/g-c3n4 z-scheme photocatalysts for achieving broad-spectrum solar hydrogen production. *ACS Applied Materials and Interfaces*, *13*(44), 52670–52680.

[151] Chiu, K. P. (2023). The influence of a trap state on the photoluminescence decay times under single pulse excitation. *Optical and Quantum Electronics*, *55*(2), 1–11. https://doi.org/10.1007/S11082-022-04433-W/FIGURES/5

[152] Fassl, P., Zakharko, Y., Falk, L. M., Goetz, K. P., Paulus, F., Taylor, A. D., Zaumseil, J., & Vaynzof, Y. (2019). Effect of density of surface defects on photoluminescence properties in MAPbI3 perovskite films. *Journal of Materials* Chemistry C, 7(18), 5285–5292. https://doi.org/10.1039/C8TC05998E

[153] Peán, E. V., Dimitrov, S., De Castro, C. S., & Davies, M. L. (2020). Interpreting time-resolved photoluminescence of perovskite materials. Physical Chemistry Chemical Physics, 22(48), 28345–28358. https://doi.org/10.1039/D0CP04950F

[154] Jiang, Y., Li, Y., Liu, F., Wang, W., Su, W., Liu, W., Liu, S., Zhang, W., Hou, J., Xu, S., Yi, Y., & Zhu, X. (2023). Suppressing electron-phonon coupling in organic photovoltaics for high-efficiency power conversion. Nature Communications 2023 14:1, 14(1), 1–12. https://doi.org/10.1038/s41467-023-40806-9

[155] Ge, H., Kuwahara, Y., & Yamashita, H. (2022). Development of defective molybdenum oxides for photocatalysis, thermal catalysis, and photothermal catalysis. Chemical Communications, 58(61), 8466–8479. https://doi.org/10.1039/D2CC02658A

[156] Eroglu, Z., & Metin, O. (2023). Internal Interactions within the Complex Type-II Heterojunction of a Graphitic Carbon Nitride/Black Phosphorus Hybrid Decorated with Graphene Quantum Dots: Implications for Photooxidation Performance. ACS Applied Nano Materials, 6(9), 7960–7974. https://doi.org/10.1021/ACSANM.3C01187

[157] Zhao, X., Zhang, X., Han, D., & Niu, L. (2020). Ag supported Z-scheme WO2.9/g-C3N4 composite photocatalyst for photocatalytic degradation under visible light.

Applied Surface Science, 501, 144258. https://doi.org/10.1016/J.APSUSC.2019.144258

[158] Shen, L., Xing, Z., Zou, J., Li, Z., Wu, X., Zhang, Y., Zhu, Q., Yang, S., & Zhou, W. (2017). Black TiO2 nanobelts/g-C3N4 nanosheets Laminated Heterojunctions with Efficient Visible-Light-Driven Photocatalytic Performance. *Scientific Reports 2017 7:1*, *7*(1), 1–11. https://doi.org/10.1038/srep41978

[159] Tran Huu, H., Thi, M. D. N., Nguyen, V. P., Thi, L. N., Phan, T. T. T., Hoang, Q. D., Luc, H. H., Kim, S. J., & Vo, V. (2021). One-pot synthesis of S-scheme MoS2/g-C3N4 heterojunction as effective visible light photocatalyst. Scientific Reports 2021 11:1, 11(1), 1–12. https://doi.org/10.1038/s41598-021-94129-0

[160] Nagappagari, L. R., Patil, S. S., Lee, J., Park, E., Yu, Y. T., & Lee, K. (2022). Upgraded charge transport in g-C3N4 nanosheets by boron doping and their heterojunction with 3D CdIn2S4 for efficient photodegradation of azo dye. *Materials Today Chemistry*, *24*, 100857. https://doi.org/10.1016/J.MTCHEM.2022.100857

[161] Prabhakar, R., Morokuma, K., Hill, C. L., & Musaev, D. G. (2006). Insights into the mechanism of selective olefin epoxidation catalyzed by [γ-(SiO4)W10O32H4] 4-. A computational study. Inorganic Chemistry, 45(14), 5703–5709. https://doi.org/10.1021/IC060725P

[162] Keller, N., Ivanez, J., Highfield, J., & Ruppert, A. M. (2021). Photo-/thermal synergies in heterogeneous catalysis: Towards low-temperature (solar-driven) processing for sustainable energy and chemicals. Applied Catalysis B: Environmental, 296, 120320. https://doi.org/10.1016/J.APCATB.2021.120320

[163] Liu, B., Bie, C., Zhang, Y., Wang, L., Li, Y., & Yu, J. (2021). Hierarchically porous zno/g-c3n4s-scheme heterojunction photocatalyst for efficient h2o2production. Langmuir, 37(48), 14114–14124.

[164] Liu, T., Pan, Z., Vequizo, J. J. M., Kato, K., Wu, B., Yamakata, A., Katayama, K., Chen, B., Chu, C., & Domen, K. (2022). Overall photosynthesis of H2O2 by an inorganic semiconductor. *Nature Communications 2022 13:1*, *13*(1), 1–8. https://doi.org/10.1038/s41467-022-28686-x

[165] Luo, Y., Zhang, B., Liu, C., Xia, D., Ou, X., Cai, Y., Zhou, Y., Jiang, J., & Han, B. (2023). Sulfone-Modified Covalent Organic Frameworks Enabling Efficient Photocatalytic Hydrogen Peroxide Generation via One-Step Two-Electron O2 Reduction. Angewandte Chemie - International Edition. https://doi.org/10.1002/ANIE.202305355

[166] Gu, M., Yang, Y., Zhang, L., Zhu, B., Liang, G., & Yu, J. (2023). Efficient sacrificial-agent-free solar H2O2 production over all-inorganic S-scheme composites. Applied Catalysis B: Environmental, 324, 122227. https://doi.org/10.1016/J.APCATB.2022.122227

[167] Jourshabani, M., Yun, S. –H, Razi Asrami, M., & Lee, B. –K. (2022). Superior photodegradation of organic compounds and H2O2 production over tungsten oxide/carbon nitride heterojunction with sizable heptazine units: Dual polycondensation and interface engineering. *Chemical Engineering Journal*, *427*, 131710. https://doi.org/10.1016/J.CEJ.2021.131710

[168] Li, L., Huo, X., Chen, S., Luo, Q., Wang, W., Wang, Y., & Wang, N. (2023). Solar-Driven Production Of Hydrogen Peroxide And Benzaldehyde In Two-Phase System By An Interface-Engineered Co9S8-CoZnIn2S4 Heterostructure. *Small*, 2301865. https://doi.org/10.1002/SMLL.202301865

[169] Zhang, J., Zheng, L., Wang, F., Chen, C., Wu, H., Leghari, S. A. K., & Long, M. (2020). The critical role of furfural alcohol in photocatalytic H2O2 production on TiO2. *Applied Catalysis B: Environmental*, *269*, 118770. https://doi.org/10.1016/J.APCATB.2020.118770

[170] Wang, L., Li, B., Dionysiou, D. D., Chen, B., Yang, J., & Li, J. (2022). Overlooked Formation of H2O2 during the Hydroxyl Radical-Scavenging Process When Using Alcohols as Scavengers. *Environmental Science and Technology*, *56*(6), 3386–3396.

[171] Kieu, L., Boyd, P., & Idriss, H. (2002). Trends within the adsorption energy of alcohols over rutile TiO2(1 1 0) and (0 1 1) clusters. *Journal of Molecular Catalysis A: Chemical*, *188*(1–2), 153–161. https://doi.org/10.1016/S1381-1169(02)00210-8

[172] Nguyen, T. T. D., Nguyen, D., Vo, P. P., Doan, H. N., Pham, H. T. N., Hoang, V. H., Tien Le, K., Kinashi, K., Huynh, V. T., & Nguyen, P. T. (2023). The roles of ethanol and isopropanol as hole scavengers in the photoreduction reaction of graphene oxide by TiO2: A competition of oxygenated groups removal and carbon defects invasion. *Journal of Molecular Liquids*, *381*, 121831. https://doi.org/10.1016/J.MOLLIQ.2023.121831

[173] Zhang, K., Dan, M., Yang, J., Wu, F., Wang, L., Tang, H., & Liu, Z. Q. (2023). Surface Energy Mediated Sulfur Vacancy of ZnIn2S4 Atomic Layers for Photocatalytic H2O2 Production. Advanced Functional Materials, 2302964. https://doi.org/10.1002/ADFM.202302964

[174] Shao, G., & Shao, G. (2021). Work Function and Electron Affinity of Semiconductors: Doping Effect and Complication due to Fermi Level Pinning. Energy & Environmental Materials, 4(3), 273–276. https://doi.org/10.1002/EEM2.12218

[175] Singh, S., Punia, R., Pant, K. K., & Biswas, P. (2022). Effect of work-function and morphology of heterostructure components on CO2 reduction photo-catalytic activity of MoS2-Cu2O heterostructure. Chemical Engineering Journal, 433, 132709. https://doi.org/10.1016/J.CEJ.2021.132709

[176] Fonagy, O., Szabo-Bardos, E., & Horvath, O. (2021). 1, 4-Benzoquinone and 1, 4-hydroquinone based determination of electron and superoxide radical formed in heterogeneous photocatalytic systems. *Journal of Photochemistry and Photobiology A: Chemistry*, *407*, 113057. https://doi.org/10.1016/j.jphotochem.2020.113057